Effect of Forming Temperature and Sheet Temper on the Brazing Characteristics of Aluminum Alloy Sheet

by

Michael J. Benoit

A thesis

presented to the University of Waterloo

in fulfillment of the

thesis requirement for the degree of

Doctor of Philosophy

in

Mechanical and Mechatronics Engineering

Waterloo, Ontario, Canada, 2018

Examining Committee Membership

The following served on the Examining Committee for this thesis. The decision of the Examining Committee is by majority vote.

External Examiner   DAVID WILKINSON

            Distinguished University Professor, McMaster University

Supervisor   MARY WELLS

            Professor, University of Waterloo

Supervisor   CAROLYN HANSSON

            Professor, University of Waterloo

Internal Member   NORMAN ZHOU

            Professor, University of Waterloo

Internal Member   MICHAEL WORSWICK

            Professor, University of Waterloo

Internal-external Member   ALEXANDER PENLIDIS

            Professor, University of Waterloo

Author's Declaration

This thesis consists of material all of which I authored or co-authored: see Statement of Contributions included in the thesis.

This is a true copy of the thesis, including any required final revisions, as accepted by my examiners.

I understand that my thesis may be made electronically available to the public.

Statement of Contributions

The research contained within this thesis was conducted as part of a Natural Sciences and Engineering Research Council of Canada Collaborative Research and Development grant (NSERC CRD), in collaboration with Dana Canada Corporation and CanmetMATERIALS. Furthermore, the results presented in Chapters 3 to 6 have been adapted from manuscripts which are published, or are to be published. As a result, a number of co-authors have contributed to the current work. However, all measurements which were not performed by me were conducted either under my direct supervision, or were co-ordinated by me. All analysis and synthesis of the results was performed by me. The individual contributions from all co-authors are as follows:

Prof. Mary Wells and Prof. Carolyn Hansson: supervised all work completed in this thesis, and provided both technical and editorial feedback in the preparation of the work.

Prof. Michael Worswick: supervised the development of the finite element models, and provided feedback in the preparation of the manuscripts which are the basis of Chapters 5 and 6.

Dr. Sooky Winkler: provided technical and editorial feedback in the preparation of manuscripts.

Dr. Haiou Jin: performed tensile tests reported in Chapters 3, 4, and 7, and collected energy dispersive x-ray spectroscopy (EDS) data in Chapter 4.

Dr. Babak Shalchi Amirkhiz: performed transmission electron microscopy (TEM) measurements reported in Chapter 4.

Mr. Mark Whitney: calibrated the differential scanning calorimeter (DSC) for experiments reported in Chapter 3.

Mr. Kyu Bin Han: developed the finite element models of the battery cooling plates described in Chapters 5 and 6, and assisted in forming battery cooling plate samples.

Ms. Ramneek Kaur: performed sagging distance measurements reported in Chapter 4.

Abstract

Automotive heat exchangers are fabricated by forming and brazing of multi-layered aluminum (Al) alloy sheets. The Al brazing sheets are comprised of two alloy layers: an AA3xxx core, which provides strength to the assembly, and an AA4xxx clad, which melts during brazing to provide filler metal for joints throughout the assembly. Warm forming has recently proven to be a promising technique to expand heat exchanger design possibilities, by increasing the material forming limits, and by enabling the use of higher strength materials, by reducing springback after forming. However, no consideration had been given to the effect of warm forming on downstream brazing and corrosion performance. The objective of the current research is to understand the effect of forming temperature and initial sheet condition on the brazing performance of Al brazing sheets.

The Al brazing sheet used throughout the current work was industrially produced, with an overall thickness of 200 µm, and a single AA4045 clad layer comprising 10 % of the sheet thickness. The sheets were supplied in both the fully annealed (O) and the work hardened (H24) sheet tempers. Warm forming was initially simulated by performing interrupted tensile tests between room temperature (RT) and 250 °C, up to pre-determined levels of strain between 2 % and 12 %, at an average engineering strain rate of $6.6 \times 10^{-4}\,\mathrm{s}^{-1}$.

The rate of liquid clad alloy depletion during simulated brazing was measured with differential scanning calorimetry, using a parameter referred to as the liquid duration time (LDT). A small LDT, caused by rapid depletion of the liquid clad due to penetration into the core alloy, was predicted to result in poor brazing performance. The LDT for the O-RT forming condition decreased from 44.2 min when no strain was applied to the sheet, to a minimum value of 29.7 min at 4 % strain, before increasing with the further application of strain. The LDT data were correlated with the post-braze sheet microstructures: when the LDT was decreasing, the core alloy was non-recrystallized and the phenomenon of liquid film migration (LFM) occurred during brazing, while for conditions where the LDT was increasing, the core alloy was characterized by coarse, recrystallized grains without LFM. The trend in the LDT data was in excellent agreement with prior studies where LFM had been observed, indicating the suitability of the LDT as a predictor of brazing performance. When the forming temperature was increased to 250 °C, the LDT decreased from 42 min at 0 % strain, to a minimum value of 26 min at 8 % strain, but did not increase at greater applied strains. The change in the LDT data after warm

forming was attributed to an increased range of strains over which LFM occurred. Thus, brazing of O temper sheet formed at 250 °C was predicted to be impaired relative to RT formed sheet. Conversely, the LDT for H24 sheet was found to be independent of both applied strain and forming temperature, and a recrystallized core alloy was observed in all cases. While some dynamic recovery is believed to have occurred during warm forming, the H24 core alloy hardness was still in the same order of magnitude as RT formed sheet, so core alloy recrystallization could still occur. Consequently, brazing of H24 temper sheet was predicted to be insensitive to forming temperature.

The difference in brazing characteristics of O-RT and O-250 °C conditions was confirmed from sagging distance experiments, again using warm formed tensile coupons. Maximum sagging of O-RT sheet occurred at 4 % strain, while complete rigidity was observed at higher strains. For O-250 °C samples, the sagging distance remained elevated between 2 % to 12 % strain. Similar to conditions with a low LDT, LFM was observed in the post-braze micrographs of forming conditions with large sagging distances (i.e. O-RT-4 % and O-250 °C-10 %), and transmission electron microscopy revealed a recovered sub-structure in front of the LFM grains. The sagging distance as a function of strain for O-150 °C samples was close to that of the RT formed sheet, which indicated that formability improvements could be achieved at this temperature, without altering the brazing characteristics of the sheet.

The brazing predictions made using the LDT and sagging distance data were tested by brazing of scaled-down electric vehicle battery cooling plates, which were formed from both O and H24 sheet tempers, between RT and 250 °C. Simulated brazing of single formed plates revealed that the microstructures within the plate were in good agreement with the results from the simplified tensile test specimens, at comparable levels of strain. Formed plates of the same forming conditions were then brazed together, to create functional cooling plates. In all cases, plates were successfully brazed, and were capable of withstanding an applied internal pressure of 0.28 MPa. Furthermore, no obvious difference in the brazing performance was found between the various sheet temper-forming temperature combinations at the component-level, and warm forming was shown to not adversely impact the ability to form brazed joints. The LDT and sagging distance measurements taken from strained sheet specimens were shown to be inadequate to predict the brazing performance of warm formed O temper sheet in assemblies more representative of heat exchangers, since these metrics did not account for wetting and

capillary flow of the liquid clad alloy. Microstructure analysis confirmed that the microstructures were similar to the warm formed tensile specimens, although certain microstructures not present in the tensile specimens were also observed, such as strain induced boundary migration in the O-250 °C condition. However, the strain rate in the plates was estimated to be in the order of $1.0 \times 10^{-1} \, s^{-1}$, orders of magnitude higher than the tensile specimens, and the plates experienced a significantly higher local strain (25 %) at the location in question. Additional tensile tests performed up to 20 % strain at 150 °C and 250 °C, using strain rates between $6.6 \times 10^{-4} \, s^{-1}$ and $6.6 \times 10^{-2} \, s^{-1}$, revealed a dependence of the post-braze microstructure on the strain rate, due to increased strain rate sensitivity at elevated temperatures, and similar microstructures as observed in the plates were found for comparable strains and strain rates.

It is concluded that warm forming, used to improve formability of Al brazing sheet, does not impair brazing performance. Brazing predictors, such as the LDT and sagging distance, are useful for studying interactions occurring within the sheet during brazing, but do not account for liquid clad flow, which is a major factor in brazed joint formation in real components. The microstructure evolution of O temper sheet during brazing depends on applied strain, strain rate, and forming temperature. The change in microstructure with changes in process variables also supports the deformation energy driving force for the LFM phenomenon. The H24 sheet was found to be insensitive to an increase in forming temperature, in terms of the post-braze microstructure, LDT, and ability to braze real components. It is recommended that the potential of the warm forming process be further investigated by forming full-scale components, and forming at higher temperatures to further improve forming limits and springback reduction. Finally, the relative corrosion performance of the different sheet tempers and forming temperatures must be more thoroughly investigated.

Acknowledgements

Similar to the raising of a child, it has taken a village to complete my doctorate degree, despite a single name appearing on this thesis. For this reason, I would like to take this opportunity to thank the key people those who have contributed in one way or another to the completion of this thesis and my degree.

To my supervisors, Mary Wells and Carolyn Hansson, I am forever grateful for your continual encouragement to pursue my ideas and interests, and for giving me the freedom to grow as a researcher. I am also thankful for the countless reference letters written and the opportunities you have created for me along the way. Similarly, I would like to thank Michael Worswick for making the time to meet with me to discuss the warm forming project, and for your mentorship throughout the completion of my degree.

To my remaining committee members, Norman Zhou, Michael Fowler, Alexander Penlidis, and David Wilkinson, thank you for your guidance in completing this work. Your feedback and contributions have helped improve the overall quality of the research contained in this thesis. To all the staff at Dana Canada, including Zeljko Gabriscek, Chris Shore, Mona Emrich, Farzad Younesi, Leo Colley, Feng Liang, and Sooky Winkler, I appreciate the countless hours spent with me to develop brazing procedures and assessment techniques. To Haiou Jin, I am grateful for your willingness to always assist me in obtaining experimental results, and I will continue to be amazed at your rapid turnaround on delivering these results. To Mark Kozdras, your willingness to offer your past experiences and insights to help guide my research efforts is greatly appreciated. The generous financial support from the Natural Sciences and Engineering Research Council of Canada (NSERC), the Canada Foundation for Innovation (CFI), the Ontario Research Fund (ORF), and Automotive Partnership Canada (APC) which made this research possible is also gratefully acknowledged.

To all of my office- and lab- mates, including Mark Whitney, Massimo DiCiano, Rick Wong, Yu Wang, Kyu Bin Han, Colin Van Niejenhuis, Ibrahim Ogunsanya, Adam Felinczak, Peter Loudfoot, Marc Johnson, and Leak Kristufek, with whom I have shared countless lunches, coffees, birthday celebrations, and who have been on the receiving end of many unsolicited venting sessions, thank you for our shared time together and for all you have done for me. To my closest friends Kyle McConnell, John Rafferty, Zack Medeiros, Jason Oncz, Jeff Barrett,

Rob Reid, Micheal Walsh, Boyd Panton, and many others, thank you for all the memories, and for always being there for me.

Finally, I will forever cherish the unwavering support from my family. To my mom and dad, who have never doubted my abilities and who I know would do anything to help me, I cannot express how thankful I am to have both of you to look to for support in all things. To Nicole Holland, I am truly blessed to call you my partner in life. Through the best and worst of times, I know I will always have you by my side. To my dear brother Matthew, while we often don't see things the same way, I know I can always turn to you in times of need. To my furrier, four legged brother Molson, you have never left my side and you are this man's best friend. To my grandpa, I am forever grateful for everything you have done for me – sometimes the little things are the big things in life. To my late grandma, who was "totally proud of her grandkids", your love will never be forgotten and you are greatly missed.

Table of Contents

List of Figures

List of Tables

List of Abbreviations

BF-STEM – Bright Field Scanning Transmission Electron Microscopy

BDP – Band of Dense Precipitates

CAB – Controlled Atmosphere Brazing

CRD – Collaborative Research and Development (grant)

DSC – Differential Scanning Calorimetry

EDS – Energy Dispersive x-ray Spectroscopy

FE – Finite Element (model)

FIB – Focussed Ion Beam

ICP-OES – Inductively Coupled Plasma-Optical Emission Spectrometry

LDT – Liquid Duration Time

LFM – Liquid Film Migration

NSERC – Natural Sciences and Research Council of Canada

RT – Room Temperature

SD – Sagging Distance

SEM – Scanning Electron Microscopy

SIBM – Strain Induced Boundary Migration

SILFM – Strain Induced Liquid Film Migration

SWAAT – Sea Water Acetic Acid Test

TEM – Transmission Electron Microscopy

"They reason theoretically, without demonstrating experimentally, and errors are the result."

-Michael Faraday

1.   Introduction

1.1.   Background

Aluminum (Al) alloys have been used extensively in automotive heat exchangers since the 1970s, when they replaced copper and brass systems due to their low density, high strength, good corrosion resistance, and good heat transfer properties [1, 2, 3]. The heat exchangers are fabricated by forming multi-layered Al alloy sheets into the required shape, assembling and fixing the formed components into the required configuration, and passing the assembly through a controlled atmosphere furnace where the components are brazed. Upon removal from the furnace, the heat exchanger should be fully joined with leak-free coolant channels. Throughout the remainder of this thesis, these multi-layered Al alloy sheets are referred to as "Al brazing sheet", and details of the composition and relevant metallurgy for these sheets will be described in detail in section 2.1.

With the introduction of electric vehicles to the automotive marketplace, innovative heat exchanger technologies have been developed to efficiently cool the batteries and associated electronics. For example, Al alloy cooling plates (Fig. 1-1) are sandwiched between battery cells in the electric Ford Focus, and a coolant is circulated through a serpentine channel in the plate in order to regulate the battery temperature [4]. Half of the channel cross-section is stamped into an Al brazing sheet blank, and two stamped sheets are subsequently fixed together and brazed to create leak-free channels.

Fig. 1-1 Stamped and brazed battery cooling plate used in the electric Ford Focus. Image courtesy of Dana Canada.

As manufacturers seek to improve performance while simultaneously reducing cost and weight, the trend has been to use thinner Al brazing sheets with higher strength and enhanced corrosion resistance in heat exchanger production. However, deformation of these thinner sheets is a concern, and stricter control of the brazing process is required [1]. Two important issues were recently identified during forming of Al brazing sheet. First, as noted by Miller *et al.* [2], there is limited space available within the vehicle for heat exchanger components; the materials used in heat exchanger applications must have good formability to enable designs that optimize performance in a restricted space. Unfortunately, the room temperature formability of Al brazing sheet is relatively low compared to other conventional materials, such as sheet steel [5], which can limit possible component designs and, consequently, heat transfer performance. Second, due to their low elastic modulus, Al alloys experience significant springback after forming, resulting in poor component flatness. Springback is particularly concerning for higher initial strength Al brazing sheet, such as those in work hardened conditions, since springback increases with a material's yield strength [6]. Poor component flatness makes the formation of high quality brazed joints, which are necessary for a leak-free assembly, difficult to achieve.

Recent research conducted at the University of Waterloo has shown that by increasing the forming temperature, up to 325 °C, the forming limits of Al brazing sheet can be increased [7, 8], and the level of springback after forming can be reduced [9, 10, 11]. However, while warm forming appears to be a promising technique for Al heat exchanger production, the effect that warm forming could have on downstream brazing and corrosion performance has not previously been studied. This is a critical gap in materials processing knowledge. When the heat exchanger assembly is in the brazing furnace, the multi-layered structure of Al brazing sheets is designed to allow one of the layers to melt to provide braze joint filler metal, while the other layer remains solid. However, interactions occur between the liquid and solid alloys during brazing, which can affect brazing performance, and the extent of these interactions depends on the starting microstructure and the amount of deformation imparted to the sheet during forming [12]. Furthermore, it is known that the corrosion performance of heat exchangers depends on the microstructure and phases present within the sheet after brazing, and, thus, on the extent of interaction during brazing [1, 13]. Thus, a detailed study on the effect of warm forming of Al brazing sheet on brazing and corrosion performance must be investigated before the process can be considered a viable manufacturing route for automotive heat exchanger production.

2

1.2. Objectives

The research detailed in this thesis was conducted as part of a Natural Sciences and Engineering Research Council of Canada (NSERC) Collaborative Research and Development (CRD) grant with Dana Canada Corporation, a global leader in automotive heat exchanger production. Prior research regarding warm forming of Al brazing sheet had shown the potential of the process to increase material forming limits, which would allow for an increase in potential product designs and a reduction in the number of forming steps required to achieve a given geometry. The current CRD expands on the results of the prior research, with the overall goal of demonstrating the commercial viability of warm forming Al brazing sheet in automotive heat exchanger production. The research conducted as part of the CRD was divided into four tasks: (i) identification of a lubricant suitable for warm forming, without any adverse effects on brazing; (ii) optimization of the warm forming process for low cycle time, increased sheet formability, and springback reduction; (iii) development of warm forming process models, and (iv) characterization of brazing and corrosion performance of warm formed components.

The objective of the research detailed in this thesis was to address task (iv) by investigating the question *"How do forming temperature and starting sheet temper impact the brazing performance of Al brazing sheet used in automotive heat exchanger production?"* Aspects of the research contribute to fundamental knowledge regarding the metallurgical interactions that occur between the Al brazing sheet alloys during brazing, and the role that microstructure and stored energy have on these phenomena. Other facets of the research address the engineering aspects and commercial viability of the warm forming process, in terms of the ability to successfully braze warm formed components, and their corrosion resistance relative to components formed at room temperature. The research contributions are expanded upon in the following section, within the context of the thesis structure.

1.3. Thesis Structure

The remaining contents of this thesis are organized as a manuscript-based thesis. Chapter 2 provides a review of the topics and literature relevant to the current research. Chapters 3 to 6 are modified versions of published articles or manuscripts in preparation, which report the research findings. The candidate is the primary author of all manuscripts, and was responsible for directly collecting data or co-ordinating the collection of data, and for conducting the

synthesis and analysis of the results. A full description of the contributions from all co-authors was provided in the Statement of Contributions. Modifications have been made to the original manuscripts to create a cohesive research arc across related studies. Introduction and conclusion sections of the original manuscripts have been re-framed to make connections between the findings of the four manuscripts. Experimental and discussion sections have been modified to reduce repetition of information across thesis chapters. Copies of the necessary copyright permissions are provided prior to the references. As noted in the preceding section, the research contained within this thesis makes original and important contributions to both fundamental knowledge and engineering applications in materials processing. The breakdown in contributions and the corresponding thesis chapters is shown in Fig. 1-2.
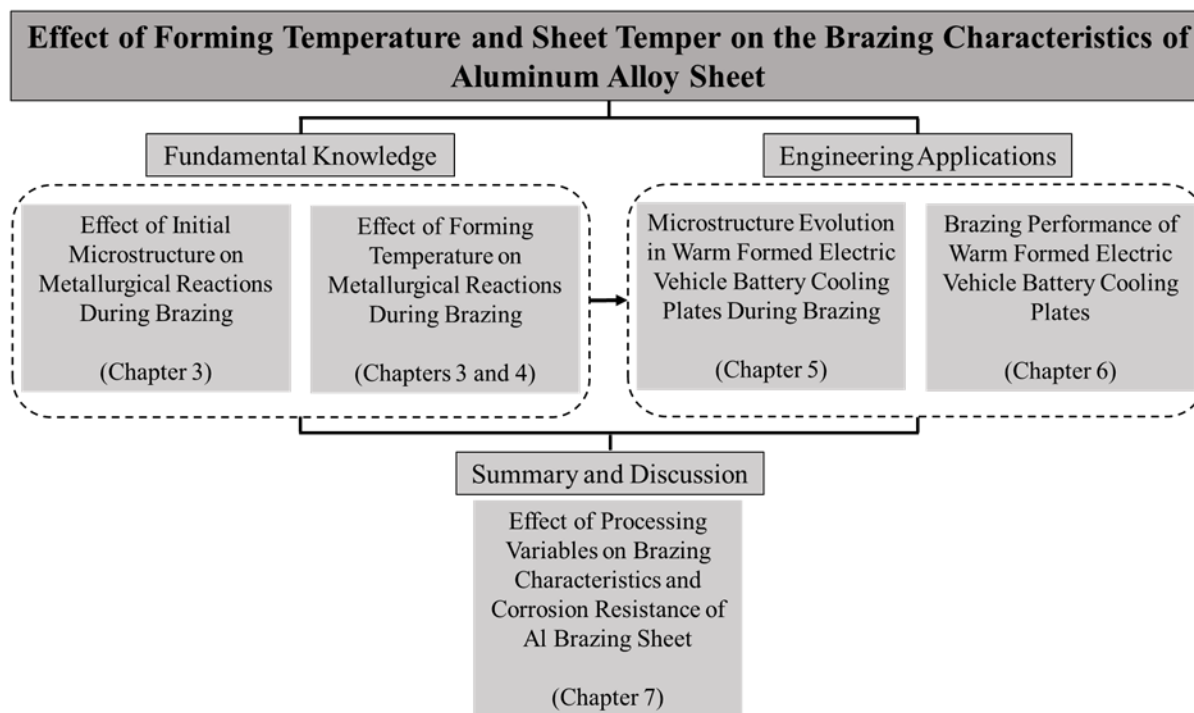
Fig. 1-2 Contributions of the conducted research to fundamental knowledge and engineering applications, and the corresponding thesis chapters.

Chapter 3 details the first ever investigation into the effect of warm forming on brazing performance. Warm forming was simplified by performing interrupted tensile tests on Al brazing sheet samples at room temperature and 250 °C. Furthermore, Al brazing sheet of both O and H24 tempers were used to investigate the effect of the initial sheet condition on the relationship

4

between forming temperature and brazeability. Thermal analysis was used to predict brazing performance as a function of applied strain, by measuring the solid-liquid interaction kinetics within the sheet during brazing. A distinct difference in the relationship between applied strain and brazing performance was found for O temper sheet when the forming temperature was increased, from which it was predicted that brazing performance would be impaired after warm forming. Conversely, no change in brazing performance of H24 temper sheet was predicted after an increase in forming temperature. The research findings were originally published as: M. J. Benoit, M. A. Whitney, M. A. Wells, H. Jin and S. Winkler, "Liquid film migration in warm formed aluminum brazing sheet," *Metallurgical and Materials Transactions A*, vol. 48, no. 10, pp. 4645-4654, 2017.

Based on the results of Chapter 3, the relationship between brazing performance and forming temperature for O temper sheet was further investigated in Chapter 4. It was of interest to determine if there was a forming temperature which would improve sheet formability without impairing brazing performance. Warm forming was again simulated by tensile tests performed at room temperature, 150 °C, 200 °C, and 250 °C, while brazing performance was predicted by the commonly used sagging test. The results revealed that Al brazing sheet formed at 150 °C would yield similar brazing performance to room temperature strained sheet. The findings were originally published as: M. J. Benoit, R. Kaur, M. A. Wells, H. Jin, B. Shalchi Amirkhiz and S. Winkler, "Sagging resistance of warm formed aluminum brazing sheet," *Journal of Materials Processing Technology*, vol. 254, no. 4, pp. 353-360, 2018.

Chapters 3 and 4 provided new insights into the effect of forming temperature and initial sheet condition on brazing performance. However, the results were from simple uniaxial tensile specimens, which may not be representative of actual process parameters used in heat exchanger production. Chapter 5 presents the results of an investigation into the microstructure evolution during brazing in a scaled-down electric vehicle battery cooling plate design. Based on the prior results, plates were formed from both O and H24 temper sheets at room temperature, 150 °C, and 250 °C. A finite element model of the formed plate was used to predict strains throughout the plate, to facilitate comparisons of the microstructure in the plate with those from the uniaxial tensile specimens. The findings were originally published as: M. J. Benoit, K. B. Han, M. J. Worswick, M. A. Wells and S. Winkler, "Brazing characteristics of warm formed automotive

heat exchanger components," in *16th International Conference on Aluminum Alloys (ICAA 16)*, Montreal, 2018, ISBN 978-1-926872-41-4.

All of the results prior to Chapter 6 predicted brazing performance based on post-braze microstructure and other indirect measurements. Chapter 6 details an investigation into the feasibility of creating leak-free battery cooling plates from warm formed components, where brazing was assessed at the microstructure and component levels. Microstructures were compared with those of the prior chapters, while the consistency of brazed joint formation and the ability to be pressurized without leaking were used to assess brazing at the component level. The results of this chapter have been prepared as a manuscript to be submitted.

Chapter 7 presents a summary of the prior chapters, and makes connections between the effects of initial sheet temper, forming temperature, strain, and strain rate on the brazing performance and resultant post-braze microstructures. Preliminary results from an accelerated corrosion test using brazed battery cooling plates are also presented. Major conclusions from the work and a set of recommended actions are presented in Chapter 8.

2.   Literature Review

This chapter provides an overview of the topics and prior research relevant to the work contained in this thesis. The chapter begins with a description of the metallurgy and production of the materials used in automotive heat exchanger production. An outline of the prior research into how warm forming can be used to expand heat exchanger design and enable the use of higher strength sheets is then given. A brief description of the general principles of the brazing process and brazed joint formation in Al heat exchangers is presented. The microstructure evolution within the brazing sheet during processing is then discussed, with connections drawn between sheet deformation and the brazing temperature cycle. The implications of the microstructural evolution during brazing on the susceptibility of the sheet to corrosive attack are presented, with a brief discussion of a phenomenon which takes advantage of diffusion to prevent rapid corrosive failure. The chapter concludes with a brief review of the relationships between forming, brazing, and corrosion performance, where the gaps in current Al brazing sheet processing knowledge are, and how the work in this thesis addresses these gaps.

2.1.   Al Brazing Sheet

Automotive heat exchangers are often produced by forming and brazing of multi-layered Al alloy sheets (i.e. Al brazing sheet). Al brazing sheets are comprised of at least two Al layers, namely the core alloy and clad alloy. Additional layers may be used in certain applications, such as a sacrificial zinc (Zn)-rich Al alloy for components requiring enhanced corrosion resistance [1]. However, as the research in this thesis uses Al brazing sheets with only two layers, this section focusses on the alloys used in these two layers, and the production of the laminate brazing sheet.

2.1.1. Core Alloys

The core alloy is the thicker of the two alloy layers, and provides the strength and lifecycle requirements for the heat exchanger product [2]. Typically, the core is either an AA3xxx or AA6xxx series alloy [1, 14, 15]. Commonly used core alloy compositions and corresponding melting ranges are presented in Table 2-1. From the table, AA6xxx alloys have a solidus temperature 15 °C to 30 °C lower than the AA3xxx series alloys, and have been reported to have detrimental interactions with the liquid clad alloy during brazing [15, 16]. As a result,

7

stricter control of the brazing process is necessary with AA6xxx cores. Since an AA3xxx core alloy was used in the Al brazing sheet used throughout the current work, AA6xxx alloys will not be discussed further.

Table 2-1 Nominal compositions and melting ranges of commonly used core alloys. Table reproduced with permission [1].

Alloy	Nominal alloying element concentration (wt%) – bal. Al				Melting temperature (°C)	
	Si	Cu	Mn	Mg	Solidus	Liquidus
AA1100	-	0.12	-	-	643	657
AA1145	0.30	-	-	-	646	657
AA3003	-	0.12	1.2	-	643	655
AA3005	0.60	0.30	1.2	0.40	629	654
AA6063	0.40	-	-	0.70	615	655
AA6951	0.30	0.30	-	0.40	616	654

The AA3xxx alloys have a relatively high manganese (Mn) content, to provide strength to the alloy. Manganese is present in the core alloy in both a (super saturated) solid solution with the Al matrix and within a number of second phase particles including $Al_6(Mn, Fe)$, α-$Al_{15}(Mn, Fe)_3Si_2$, and α-AlMnSi [3, 17, 18, 19]. The difference in Mn content in the matrix compared to second phase particles has an important role in corrosion resistance of the core alloy, and will be discussed in section 2.5. Magnesium (Mg) can be added to the core to increase strength, but too high a Mg content impairs brazing performance of the sheet due to reactions with the flux during brazing [1]. The silicon (Si) content in the core must be kept to a low level, to allow for the development of a sacrificial layer during brazing. Copper (Cu) can be added to the core to provide solid solution strengthening and improve the corrosion resistance of the core. For Cu-containing core alloys, the presence of small Al_2Cu particles has also been reported [20, 21]. Iron (Fe) is often present in the core alloys, usually as intermetallic particles with Al and Mn. However, Fe has a detrimental effect on the corrosion resistance of the core, so it is typically maintained at a low level. The nature of second phase particles in the core and distribution of alloying elements changes during brazing, and will be discussed in subsequent sections.

2.1.2. Clad Alloys

The second layer in the brazing sheet is the clad alloy, which may be present on either one or both sides of the sheet, and typically has a thickness of approximately 10 % of the total sheet thickness. The clad is always one of the Si-rich AA4xxx series alloys; commonly used clad alloy compositions and melting temperature ranges are presented in Table 2-2. Referring to Tables 2-1 and 2-2, the Si-rich clad alloys have a liquidus temperature significantly below the AA3xxx core alloys solidus temperature. Thus, when the heat exchanger assembly is placed in the furnace for brazing, the clad alloy partially or completely melts, depending on the composition and brazing temperature profile, to provide the brazed joint filler metal, and co-exists with the solid core alloy. Additional reasons for using AA4xxx alloys for the clad include: (i) good wettability and low interfacial energy with the core alloy, (ii) a similar corrosion potential to the core alloy, reducing the driving force for galvanic corrosion, and (iii) a relatively small melting temperature range, allowing good control of the liquid filler metal [1]. The pre-braze clad alloy microstructure is characterized by numerous Si particles, surrounded by an Al solid solution matrix with low Si content.

Table 2-2 Nominal compositions and melting ranges of commonly used clad alloys. AWS Brazing Handbook 4th Edition:1991, Table 3.4, reproduced with permission from the American Welding Society (AWS), Miami, FL [22].

Alloy	Nominal alloying element concentration (wt%) – bal. Al					Melting temperature (°C)	
	Si	Cu	Mn	Mg	Zn	Solidus	Liquidus
AA4343	6.80-8.20	0.25	0.10	-	0.20	577	617
AA4145	9.30-10.70	3.30-4.70	0.15	0.15	0.20	521	585
AA4047	11.00-13.00	0.30	-	0.10	0.20	577	582
AA4045	9.00-11.00	0.30	0.05	0.05	0.20	577	599

2.1.3. Production

Al brazing sheets have traditionally been produced by roll bonding of direct chill (DC) cast ingots of the clad and core alloys [1, 14, 19]. The core alloy ingot may or may not be homogenized after casting, depending on the application, and the surface of the ingot is scalped. Homogenization is performed for sheets that require good formability, while sheets requiring good corrosion performance are not homogenized [19]. Prior to being placed on the surface of

the core ingot, the clad alloy ingot thickness is reduced by rolling. The multi-alloy assembly is pre-heated and hot rolled, to create a metallurgical bond at the interface. Additional hot rolling passes are performed to reduce the ingot thickness. A number of cold rolling passes are then conducted to achieve the final sheet thickness, with inter- and end-annealing steps used as necessary to achieve the desired final properties in the sheet. An example of Al brazing sheet cross section in the pre-braze condition is given in Fig. 2-1. The core alloy second phase particles and the Si particles in the clad are clearly observed in the figure. The use of Al brazing sheets allows for numerous brazed joints to be formed simultaneously, even in complex assemblies, without needing to place filler metal foil at joint locations, since the filler alloy is roll bonded to the base metal surface [22, 23].
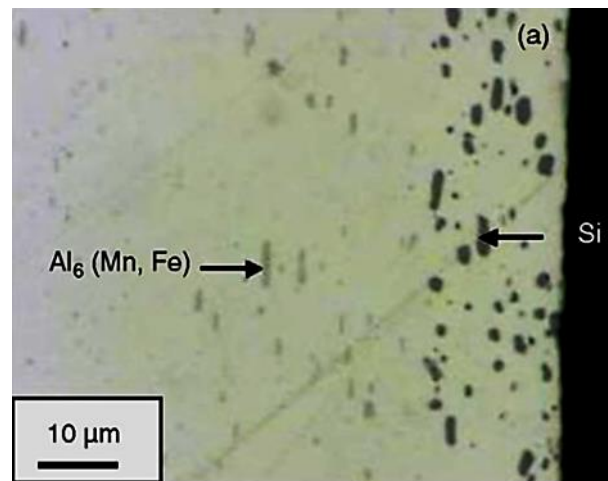
Fig. 2-1 Al brazing sheet cross-section in the as-received (pre-braze) condition. Reprinted from Materials Science and Engineering: A, vol. 413, Lacaze *et al.*, Study of the microstructure resulting from brazed aluminium materials used in heat exchangers, pp. 317-321 © 2005, with permission from Elsevier [24].

2.2. Warm Forming

When the Al brazing sheet is formed into the required component geometry, dislocations are introduced to the material, which increase the stored deformation energy [24]. The dislocation density (ρ) can be approximately related to the material flow stress (σ) according to Eq. 1 [25]:

$$\sigma = cGb\sqrt{\rho} \qquad \qquad \text{Eq. 1}$$

where G is the shear modulus, b is the Burgers vector, and c is a material constant. According to Bergstrom [26], the net rate of dislocation accumulation as a function of strain is equal to the rate of dislocation generation less the rate of dislocation rearrangement or annihilation. The dislocation density increases with strain and dislocations become entangled during room temperature forming, since dislocations are not rapidly annihilated at room temperature, leading to work hardening of the material. However, the rate of dislocation remobilization and annihilation during forming was shown to depend on the strain rate and forming temperature [27]. The Bergstrom hardening model was shown to adequately describe plastic deformation of Al brazing sheet at different forming temperatures and strain rates [28].

Deformation at temperatures above room temperature, but below the material recrystallization temperature, is known as warm forming [6, 29]. Warm forming can significantly improve the material ductility, without recrystallizing the material as in hot forming [30]. Shehata *et al*. [31] were among the first to demonstrate the benefits of warm forming, using Al-Mg alloys. A six-fold increase over the room temperature total elongation was obtained when the tensile tests were performed at 280 °C, due to an extended diffuse necking regime after uniform elongation. The material flow stress was shown to be governed by strain rate hardening rather than by strain hardening as the forming temperature increased, as evidenced by an increase in the strain rate sensitivity exponent (m) from 0.08 at 150 °C to 0.34 at 260 °C for one of the alloys studied. Since the work of Shehata *et al.*, most studies on warm forming of Al alloys have focussed on AA5xxx and AA6xxx series alloys [32, 33], although other studies on AA1xxx, AA2xxx, AA3xxx, and AA7xxx alloys have also been conducted [5, 34, 35].

As noted in Chapter 1, heat exchanger design possibilities are limited by the forming limits of Al brazing sheet, and the use of thin brazing sheets with high initial strength is limited due to high levels of springback. Recent studies have shown that warm forming is a promising method to alleviate both of these formability concerns for Al brazing sheet. For example, Bagheriasl *et al.* showed that the total elongation of Al brazing sheet rapidly increased when the forming temperature exceeded 100 °C, reaching 60 % elongation at 250 °C, and that the material showed greater sensitivity to strain rate (Fig. 2-2) [7]. These results were in agreement with Abedrabbo *et al.*, who showed that when the forming temperature of H24 temper AA3003 sheet increased from room temperature to 260 °C, n decreased from 0.215 to 0.116, while m increased from 0.003 to 0.080 [34]. The practical implications of increased forming limits were

demonstrated by Bagheriasl *et al.*, who showed that a heat exchanger component with a drawn cup feature (Fig. 2-3), which could not be formed at room temperature, could be formed in a single step with a die heated to 300 °C and a cold punch. The formability improvements associated with warm forming of Al brazing sheet were further demonstrated in a follow-up study, where forming limit curves for the Al brazing sheet shifted to greater strains with increasing forming temperature [8].
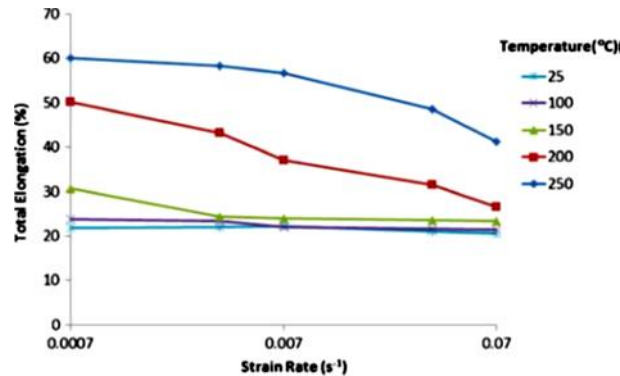
Fig. 2-2 Total elongation of Al brazing sheet as a function of strain rate and forming temperature. Reprinted with permission from Springer Nature: Springer, International Journal of Material Forming, Formability improvement with independent die and punch temperature control, Bagheriasl *et al.* © 2014 [7].
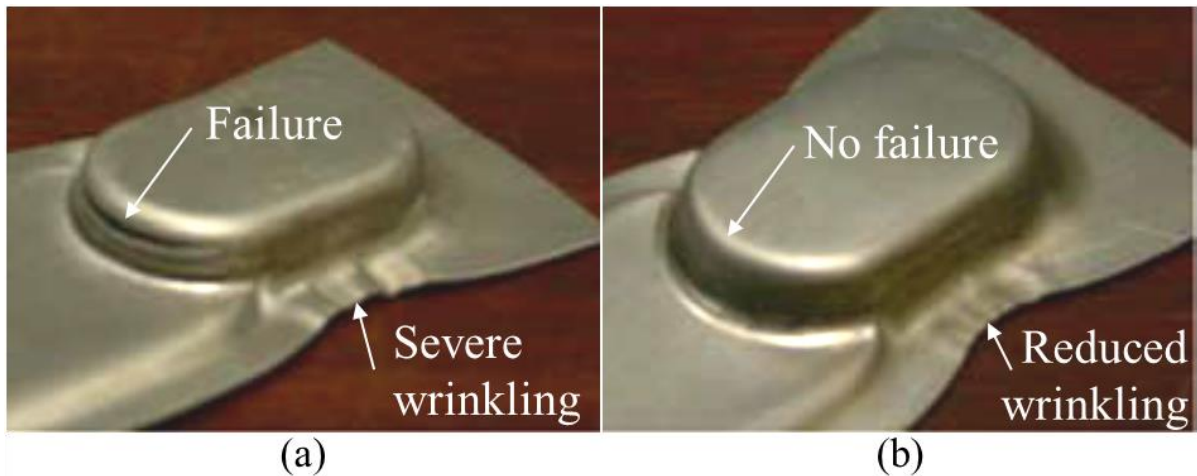
Fig. 2-3 Formed automotive heat exchanger component with a drawn cup feature, formed with a (a) room temperature and (b) 300 °C die. Reprinted with permission from Springer Nature: Springer, International Journal of Material Forming, Formability improvement with independent die and punch temperature control, Bagheriasl *et al.* © 2014 [7].

Warm forming has also proven to be effective in reducing springback of Al brazing sheet, particularly for sheets of greater initial strength, such as work hardened sheet tempers. For a simple "U" channel geometry, springback of work hardened H24 temper sheets was reduced to the same level as fully annealed Al brazing sheet by forming at 250 °C, without a reduction in material strength after forming (Fig. 2-4) [9, 10]. More recently, it was shown that for formed geometries more akin to actual heat exchanger components, a forming temperature of 325 °C was needed to completely reduce springback of H24 sheet to the same level of O temper sheet formed at room temperature [11].
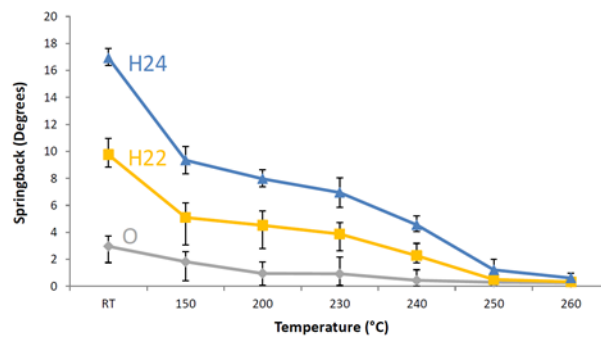
Fig. 2-4 Springback reduction with increasing forming temperature. Image reproduced with permission [36].

2.3. Brazing

Brazing is one of the main materials joining processes, where a liquid filler metal penetrates a gap between the surfaces to be joined, and upon cooling forms a permanent joint. Brazing differs from soldering in that brazing takes place above 450 °C, and differs from fusion welding in that the base materials to be brazed remain solid [23]. In a typical brazed joint, the parts are arranged such that the faces to be joined form a narrow gap (i.e. a capillary). At the brazing temperature, the liquid filler metal infiltrates the gap and is drawn along the length by capillary action [22, 37]. The extent to which the liquid can penetrate the capillary depends on the ability of the liquid filler metal to wet the solid base material, in order to create intimate contact at the solid-liquid interface. For the simple case of a liquid droplet on a solid surface (Fig. 2-5), the contact angle between liquid and solid is a function of the interfacial energies, as described by the Young equation in Eq. 2 [38]:

$$cos\theta = \frac{\gamma_{SV} - \gamma_{SL}}{\gamma_{LV}}$$

Eq. 2

where γ is the interfacial energy for the solid-vapour (SV), solid-liquid (SL), and liquid-vapour (LV) interfaces, respectively, and wetting occurs when $\theta \leq 90°$. By defining the work of adhesion (W_a) between the liquid and solid as in Eq. 3, Eq. 2 can be rewritten as shown in Eq. 4 [39]:

$$W_a = \gamma_{SV} + \gamma_{LV} - \gamma_{SL}$$

Eq. 3

$$cos\theta = \frac{W_a}{\gamma_{LV}} - 1$$

Eq. 4
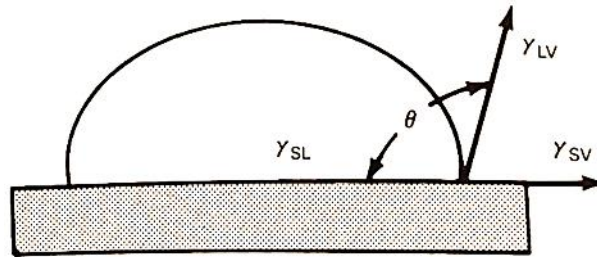
Fig. 2-5 Definition of the contact angle between a liquid and solid, as determined by the balance of interfacial energies. AWS Brazing Handbook 4th Edition:1991, Figure 1.3(A), reproduced with permission from the American Welding Society (AWS), Miami, FL [22].

From Eq. 4, it can be seen that excellent wetting conditions (i.e. $\theta \leq 45°$) can only occur when W_a approaches twice γ_{LV} [40]. Such a condition is only possible with low solid-liquid interfacial energy, such as the case for metallic bonding between an Al alloy base metal and liquid Al filler metal [41]. The solid surface can reduce its free energy by absorbing contaminants from the surrounding environment [22]. Therefore, an essential step in the brazing process is the removal of surface contaminants such as grease, paint, and oxides, to allow good wetting and intimate contact between the liquid and solid [23, 37]. Surface cleaning is particularly important for Al alloy brazing, due to the presence of the tenacious Al oxide layer, which prevents liquid flow and intimate contact at the interface. The Al oxide is usually removed by a potassium fluoroaluminate (KFAl)-based flux (i.e. the NOCOLOK® process) [1], or by using fluxless brazing technology, such as Dana Corporation's proprietary nickel (Ni)-based braze promoter [42, 43].

It should be noted that the contact angle defined by Eq. 2 and Eq. 4 is for non-reactive wetting, and is only a qualitative description if interfacial interactions occur. During brazing, where the liquid filler metal is in contact with a real surface, a number of possible secondary phenomena can occur. For example, the liquid filler metal can dissolve part of the solid base material, increasing the liquid filler metal melting point and causing partial solidification, consequently impairing the liquid flowability [23]. Alternatively, diffusion of alloying elements from the liquid filler into the solid base material can occur at the brazing temperature, again increasing the melting point of the liquid, resulting in isothermal solidification [37]. Spreading of the liquid filler can erode the base material, altering the flowability of the liquid and reducing the remaining thickness of the base material [22]. These secondary phenomena will be discussed in greater detail in section 2.4.

After the surfaces to be joined are cleaned, the components are assembled and fixed together. The fixtures used to hold the work pieces together during brazing apply pressure to the components to ensure that intimate contact is made at the joint faying surfaces, but not so much pressure that the components collapse during brazing. The brazing process is often classified by the method used to heat the assembly [44]. Numerous heating methods, such as manual torch, furnace, induction, resistance, laser, and immersion in molten flux (i.e. dip brazing), have been developed for various brazing and material applications [41]. Each brazing process can be further divided; for example, furnace brazing can be classified as either batch or continuous, depending on the component geometry and production volume, or by whether the furnace atmosphere is an inert gas, a reducing gas, or under vacuum during brazing. Automotive heat exchangers are most often fabricated by controlled atmosphere brazing (CAB), using continuous furnaces, due to the high production volume. Additionally, the filler metal is already present at the joints during assembly, due to the laminate structure of Al brazing sheet, making furnace brazing an even more viable process. During brazing, the assembly typically passes through a number of zones in the furnace, where the temperature of each zone is calibrated to ensure that the assembly is exposed to the necessary temperature profile to allow the filler metal to wet and flow to the joints. During heat exchanger production, the furnace zone temperatures are adjusted such that the assembly experiences a peak brazing temperature between 595 °C and 600 °C for approximately 3 min, and a continuous stream of nitrogen gas is flowed through the furnace to maintain the oxygen level below 100 ppm [1].

In terms of brazed joint configurations, the work pieces and filler metal can be arranged in two general configurations [40]. In the first, the pieces to be joined are arranged to form a capillary, with the filler metal placed outside the gap; upon melting, the liquid is drawn into the gap by capillary action. In the sandwich configuration, the filler metal is placed in the gap between the work pieces prior to brazing, and upon melting, wets the work pieces to form the brazed joint. Given the structure of Al brazing sheets (section 2.1), and the specific application of battery cooling plates under investigation in this thesis, the sandwich configuration is of particular interest. When the filler alloy has excellent wetting of the base material (i.e. $\theta \leq 45°$), there is intimate contact everywhere, and the liquid completely fills the gap. The meniscus of the liquid is outside of the gap, and the joint thickness is reduced (Fig. 2-6) [40].
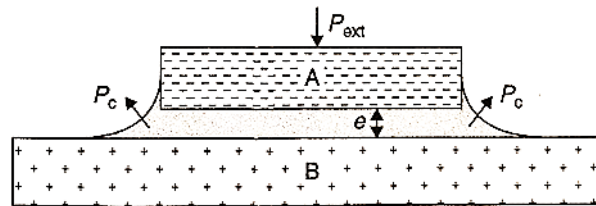
Fig. 2-6 Sandwich-type brazed joint configuration for when excellent wetting conditions between liquid filler alloy and solid base materials exist. Image reproduced with permission [40].

In the Al brazing sheet system, the liquid clad alloy provides the filler metal for the brazed joints throughout the heat exchanger assembly. Zhao and Sekulic [45] proposed that melting of the clad alloy was a diffusion controlled, non-equilibrium process, where melting initiates at the clad alloy grain boundaries, and the newly formed liquid is in local equilibrium with the solid grain. Melting progresses at the boundary of the shrinking clad grains, until the overall composition within the grain reaches the solidus composition at the brazing temperature. Capillary forces and surface tension draw the liquid to the joint faying surfaces, while the solid solution clad grains remain in place at the sheet surface and do not contribute to joint formation. This solid solution layer was referred to as the 'clad residue', and can be seen in Fig. 2-7a. The clad residue has been characterized by Gao *et* al. to be of uniform thickness and to have a planar interface with the core, indicating that no interface migration occurs [46, 47]. No microstructure evidence for diffusion controlled melting was provided by Zhao and Sekulic. However, Nylen *et al*. [16] presented a series of micrographs throughout clad melting, where liquid was observed

16

to first form at clad grain boundaries, and a band of non-melted clad grains were present at the interface with the core alloy at higher temperatures (i.e. the clad residue). On the other hand, Woods [12] showed that clad alloy melting initiated at the clad-core interface, where the melting point is locally reduced due to the diffusion of elements from the core (i.e. Mg and Cu), and progressed to the surface of the sheet. Melting of the clad alloy is clearly a complex phenomenon, particularly in the initial stages of the process.
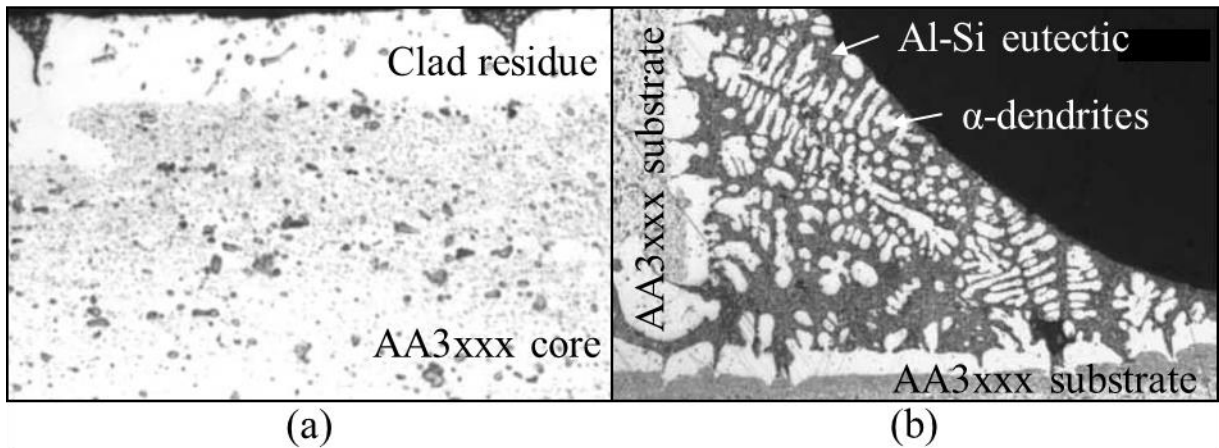
Fig. 2-7 Post-braze microstructure (a) far away from joints (i.e. clad residue) and (b) at brazed joint locations. Reprinted from International Journal of Heat and Mass Transfer, vol. 48, Sekulic *et al.*, Dendritic growth in Al–Si alloys during brazing. Part 1: Experimental evidence and kinetics, pp. 2372-2384 © 2005, with permission from Elsevier [48].

The liquid clad alloy, which accumulates at the joint faying surfaces throughout the assembly, solidifies to form the permanent brazed joint upon cooling of the assembly (Fig. 2-7b). Prior work has shown that the brazed joint topography observed in Fig. 2-7b can be predicted by minimizing the liquid clad membrane potential energy (E_P) given in Eq. 5 [46]:

$$E_P = E_s + E_g + E_w \qquad \text{Eq. 5}$$

where E_s is the surface energy of the liquid membrane with the atmosphere, E_g is the gravitational potential energy of the liquid brazed fillet, and E_w is the energy associated with the wetted interface. Minimization of the potential energy requires minimizing the sum of the three energy terms, and has shown to accurately predict brazed fillet topography for a number of brazing temperatures.

Since the liquid is essentially a binary Al-Si alloy, the main phases present after solidification can be predicted from the Al-rich end of the binary phase diagram (Fig. 2-8). Upon cooling from the liquid phase, primary Al-Si solid solution α-dendrites first begin to grow from the core alloy surface [48]. The volume fraction of α-dendrites increases with higher brazing temperatures, due to increased dissolution of the core by the liquid clad during the dwell at the brazing temperature. Dendrites continue to grow as the assembly is further cooled, and eventually the remaining liquid solidifies to form the Al-Si eutectic structure. Core alloy dissolution by the liquid clad at the brazed joint has been reported to lead to the presence of α-Al(Mn, Fe)Si particles on the surface of the re-solidified joint [17, 20].
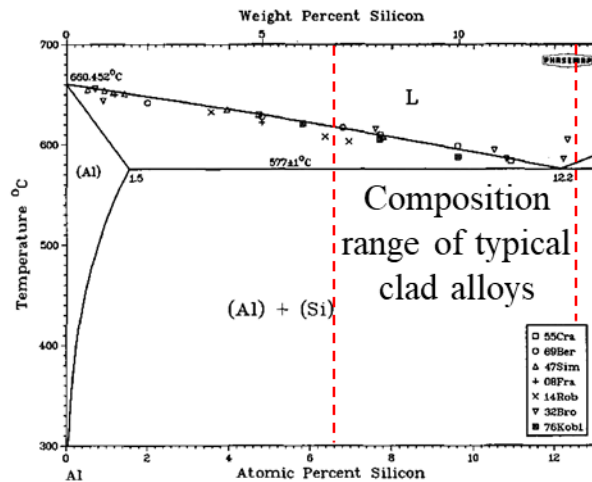
Fig. 2-8 Al-rich end of the binary Al-Si phase diagram used to predict phases present in re-solidified clad alloy. Reprinted by permission from Springer Nature: Springer, Bulletin of Alloy Phase Diagrams, The Al-Si (Aluminum-Silicon) System, Murray and McAlister © 1984 [49].

2.4. Secondary Phenomena During Brazing

Due to the thermomechanical processing history and multi-alloy nature of the Al brazing sheet, a number of phenomena secondary to braze joint formation can occur, which can alter the brazing performance and corrosion resistance of the sheet. This section describes a number of the secondary phenomena relevant to warm forming.

18

2.4.1. Solid State Diffusion

During warm forming, the Al brazing sheet is held at the forming temperature during forming. Due to the composition difference of the brazing sheet layers, a diffusion couple is naturally established when the sheet is heated, where Si diffuses out of the clad and into the core. While "long life" brazing sheets are designed to take advantage of the inward diffusion of Si to form the "band of dense precipitates" in the core (section 2.5), extensive Si diffusion reduces the mass of clad alloy which melts upon reaching the brazing temperature, impairing the formation of brazed joints.

Terrill [50] observed that a region of the clad alloy adjacent to the core became depleted of Si when the sheet was held at high temperatures, as shown schematically in Fig. 2-9. The Si content in the depleted zone is sufficiently reduced such that the melting temperature increases and, consequently, the zone does not melt upon reaching the brazing temperature. Consequently, the depleted zone does not contribute to brazed joint formation.
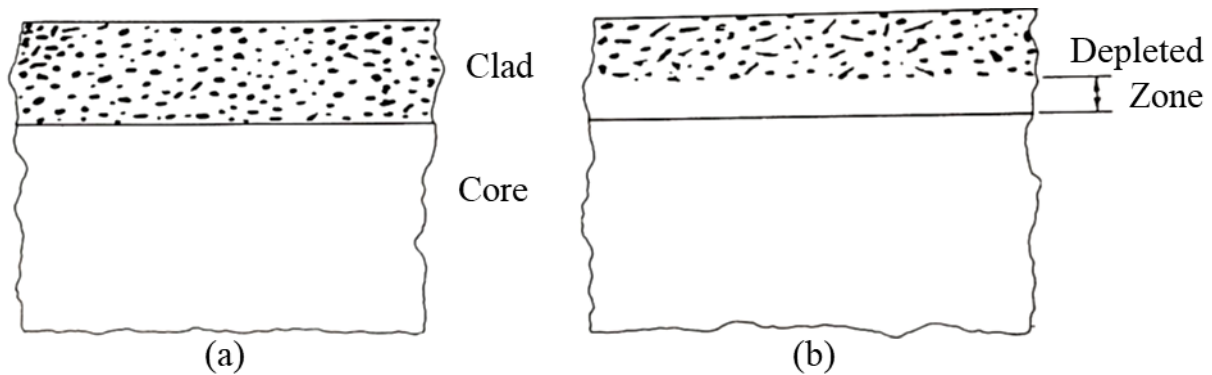
Fig. 2-9 Clad alloy thickness (a) before and (b) after a high temperature isothermal hold. The Si-depleted zone develops adjacent to the clad-core interface, as indicated by the reduction of Si particles in this region. Reprinted from Welding Journal (May, 1966) © American Welding Society, with permission [50].

An analytical solution for the depleted zone thickness as a function of isothermal hold time and temperature was derived from Fick's second diffusion law and conservation of mass (Eq. 6) [50].The amount of Si from the depleted zone thickness (area abcf in Fig. 2-10) was equated to the area under the diffusion profile (area bcde). Assuming the Si concentration in the clad layer remains constant and equal to the solid solubility at the test temperature, the depleted zone thickness (in cm) was shown to be:

$$y = 1.1284\sqrt{Dt}\,\frac{c_0}{c_i} \qquad\qquad \text{Eq. 6}$$

where c_i is the nominal clad alloy Si composition, c_0 is the solid solubility of Si in Al at the test temperature, t is the isothermal hold time, and D is the Si diffusion coefficient. The model was shown to be in excellent agreement with experimental measurements of the depleted zone thickness.
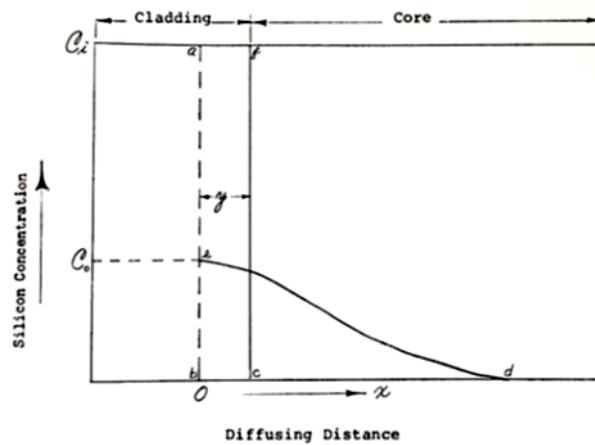
Fig. 2-10 Development of Si diffusion profile in the core alloy due to the formation of the depleted zone. Reprinted from Welding Journal (May, 1966) © American Welding Society, with permission [50].

Turriff *et al.* [51] studied the suppression of liquid clad formation due to solid state diffusion, by measuring the reduction in melting peak area after high temperature holds using differential scanning calorimetry (DSC), where the melting peak area is proportional to the mass of clad alloy undergoing melting. While a continual decrease in melting peak area was found with increasing hold time at 500 °C, the authors concluded that the reduction of liquid clad alloy formation due to solid state diffusion of Si was insignificant, particularly compared to the clad loss after melting. Benoit *et al.* [52] corroborated these findings, showing that clad loss due to Si solid state diffusion was significant only for holds above 500 °C. However, it was experimentally shown that a depleted zone at least 3 µm thick forms during heating to the brazing temperature if the heating rate is 20 °C/min or less, even in the absence of a high temperature hold. Such a depleted zone thickness may be significant for braze joint formation, particularly

20

for thinner sheets with correspondingly thin clad layers. Since warm forming of Al brazing sheet is performed below 325 °C, a depleted zone greater than what forms during heating to the brazing temperature is not expected to develop as a result of warm forming. Thus, clad loss due to solid state diffusion will not be given further consideration in this thesis.

2.4.2. Core Alloy Recovery and Recrystallization

As previously noted, dislocations are imparted to the Al brazing sheet during forming, which are a source of stored energy. While dislocations are thermodynamically unstable and should be eliminated spontaneously, this is not the case, as the atomistic processes required to do so are sluggish at room temperature [24]. The basic principle behind annealing heat treatments of metals is to provide the activation energy required for the processes that reduce the stored energy associated with the deformed microstructure. During heat exchanger production, the brazing temperature profile is a (non-isothermal) heat treatment for the deformed sheet. This section discusses the two main processes which can occur in the core alloy during brazing: recovery and recrystallization.

During heating of lightly deformed sheet, rearrangement and annihilation occurs by dislocation glide and climb to form lower energy, metastable sub-structures, such as dislocation cells and sub-grains. As the dislocations are not fully eliminated, these sub-structures represent a source of stored energy (E_D), as indicated by Eq. 7:

$$E_D = \frac{3\gamma_s}{D} \qquad \text{Eq. 7}$$

where γ_s is the sub-structure boundary specific energy and D is the sub-structure diameter. The final recovered microstructure depends on the level of applied strain and annealing time, as noted in the Nes model [53], where finer sub-structures are obtained with greater applied strain and shorter annealing times. The recovered microstructure stored energy is problematic for Al brazing sheet, as it provides a driving force for liquid clad penetration into the core during brazing (section 2.4.3).

Full recovery is limited to lightly strained materials. As the amount of applied strain increases, the driving force for recrystallization also increases. If substantial recovery occurs

during annealing, recrystallization may be inhibited due to a reduced driving force; conversely, if recrystallization occurs during annealing, eliminating stored deformation energy, recovery can not occur [24]. Two recrystallization mechanisms relevant to Al brazing sheet are discussed here: strain induced boundary migration (SIBM) and the nucleation and growth of new grains.

Recrystallization in Al alloys which are moderately deformed (i.e. up to 20 %) has been shown to be dominated by SIBM [54], shown schematically in Fig. 2-11. The driving force for SIBM is a difference in stored deformation energy across an existing grain boundary, which may originate from a difference in dislocation accumulation rates during deformation. During SIBM, part of a pre-existing boundary bulges into an adjacent grain of higher stored energy, leaving the region behind the migrating boundary with a lower dislocation density. It has been shown that the SIBM can initiate from a single or multiple sub-grains, depending on the extent of recovery which has occurred. In either case, the critical radius for grain boundary bulging is directly proportional to the grain boundary energy, and inversely proportional to the difference in stored energies across the boundary [24, 55]. Second phase particles exert a pinning pressure on the boundary, which increases the critical radius for SIBM.
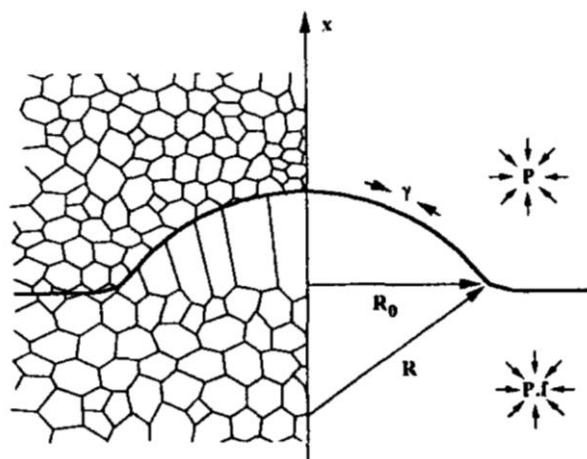
Fig. 2-11 A segment of a pre-existing grain boundary bulging into a grain of higher stored energy due to SIBM, lowering the dislocation density in area behind the migrating boundary. Reprinted from Scripta Materialia, vol. 36, Bate and Hutchinson, A re-evaluation of the mechanism of SIBM, pp. 195-198 © 1997, with permission from Elsevier [55].

A coarse and elongated microstructure characteristic of SIBM has been found in studies of Al brazing sheet, and has been correlated with good predicted brazing performance [56, 57].

An example of SIBM in Al brazing sheet strained between 5 % and 10 % and subjected to a simulated brazing heat treatment can be seen in Fig. 2-12.
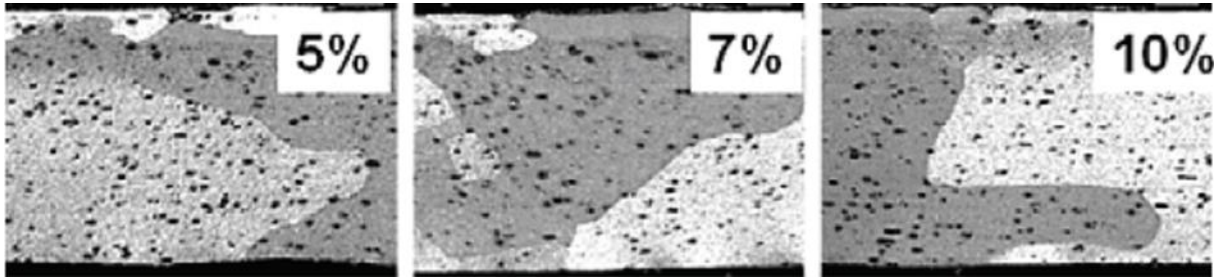
Fig. 2-12 SIBM in the post-brazed core alloy of Al brazing sheet strained between 5% and 10% prior to brazing. The core alloy grains are elongated and have a thickness in the order of the sheet thickness. Image reproduced with permission [57].

Recrystallization by nucleation and growth of new grains becomes significant at levels of deformation greater than what is required for SIBM. A number of empirical laws have been developed to describe the relationship between thermomechanical processing and recrystallization [58]; a sub-set of the laws most pertinent to the current work are as follows:

1. *Recrystallization requires a minimum amount of deformation to occur.* The deformed microstructure provides nucleation sites for new grains, and the deformation energy provides the driving force for the growth of new grains.

2. *The recrystallized grain size is inversely related to the level of deformation.* As the amount of deformation increases, more nucleation sites are provided per unit volume.

3. *The recrystallization temperature decreases with increasing deformation.* The driving force for recrystallization increases with strain, allowing nucleation and growth to occur at lower temperatures.

4. *Increasing the deformation temperature increases the recrystallization temperature.* Dynamic recovery can occur during elevated temperature forming, reducing the accumulation of stored energy, and delaying the onset of recrystallization to higher temperatures.

23

Nucleation and growth is particularly relevant for the microstructural evolution of sheet products with different levels of rolling reduction from the cast ingot, such as Al brazing sheets in the H temper. It has been shown that the recrystallized grains of cold rolled sheets tend to be elongated along the rolling direction [2, 21]. In particular, Puchi-Cabrera *et al*. [59] showed that the recrystallized grains in cold rolled and non-isothermally annealed AA3003 sheet were elongated, due to the alignment of second phase particles along the rolling direction, which pin grain boundaries and retard growth in the transverse direction. Furthermore, a number of studies related to the recrystallized microstructures of rolled Al brazing sheet have come to the same conclusion: coarse recrystallized grains are desirable for enhanced brazing performance, compared to fine recrystallized grains, as the coarse grains limit the number of high diffusivity grain boundaries for liquid clad penetration [60, 61, 62, 63]. The variation in recrystallized grain size after simulated brazing, with the corresponding sheet sagging distance (SD), can be seen in Fig. 2-13 for various rolling reduction and annealing temperature combinations. As a large sagging distance indicates loss of sheet rigidity during brazing and is therefore undesirable, the benefit of a coarse recrystallized grain size is clearly demonstrated in the figure.
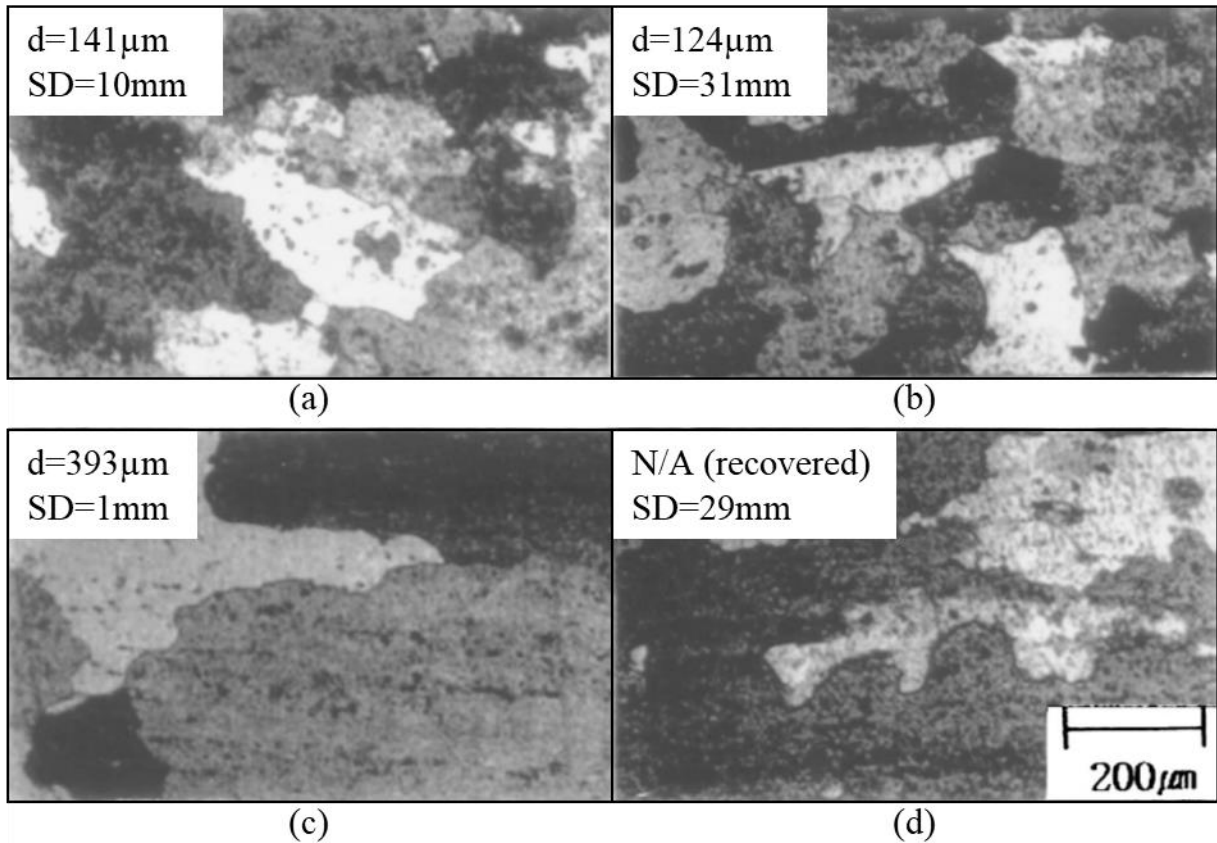
Fig. 2-13 Post-brazed core alloy microstructure, recrystallized grain size (d), and sagging distance (SD) for sheets inter-annealed at/cold rolled to (a) 327°C/30%, (b) 327°C/45%, (c) 417°C/30%, and (d) 417°C/10%. Reprinted by permission from Springer Nature: Springer, Journal of Materials Science Letters, Sagging resistance of cold rolled aluminum 4343/3N03/4343 clad sheet, Yoon *et al.* © 2001 [56].

2.4.3. Liquid Film Migration

The liquid clad alloy exists on the surface of the solid core alloy during brazing, due to the clad alloy liquidus temperature being lower than the core alloy solidus. As a result, a number of interactions can occur between the liquid clad and solid core during brazing. Wittebrood [14] grouped the interactions discussed in literature into three general categories:

1. *Core alloy dissolution:* a static liquid clad alloy dissolves part of the core alloy surface, increasing the total liquid volume and the volume fraction of α-dendrites formed in the brazed joint during solidification.

25

2. *Core alloy erosion:* liquid clad alloy flowing under the influence of an external force, such as gravity or capillary action, locally dissolves the core alloy in the region where the liquid flows, reducing the core thickness.

3. *Liquid film migration (LFM):* the movement of a liquid clad film through the sheet thickness causes local core dissolution, and the re-distribution of alloying elements in the region the liquid film has passed through.

LFM has been observed in a number of material systems as outlined by Yoon [64], and results in a number of characteristic microstructural changes. The phenomenon was first characterized in Al brazing sheets by Woods [12], where the occurrence of LFM during brazing reduced the liquid clad flow by up to 75 %, and was therefore considered detrimental to brazing. LFM in Al brazing sheet has been shown to depend on the level of strain applied to the sheet prior to brazing. Given that the objective of this thesis is to understand the relationship between warm forming and brazing, the remainder of this section focuses on LFM. The LFM mechanism in Al brazing sheet is described in the following paragraphs, and is shown schematically in Fig. 2-14.
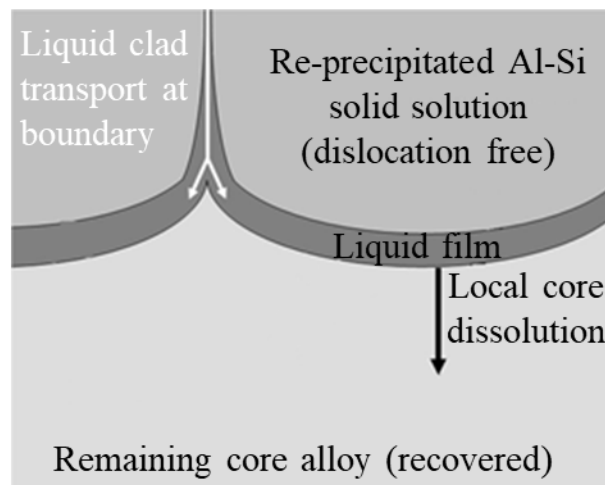
Fig. 2-14 Schematic representation of the LFM process in Al brazing sheet. Image modified with permission [14].

When the liquid clad which forms during melting is not drawn away to a joint by surface tension, it is attracted to the grain boundaries at the core alloy surface by capillary action, and

completely wets the boundaries [65]. Since the wetted boundary has a lower energy than high angle (solid) grain boundaries, the wetted boundary is able to migrate with a smaller critical radius or stored energy than what is required for strain induced boundary migration (SIBM) [14]. As the liquid film begins to migrate, the core alloy directly ahead of the film dissolves, reducing the remaining core layer thickness. Furthermore, the liquid film dissolves second phase particles in the core as it passes, enriching the film with Mn, Fe, and Cu [12, 16]. It has also been shown that if the film accumulates large quantities of heavier alloying elements, such as Fe, regions of the film begin to drag and eventually detach as discrete pools behind the film [57, 66].

As the film migrates, a solid solution consistent with the equilibrium solidus composition (i.e. Si-rich) is precipitated in the region behind the film [67, 68], which is reported to epitaxially grow from the clad grains originally at the interface with the core [12, 69]. Thus, as the liquid film moves, it continually loses Si to the newly precipitated solid solution. In order for the film to remain liquid, it must be replenished with Si, which has been shown to occur by Si transport from the remaining liquid clad at the sheet surface, along the boundaries of the precipitated grains, and to the migrating film [14, 70]. By removing Si from the remaining clad alloy, LFM causes partial solidification of the remaining liquid filler alloy, impairing brazing performance [16, 71]. The solid solution precipitated behind the film (i.e. the LFM affected area), is void of second phase particles, confirming that they are dissolved by the film. Due to the high alloying content of the film, a band of intermetallic particles develops at the interface with the remaining core alloy when the film solidifies.

The extent to which LFM occurs depends on the amount of strain imparted to the Al brazing sheet prior to brazing, where the depth of LFM into the core alloy has a non-linear relationship with applied strain [69]. The relationship between LFM and applied strain has been shown to be related to the core alloy microstructure after brazing. In Fig. 2-15, the ratio of the clad alloy solidification energy after simulated brazing to the initial melting energy, which indicates the relative amount of liquid clad alloy lost during brazing, was a non-linear function of applied strain [57]. The post-braze microstructures for a number of strains are also shown. It can be seen that for conditions where the energy ratio was lowest (i.e. 2 % - 4 % strain), the microstructure consisted of a fine-grained core alloy, and large blocky grains at the sheet surface protruding into the core, characteristic of the LFM-affected area. A clear difference in microstructure was found at higher strains (i.e. 8 %), where the core was characterized by coarse

grains, which were attributed to SIBM (section 2.4.2), and no LFM was observed at the sheet surface.
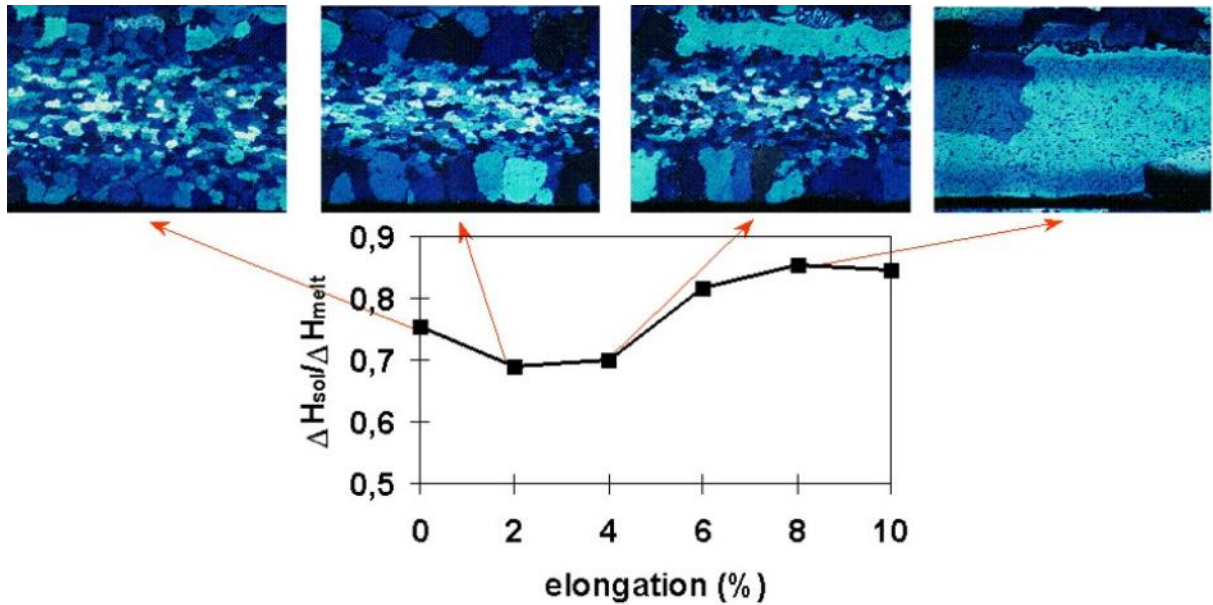
Fig. 2-15 The effect of applied strain on the relative amount of liquid clad remaining after a brazing heat treatment, a measure of the extent of LFM, and the post-braze microstructure. Image reproduced with permission [14].

Numerous LFM driving forces have been proposed in literature. The most comprehensive analysis of the proposed driving forces was conducted by Wittebrood [14], where the viability of each driving force was first evaluated on a free energy change basis. After eliminating proposed mechanisms with a positive free energy change, the remaining driving forces were evaluated through additional analysis of experimental observations. At the end of the analysis, it was concluded that the most feasible driving force was the reduction of stored deformation energy in the core alloy by the passage of a liquid film. As a result, LFM in brazing sheet was proposed to be a special case of the general process, differing in driving force but resulting in the same microstructure changes, and was classified as strain induced LFM. Beginning with the driving pressure for grain boundary migration during recrystallization, the driving pressure (P) for LFM was derived by Wittebrood to be:

28

$$P = \frac{\alpha \rho_f G b^2}{2} + \frac{2\gamma_b}{R}$$

<div align="right">Eq. 8</div>

where α is a constant equal to 0.5, ρ_f is the dislocation density in front of the liquid film, G is the shear modulus, b is the Burgers vector, γ_b is the grain boundary energy, and R is the radius of the grain growing into the deformed structure. It was proposed that as the liquid film moves, it consumes dislocations in the core alloy, reducing the stored energy, and leaves a dislocation-free solid solution (i.e. the affected area) in its wake [14]. Unfortunately, conclusive evidence for a recovered core alloy after brazing in samples where LFM occurred was not presented in Wittebrood's study, although some residual stored energy was observed. However, a recovered core alloy ahead of the liquid film and dislocation free region behind the liquid film was shown in other studies [65, 72].

According to Eq. 8, the driving pressure for LFM monotonically increases with the dislocation density in the core alloy, and thus is in competition with recrystallization for the same driving force. Three possible outcomes of this competition to reduce stored energy during brazing were noted, as shown schematically in Fig. 2-16. In lightly strained Al brazing sheet (1 in Fig. 2-16), the dislocation density in the core alloy is too low to trigger either recrystallization or LFM during brazing. The post-braze microstructure in this case is characterized by a non-recrystallized core alloy with a re-solidified clad alloy at the sheet surface (e.g. leftmost micrograph in Fig. 2-15). As more strain is imparted to the sheet, the stored energy increases (2 in Fig. 2-16), and recovery occurs in the core alloy during heating to the brazing temperature. Upon reaching the clad alloy melting temperature, the recovered sub-structure provides a sufficiently high driving pressure for LFM to occur (e.g. center two micrographs in Fig. 2-15). As the strain is further increased (3 in Fig. 2-16), the dislocation density is sufficiently high to trigger recrystallization during heating, resulting in a coarse grained core alloy with a significantly reduced dislocation density. Upon reaching the clad alloy melting temperature, the driving pressure for LFM is eliminated, and the liquid clad alloy remains at the surface (e.g. rightmost micrograph in Fig. 2-15).
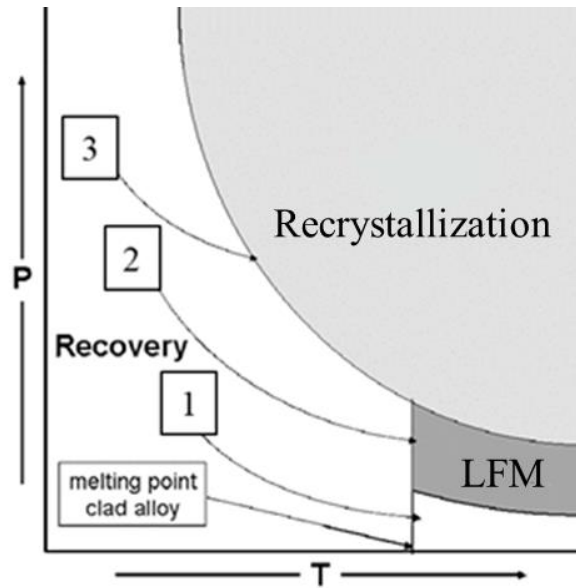
Fig. 2-16 Competition between recrystallization and LFM during heating for Al brazing sheet with varying levels of applied strain (i.e. different stored energy driving forces, P). Image modified with permission [14].

2.5. Corrosion of Al Brazing Sheet

As manufacturers use thinner gauge Al brazing sheets in heat exchanger production, sheet perforation due to corrosive attack is a concern [13]. A number of corrosion modes have been identified in automotive heat exchangers, including galvanic, pitting, intergranular, crevice, and erosion corrosion [1]. Some of these attack modes can be attributed to component design (e.g. crevice) or operating parameters such as coolant velocity (e.g. erosion). In some instances, galvanic corrosion is used to provide cathodic protection to critical component (e.g. coolant tubes), by joining them to fins made from less noble alloys (e.g. Zn-containing AA7xxx series). Pitting, intergranular, and (micro) galvanic corrosion modes depend on the phases present at the microstructure level and the service environment, and are the focus of this section.

The progression of corrosive attack through the brazing sheet when exposed to a chloride (Cl⁻)-containing environment was first described by Isobe *et al*. [13]. The heat exchanger external surface may be exposed to chlorides from, for example, de-icing road salts, while chlorides could be present at the internal surfaces if contaminated make-up water is used in *lieu* of antifreeze. As previously discussed, the main phases present at the re-solidified surface of the sheet include primary Al-Si solid solution (in the form of α-dendrites, the LFM affected area, or the clad residue), eutectic Al, and eutectic Si. Using measured composition data from each phase,

the corrosion potentials (vs. saturated calomel electrode) were calculated to be -0.85 V, -0.84 V, -0.83 V, and -0.26 V for the core alloy, eutectic Al, primary Al, and eutectic Si, respectively. Thus, the eutectic Al was calculated to be 10 mV less noble than the primary Al, and is coupled to the relatively noble Si particles in the eutectic structure. As a result, preferential anodic dissolution of the eutectic Al phase occurs, with the cathodic reaction proposed to occur predominantly on the Si particles. However, Meijers [19] argued that while Si assists in initiating corrosion, the Si needles are not a strong cathode. The corrosive attack then progresses intergranularly, toward the interface between the re-solidified clad and core alloy, where intermetallic particles may be present, and a pit forms at the interface. An example of corrosive attack through the re-solidified clad layer, after anodic polarization to 1 V above the sheet open circuit potential in a 5 wt% sodium chloride (NaCl) solution, can be seen in Fig. 2-17 [73]. From the figure, it is clear that corrosion initiates at the grain boundaries between the primary Al grains, and progresses intergranularly toward the interface. From section 2.4.3, it can be understood why LFM is undesirable from a corrosion standpoint. The Si penetration between the LFM-affected area grains provides a convenient pathway for corrosive attack deep into the core, and the intermetallic particles present at the interface make the region more susceptible to corrosive attack. As the corrosive attack continues, the pit environment becomes more acidic, and the Cl^- concentration increases to maintain electro-neutrality. At this point, the pit becomes self-sustaining [74], and progresses through the remaining core alloy, which was the least noble phase.
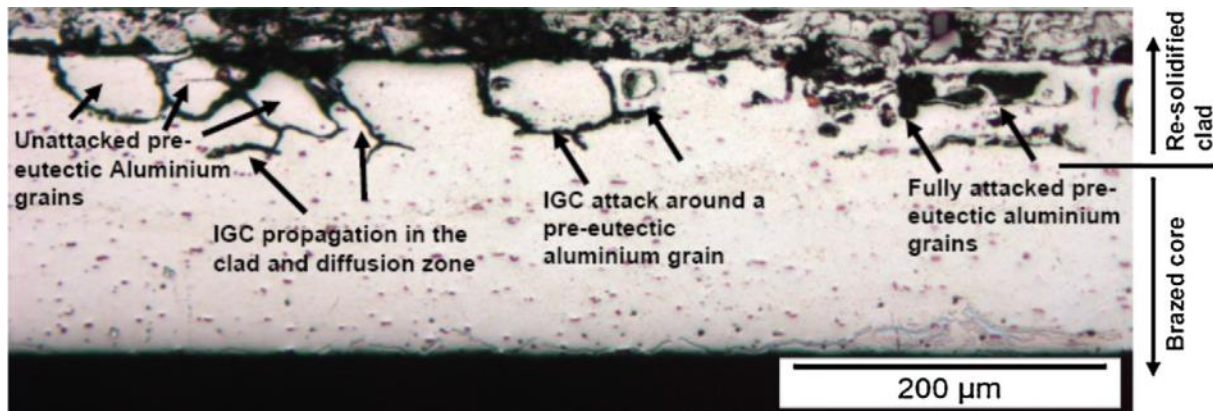
Fig. 2-17 Microstructure of brazed sheet after 1V anodic polarization above open circuit potential in 5 wt% NaCl solution. Reprinted from Electrochimica Acta, vol. 104, Norouzi Afshar *et al.*, A combined electron probe micro analysis and scanning Kelvin probe force microscopy study of a modified AA4xxx/AA3xxx aluminium brazing sheet, pp. 48-63 © 2013, with permission from Elsevier [73].

While Si diffusion can suppress liquid clad formation, it has also been used to improve corrosion resistance in so-called 'long life' brazing sheets. These sheets are reported to have at least a five-fold increase in the time to sheet perforation in the Sea water acetic acid test (SWAAT), a severe accelerated corrosion test environment, compared to conventional AA3003 and AA3005 alloys [2]. The enhanced corrosion resistance is achieved through the formation of a sacrificial layer called the 'band of dense precipitates' (BDP). As previously noted, Mn is present in the core as second phase particles and in super saturated solid solution with the Al matrix. When Si diffuses into the core alloy, Mn is forced out of solution to form α-Al(Mn, Fe)Si particles [19]. Due to the lower Mn content in solid solution, the corrosion potential of the core matrix in the diffusion zone becomes more negative than the remainder of the core by approximately 30 mV; this slight difference in corrosion potentials has been shown to be sufficient to change the corrosion morphology [3]. The BDP formation is enhanced by super-saturation of Mn in the core matrix prior to brazing, which can be achieved by not homogenizing the core ingot, and maintaining a low Si content in the core prior to brazing. The BDP effect has been shown to be even more effective if the core alloy contains Cu, since Cu diffuses from the core toward the Cu-lean clad alloy [20]. The Cu diffusion leads to a depletion of Cu in solid solution in the BDP region, resulting in a more negative corrosion potential. However, Norouzi Afshar *et al.* showed that Cu can accumulate in the eutectic structure of the re-solidified clad, increasing the susceptibility to intergranular corrosion [20]. The net effect of the post-braze

alloying element distribution on the calculated corrosion potential through the sheet thickness is presented in Fig. 2-18.
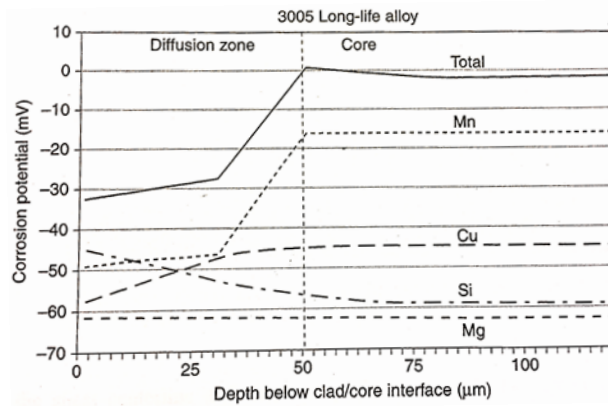
Fig. 2-18 Calculated corrosion potential through the thickness of the Al brazing sheet due to the re-distribution of alloying elements after brazing. Image reproduced with permission [1].

When the corrosive attack reaches the BDP in the long life alloys, the attack is deflected laterally rather than through the sheet thickness, due to the more negative corrosion potential of the matrix in the diffusion zone. An example of the typical corrosion morphology for a long life sheet is given in Fig. 2-19, after exposure to the SWAAT environment for 6 weeks. Clearly, the corrosive attack has been restricted to the surface of the sheet, rather than progressing through the thickness of the core.
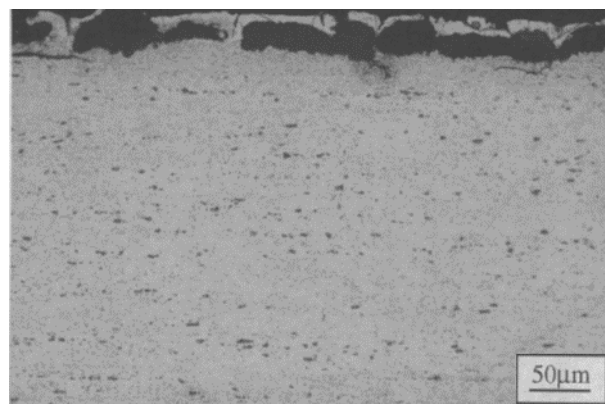
Fig. 2-19 Corrosion morphology of long life brazing sheet after 6 weeks exposure to the SWAAT environment. Reprinted by permission from Springer Nature: Springer, Metallurgical and Materials Transactions A, Microstructural control in an aluminum core alloy for brazing sheet applications, Marshall *et al.* © 1993 [3].

33

2.6. Summary

Warm forming has emerged as a promising technique for the production of innovative Al alloy heat exchanger technologies, by increasing the forming limits of Al brazing sheets, and enabling the use of higher strength sheets by reducing springback. The relationship between room temperature sheet deformation, post-brazed microstructure, and corrosion resistance have been well studied. However, no assessment of the brazing and corrosion performance of warm formed Al brazing sheet has been conducted. The following chapters present the first studies to elucidate the relationship between warm forming and brazing performance, and discuss the implications of this relationship on the in-service corrosion performance of warm formed and brazed assemblies.

3. Effect of Sheet Temper, Strain, and Forming Temperature on Metallurgical Reactions During Brazing[1]

3.1. Introduction

Warm forming is a promising manufacturing technique to improve forming limits and component flatness of multi-layered Al brazing sheet. However, metallurgical reactions that occur between the clad and core during brazing have not been studied for warm formed sheet. An understanding of how an increase in forming temperature changes the microstructure that evolves during brazing and the severity of liquid film migration (LFM) is needed; this chapter details the research conducted to investigate this relationship.

In this chapter, the strains imparted to the sheet during forming were simulated by performing interrupted tensile tests on Al brazing sheet dog bone specimens at room temperature (RT) and 250 °C. To determine the effect of the initial sheet condition on the response to forming temperature and predicted brazing performance, fully annealed (i.e. O), and work hardened and partially annealed (i.e. H24) sheet tempers were used. Differential scanning calorimetry (DSC) has previously been shown to be a powerful method to quantify the rate of solid-liquid interactions during brazing [43, 51]. It has also been shown that DSC is capable of discriminating between slight differences in initial sheet condition (i.e. grain size and applied strain), and that thermal data have a strong correlation with measured braze joint fillet area [71]. Therefore, DSC was used in this chapter to quantify the kinetics of the metallurgical interactions occurring between the clad and core alloys during brazing, to elucidate the effect of warm forming on brazing performance. The thermal analysis results were corroborated with microstructure analysis and chemical composition measurements.

3.2. Experimental Procedure
3.2.1. Materials and Sample Preparation

Industrially produced Al brazing sheet, comprised of a modified AA3003 core alloy and a single AA4045 clad layer, was used in the current investigation. The compositions of both Al

---

alloy layers are given in Table 3-1. The core alloy composition was determined by performing inductively coupled plasma optical emission spectrometry (ICP-OES) after removing the clad alloy layer by chemical etching with a sodium hydroxide (NaOH) solution. Prior to etching, the core alloy was masked with tape, and etching progressed until at least 30 µm of sheet thickness was removed from the clad layer surface. The clad alloy composition was then calculated by performing ICP-OES on the full brazing sheet, and subtracting the weighted core alloy composition. The measurements were conducted by Cambridge Materials Testing, and were performed in accordance with ASTM E1479 and ASTM E1097 [75, 76].

Table 3-1 Composition of the Al alloys used in the brazing sheet in wt% (bal. Al).

Sheet Layer	Si	Mn	Cu	Fe	Other
Clad	9.19	-	0.11	0.10	≤0.08
Core	0.18	0.86	0.64	0.33	≤0.08

Industrially produced brazing sheets with two different initial sheet conditions (i.e. tempers) were used in the current investigation. Fully annealed (i.e. O temper) sheet was used as a baseline to determine the effect of applied strain and forming temperature on brazing kinetics. Sheets which were work hardened and partially annealed to half hardness (i.e. H24 temper) were also studied, as these sheets exhibit greater strength and experience a greater level of springback after forming [9, 10, 11]. The starting microstructures for each sheet temper are given in Fig. 3-1. The O temper sheet microstructure was revealed by etching the cross section with Keller's reagent. The core alloy was characterized by a number of small grains from annealing, as well as larger elongated grains left over from the prior rolling during sheet production. Chemical etching was not able to reveal the microstructure of the H24 sheet, due to the highly deformed and elongated (i.e. pancaked) core alloy grains. Therefore, the H24 sheet microstructure was revealed using a FEI Helios NanoLab 650 focussed ion beam (FIB) microscope, using gallium ions (Ga$^+$) and an accelerating voltage of 30 kV, and subsequent imaging of the surface by scanning electron microscopy. Both sheet tempers had a nominal sheet thickness of 200 µm, with a clad layer between 10 % (H24) and 13 % (O) of the total sheet thickness. Clad layer and overall sheet thickness measurements for both sheet tempers are given in Table 3-2. The Al brazing sheets described in this section were used for all of the experiments contained in this thesis, so only modifications to the material will be described in subsequent chapters, as required.
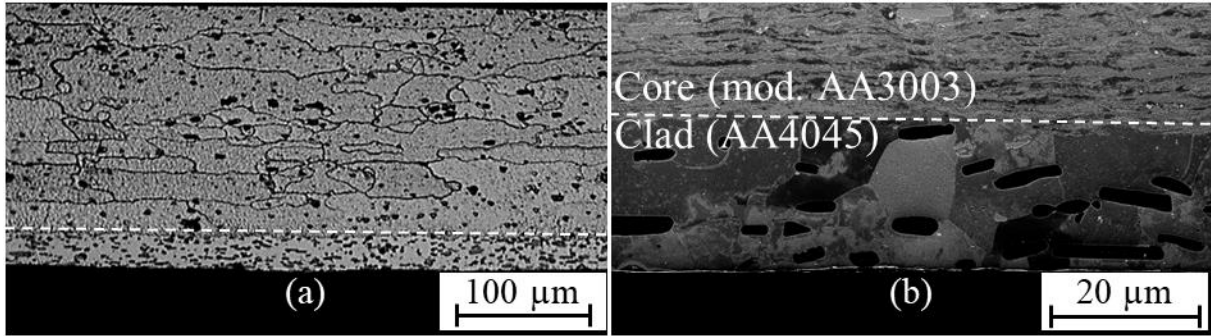
Fig. 3-1 Initial core grain structure of (a) O and (b) H24 sheet tempers. Cross sections were taken along the sheet rolling direction.

Table 3-2 Measured clad layer and overall sheet thicknesses of O and H24 sheets (n=10).

Sheet Temper	Overall Sheet (µm)	Clad Layer (µm)
O	202.7 ± 1.5	25.8 ± 1.2
H24	203.2 ± 0.5	22.3 ± 1.1

Forming was simulated by uniaxial stretching of the Al brazing sheet tensile specimens along the sheet rolling direction, using a tensile tester (Instron model 5697) equipped with a furnace (Instron model 3119-606). All tensile tests were performed at CanmetMATERIALS in Hamilton, ON. The tensile specimens had a nominal gauge length and width of 19 mm (0.75") and 12.7 mm (0.5"), respectively. The sample geometry used for these tests was originally used for superplasticity tensile tests, but has also been used for soft and thin sheets, to avoid bending or twisting of the gauge length. The sample temperature was measured by clamping a thermocouple to the sheet surface at each of the tensile grips, and attaching a third thermocouple to the backside of the sample gauge length. A ventilation fan within the furnace chamber was also used to ensure temperature uniformity along the sample length. Prior to testing, the tensile specimens were allowed to equilibrate with the furnace, which took up to 30 min for forming at 250 °C. Interrupted tensile tests were performed between 2 % and 12 % engineering strain, using a crosshead speed of 0.75 mm/min, resulting in an average strain rate of $6.6 \times 10^{-4}\,\text{s}^{-1}$ for a nominal gauge length of 19 mm. Strain was recorded using an MTS video extensometer, using two points spaced approximately 12.7 mm apart along the gauge length; all uniaxial strains reported throughout this thesis are the average value between the extensometer markers. Samples of each sheet temper were stretched at RT, to determine the baseline dependence of LFM on applied strain. Warm forming was simulated with tensile tests performed at 250 °C, since improved

formability and springback reduction have been demonstrated at this temperature [7, 8, 9, 10, 11].

3.2.2. Differential Scanning Calorimetry

Differential scanning calorimetry (DSC) is a thermal analysis technique, in which the temperature difference between a sample and a reference is measured as a function of test temperature. The sample, and a reference mass when required, are placed in separate crucibles, which are then placed on a platform within the DSC, referred to as the measuring head. Two thermocouples are located on the underside of the measuring head, directly below the sample and reference crucibles, in order to measure the temperature difference between the sample and reference. A correction file using two empty crucibles is performed prior to the test, to remove the thermal effects of the equipment from the thermal data. During the test, when a thermal event such as clad alloy melting occurs within the sample, the sample temperature begins to lag behind the reference, since additional heat input is required to continue to raise the sample temperature [77]. The additional heat flow appears as a peak in the thermal data and, after calibration of the measurement equipment, the integrated area below the peak is directly proportional to the mass of material undergoing the thermal event.

A cyclic temperature profile (Fig. 3-2), which was originally developed by Corbin *et al.* [43], was used to quantify the rate of liquid clad alloy penetration into the core alloy during brazing. Samples were heated to a peak temperature of 600 °C to fully melt the clad alloy, held isothermally for 1 min, and were then cooled to 530 °C to completely solidify the remaining clad; this cycle was repeated until no liquid clad remained. Clad alloy melting began at 574 °C during each heating segment, as indicated by the top row of red dots in Fig. 3-2, and an endothermic peak appeared in the DSC data during each cycle. Conversely, solidification of the remaining liquid clad ended around 550 °C (i.e. the bottom row of red dots) during each cooling segment, which resulted in an exothermic peak in the data. The amount of Si present in the clad alloy is reduced during each temperature cycle, due to Si diffusion from the liquid into the core alloy or by the formation of the LFM affected area, both of which increase the melting point of the remaining clad and, consequently, reduces the amount of clad which can melt during the subsequent cycle. Since the peak areas are proportional to the mass of clad alloy undergoing the

38

phase change [77], the reduction in the melting peak area with an increasing number of thermal cycles was used to estimate the remaining clad alloy as a function of time.
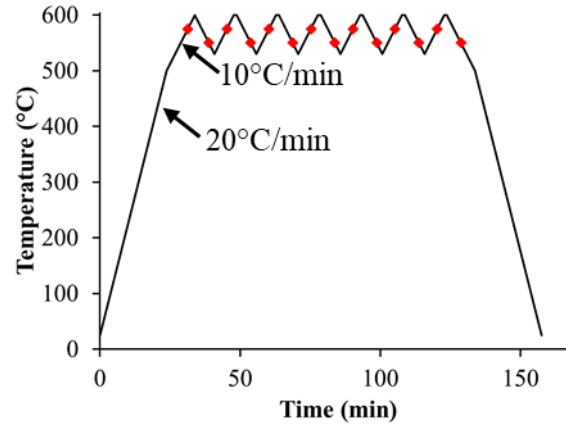
Fig. 3-2 Cyclic temperature profile used to study the rate of liquid clad alloy depletion during simulated brazing. Clad melting initiation and solidification completion are indicated by points on heating and cooling segments, respectively.

DSC samples 4.8 mm in diameter were manually punched from between the extensometer markers along the gauge length of the tensile test samples, with the punch pin in contact with the core layer, and were placed in alumina crucibles with the clad layer facing up. The crucible was then placed on the sample side of the DSC measuring head, and an empty crucible was used on the reference side. A Netzsch DSC 404C Pegasus instrument, calibrated to within ± 1 °C of the melting onset temperature of pure Al and within ± 2.6 % of the heat of fusion, was used for the experiments. A baseline correction file with empty crucibles was performed to remove machine and crucible effects from the thermal data. The furnace chamber was evacuated and subsequently back filled with 99.999 % purity nitrogen gas at a flow rate of 150 mL/min throughout testing. Heating and cooling rates were 20 °C/min below 500 °C and were lowered to 10 °C/min above 500 °C, to reduce lag in the thermal data [78]. Three replicates were conducted for each sheet temper-forming temperature-strain combination to demonstrate reproducibility; all reported thermal data are the average of three replicates, and error bars correspond to the standard deviation of measured melting peak areas for the three trials.

3.2.3. Microstructure and Composition Analysis

Additional samples were punched from between the extensometer markers along the gauge length of the strained samples to investigate metallurgical changes which occur within the sheet during brazing. The DSC was used as a controlled atmosphere furnace, using the same conditions as detailed in the preceding section, with the exception of the temperature profile. To simulate brazing, samples were heated to 600 °C, held for 10 min, and were subsequently cooled, using the same heating and cooling rates as before. Samples were mounted such that the microstructure along the sheet rolling direction was visible in the cross-section, prepared for metallographic analysis using progressively finer sandpaper grit and diamond particle size, and etched with Keller's reagent for 110 s to reveal the post-braze core microstructure. A Hitachi SU 3500 scanning electron microscope (SEM), equipped with an energy dispersive x-ray spectroscopy (EDS) detector operated in spot mode using an accelerating voltage of 15 kV and acquisition time of 100 s, was used to obtain composition data to qualitatively confirm the occurrence of LFM during simulated brazing. The composition measurements were performed on the Al matrix in both the clad and core alloys, avoiding second phase particles.

3.3. Results
3.3.1. Warm Forming

Experimental stress-strain curves for both sheet tempers and forming temperatures are given in Fig. 3-3. Work hardening was observed over the entire range of strains studied during RT stretching of the O temper sheet. Due to the highly deformed initial condition of the H24 temper sheet, negligible work hardening was observed during RT stretching, and the ultimate tensile strength was reached at approximately 5 % strain. A slight decrease in the stress-strain data was observed beyond 5 % strain, indicating that necking occurred. The implications of strain non-uniformity at higher strains on the material characterization results will be discussed in sections 3.3.2 and 3.3.3.
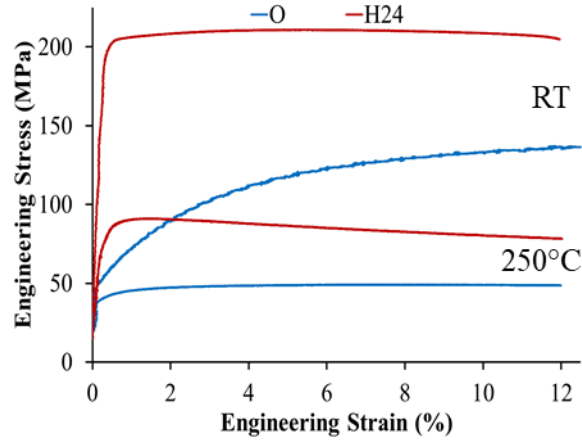
Fig. 3-3 Experimental stress-strain curves of O and H24 temper Al brazing sheet during stretching at RT and 250 °C.

Thermal softening and reduced work hardening were observed in Fig. 3-3 for both sheet tempers when the forming temperature was increased to 250 °C. The stress-strain curve for the O-250 °C condition is relatively flat compared to the RT curve, which, according to the Bergstrom model [26], suggests that at the relatively low strain rate used, the rate of dislocation re-mobilization is comparable to the rate of dislocation generation. Further inspection of the tensile data revealed that there was a very slight decrease in the stress around 8 % strain, indicating that necking occurred. The decrease in stress during forming is more apparent for the H24-250 °C condition, where the ultimate tensile strength was reached almost immediately, after which the tensile curve displayed a negative slope, indicative of necking. Part of this reduction could also be attributed to dynamic recovery by thermally activated mobilization of dislocations in the highly cold worked material, and this will be discussed further in section 3.4.2. As discussed in section 2.2, material deformation at elevated temperatures becomes less dependent on strain hardening and more dependent on strain rate hardening. While uniform elongation decreases due to the reduction in work hardening, the amount of non-uniform elongation to failure increases by the development of a diffuse neck, due to positive strain rate sensitivity [30]. As noted by Ghosh [79], strain changes gradually through a diffuse neck, and for practical purposes, much of the post-uniform elongation may be considered uniform. Moreover, as noted by Hosford and Duncan [80], deformation within a diffuse neck usually occurs over a length approximately equal to the width of the sample. This was confirmed by Kahl *et al.* [81], who showed that the length of a diffuse neck in AA3003 samples strained at 250 °C was nearly twice

41

the width of the sample. Thus, for the warm formed uniaxial samples in this thesis, necking is assumed to be diffuse rather than localized, and the strain through the gauge length is assumed to be relatively uniform. Again, this assumption will be discussed in sections 3.3.2 and 3.3.3.

3.3.2. Differential Scanning Calorimetry

For a single temperature cycle, the liquid duration time (LDT) is defined as the time between the onset of clad melting during heating at the eutectic temperature of 574 °C to the time when the last liquid solidifies during cooling around 550 °C. The LDT for a single temperature cycle is indicated in the heat flow trace Fig. 3-4. The thermal analysis results in this section are plotted against the cumulative LDT, since liquid clad can penetrate the core alloy along grain boundaries as soon as liquid forms [12]. For this study, the effect of applied strain and forming temperature on brazeability was inferred by the total LDT from all temperature cycles, until no liquid clad remained. Poor brazeability was inferred for forming conditions which had a short LDT, as this suggested that liquid clad filler metal would be rapidly depleted. As seen in Fig. 3-5, there is a continual decrease in the melting peak area with an increasing number of temperature cycles. However, it can also be seen from the figure that the number of melting peaks before complete liquid clad loss (i.e. zero peak area) depended on the level of applied strain.
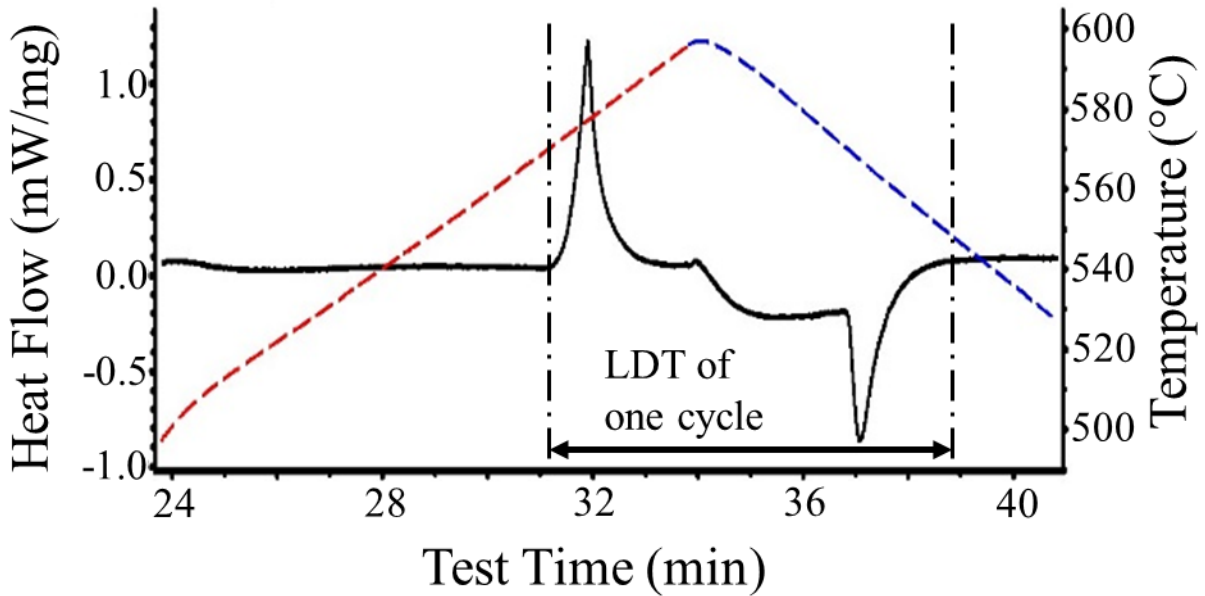
Fig. 3-4 The LDT for a single temperature cycle is the time between the onset of clad melting and the end of solidification, indicated by the vertical dashed lines. The temperature profile during heating and cooling is indicated by the dashed red and blue lines, respectively.
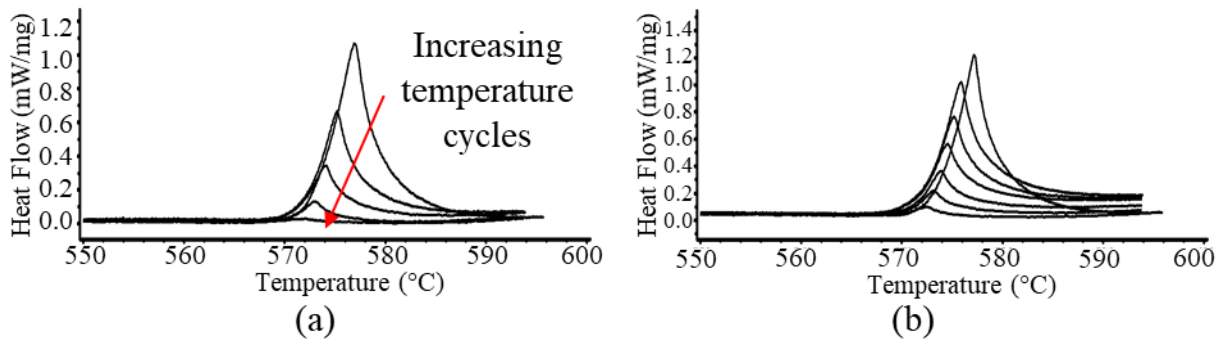
Fig. 3-5 Melting peak area reduction with an increasing number of temperature cycles for O temper sheet stretched at RT to (a) 4 % and (b) 10 % engineering strain.

When the melting peak area from each temperature cycle was measured and plotted against the cumulative LDT, there was a continual decrease in peak area with increasing LDT for all forming conditions (Fig. 3-6). It is clear from Fig. 3-6a and b that the rate of melting peak area reduction was not the same at all levels of strain in the O temper sheet. Fig. 3-6a revealed that the rate of melting peak area reduction did not change monotonically with RT applied strain, while Fig. 3-6b showed that the reduction in melting peak area became more rapid with increasing applied strain at 250 °C. From Fig. 3-6c and d, the melting peak area for H24 sheet

also decreased with increasing LDT; however, no obvious dependence of the rate of peak area reduction on applied strain and forming temperature was observed. Furthermore, it can be seen that the H24 temper thermal data have excellent repeatability in all cases, as evidenced by the small error bars, which suggests that any strain non-uniformity caused by necking in the samples does not impact the thermal data. Indeed, in many cases the error bars for the thermal data corresponding to the relatively highly strained H24 temper sheet are smaller than those of the O temper data, where the strain distribution in the gauge length is more uniform.
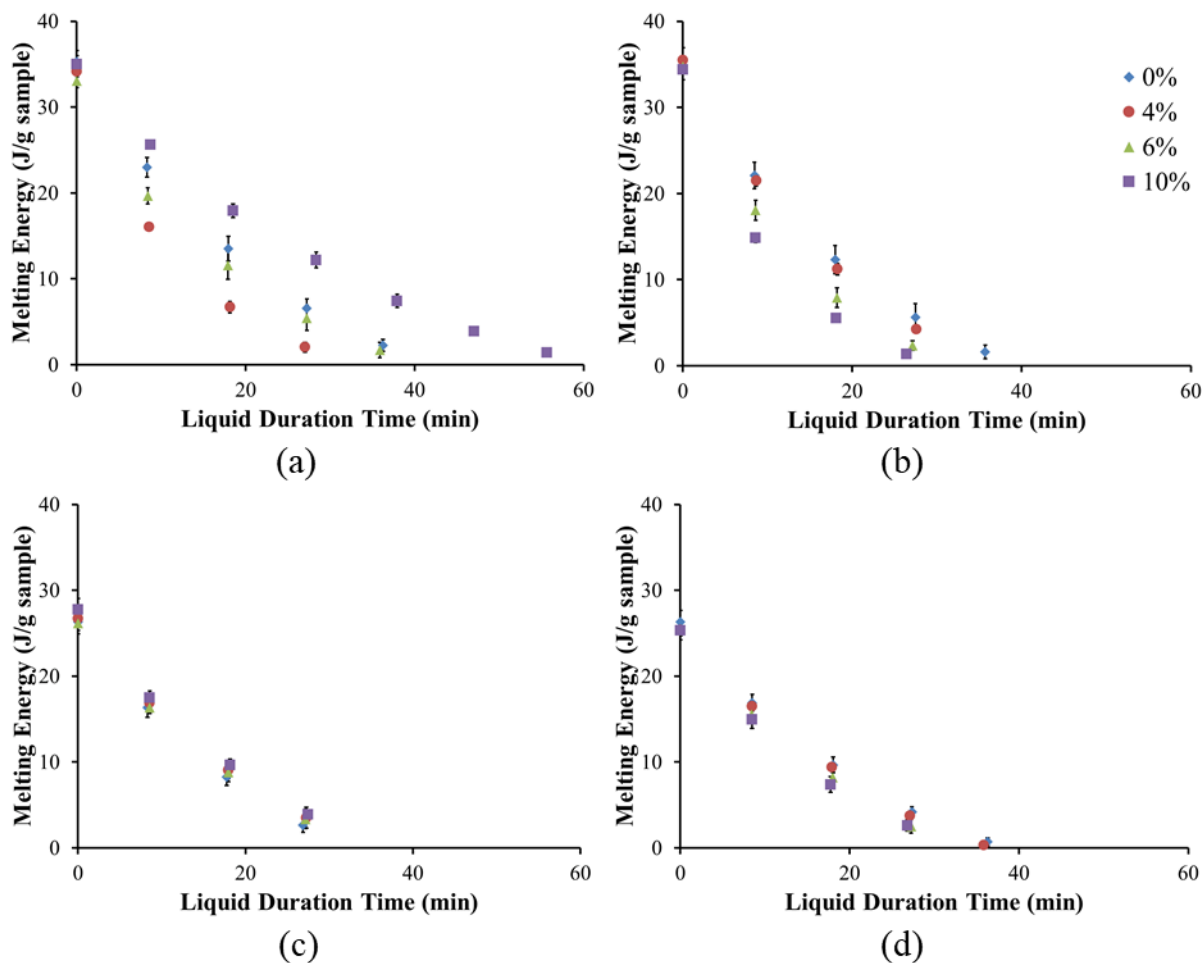
Fig. 3-6 Melting peak area reduction with increasing LDT after forming to different levels of engineering strains for (a) O-RT, (b) O-250 °C, (c) H24-RT, and (d) H24-250 °C forming conditions.

3.3.3. Microstructure and Composition

Post-braze microstructures and composition measurements for a number of forming conditions are given in Fig. 3-7 to Fig. 3-11. The dependence of the O temper post-braze microstructure on RT applied strain can be seen in Fig. 3-7. At 4 % strain (Fig. 3-7a), the core grains were similar to the pre-braze condition (Fig. 3-1a), but large grains similar in morphology to those characteristic of LFM were found protruding into the core alloy at the sheet surface. The large surface grains were also void of second phase particles, even in the areas where the core alloy was originally. When the strain was increased to 6 % and 12 % (Fig. 3-7b and c), a dramatic change in the core grain structure from the pre-braze condition was observed, where the post-braze core was characterized by very coarse grains elongated along the sheet rolling direction. Drastic changes of this nature have been previously attributed to recrystallization by strain induced boundary migration (SIBM) during brazing [57, 70]. LFM attack on the core alloy in these conditions was consequently reduced or eliminated, and a residual clad layer of relatively uniform thickness was observed, with some Al-Si eutectic phase present at the sheet surface.
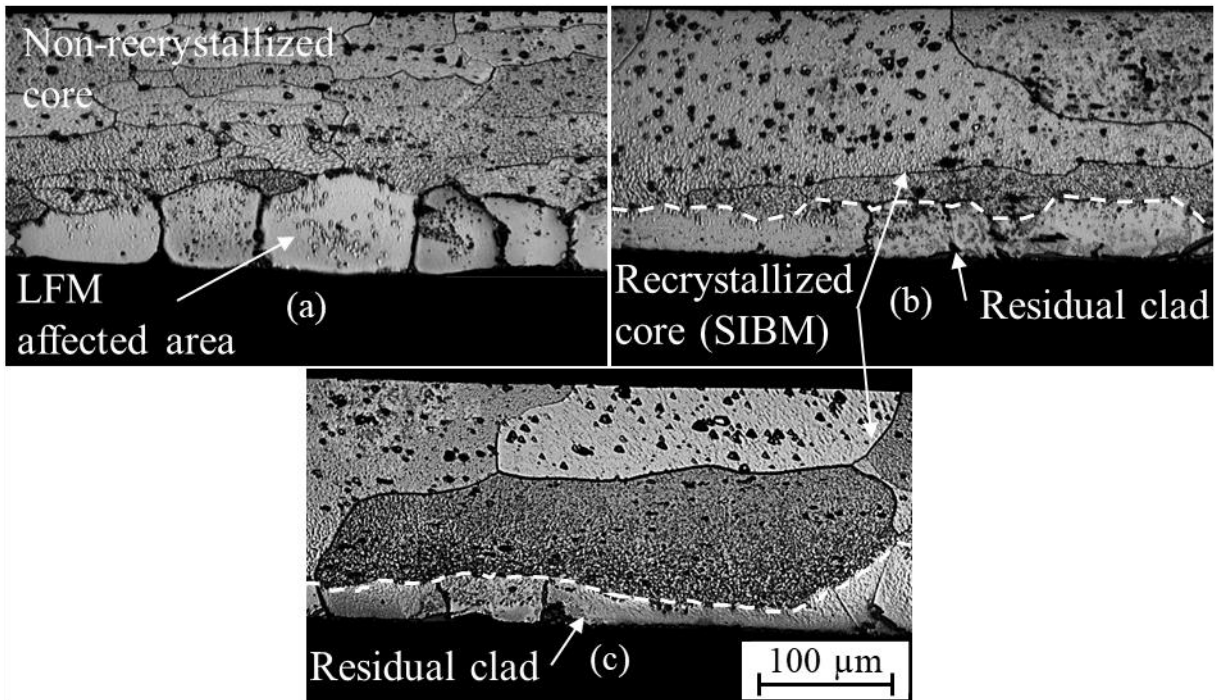
Fig. 3-7 Post-braze microstructure for O temper sheet formed at RT to engineering strains of (a) 4 %, (b) 6 %, and (c) 12 %. The LFM-area affected is indicated in (a), and the approximate interface between the core and residual clad is indicated by the dashed white line in (b) and (c).

45

EDS measurements of Si and Mn concentration after simulated brazing of RT formed O temper sheet are given in Fig. 3-8. For the sample strained to 4 %, the Si level through the LFM grains at the sheet surface was high, around the solidus composition of Si in Al at 600 °C, while beyond these grains, a diffusion profile was observed far into the core. Over the same distances, the Mn level was observed to be very low in the LFM grains, after which a diffusion profile opposite that of Si was observed until the concentration approached the initial core level. On the other hand, for the sample strained to 10 %, the maximum Si concentration near the sheet surface was less than in the 4 % strained sample, and the diffusion profile into the core was markedly shorter.
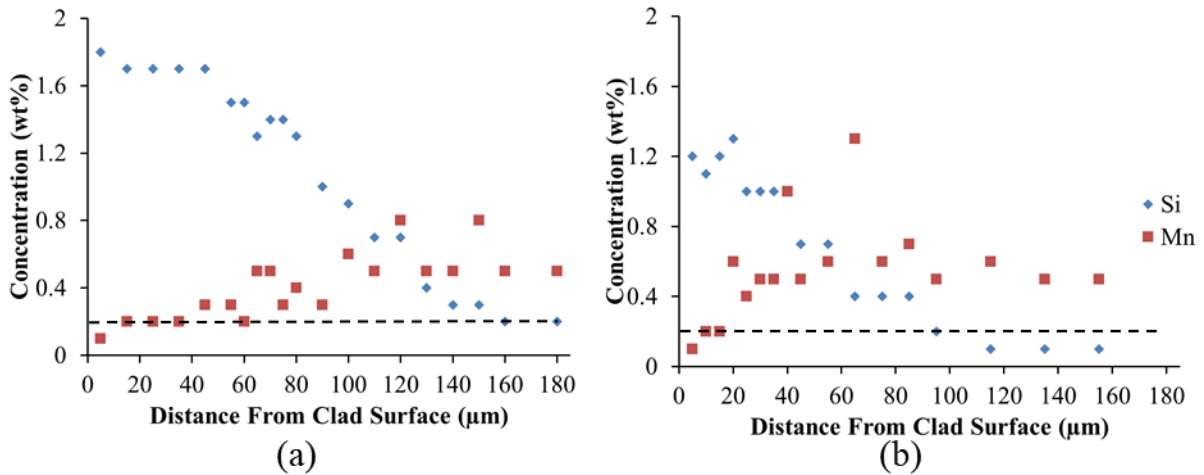
Fig. 3-8 Through-thickness EDS measurements of Si and Mn concentrations after simulated brazing of the O-RT forming condition strained to (a) 4 % and (b) 10 % engineering strain. Si content of the core alloy as measured by ICP-OES is indicated by the dashed line.

Post-brazed micrographs of warm formed O temper sheet are given in Fig. 3-9. The core grain microstructures were largely unchanged from the pre-braze condition, in that a number of small grains remain throughout the core in all cases. Large, precipitate-free grains characteristic of LFM were observed at the sheet surface, even at 10 % strain. Composition measurements (Fig. 3-10) were similar to O temper sheet stretched to low strains at RT (Fig. 3-8a), with regards to the depth of the LFM affected area and long diffusion profile into the core. Unlike the O-RT strained sheets, the composition measurements did not show a dependence on the level of applied strain.
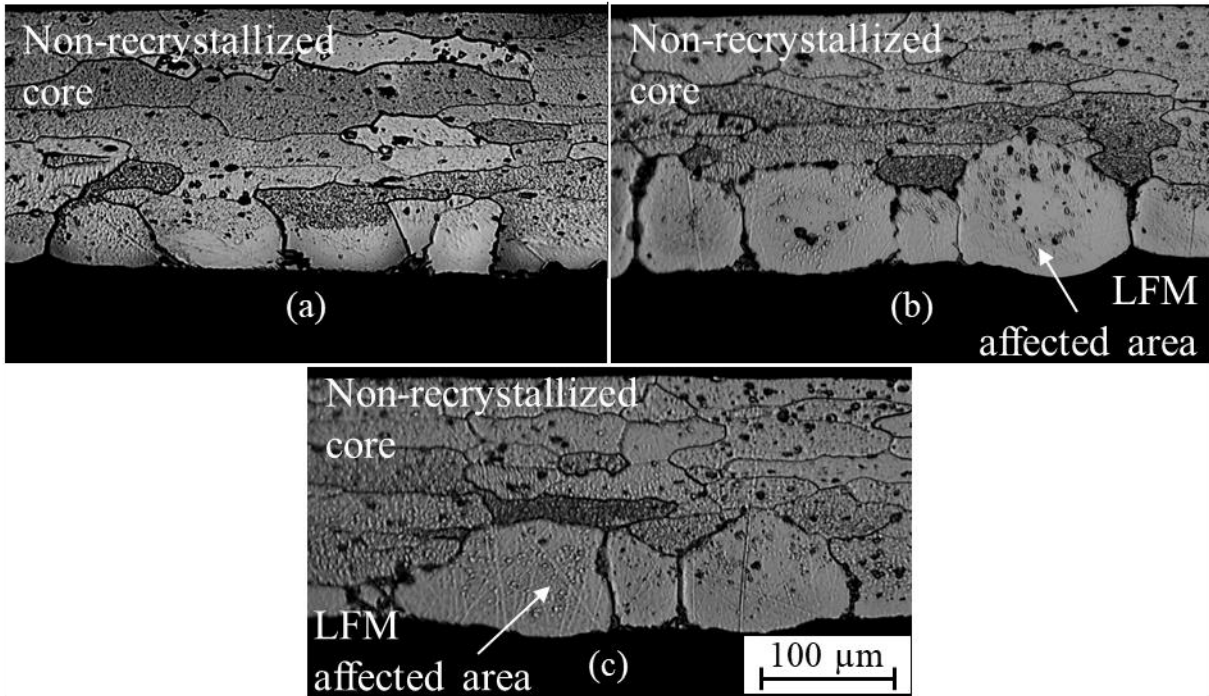
Fig. 3-9 Post-braze microstructure for O temper sheets formed at 250 °C to (a) 4 %, (b) 6 %, and (c) 10 % engineering strain. Areas affected by LFM are indicated in (b) and (c).
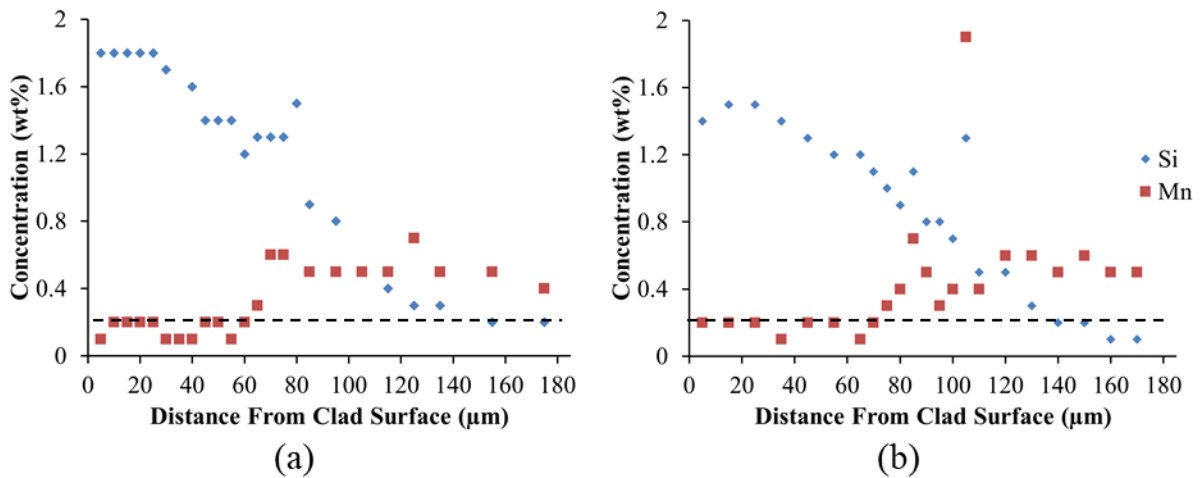
Fig. 3-10 Through-thickness EDS measurements of Si and Mn concentrations after simulated brazing of the O-250 °C forming condition strained to (a) 4 % and (b) 10 % engineering strain. Si content of the core alloy as measured by ICP-OES is indicated by the dashed line.

H24 post-brazed microstructures are shown in Fig. 3-11. A clear difference from the pre-braze condition (Fig. 3-1b) was observed. While the core layer was initially characterized by very thin deformed grains, the core was comprised of coarse recrystallized grains after brazing.

47

The recrystallized microstructure and a thin, relatively uniform clad residue layer was observed in all forming conditions. Most important was the microstructure of the warm formed H24 sheet (Fig. 3-11c); although the sheet was strained at 250 °C, recrystallization still occurred during simulated brazing. Again, despite necking occurring in the sample during forming (localized or diffuse), the microstructure evolution in the sheet during brazing was not affected, due to the level of deformation imparted to the sheet to achieve the H24 temper. The H24 temper core alloy was able to recrystallize at all levels of strain, and any localized increase in strain due to a neck would only further increase the driving force for recrystallization. It is worth noting that while the H24 core grains recrystallized, the grain size appeared to be smaller than those resulting from SIBM (Fig. 3-7b and c). The H24 composition data (Fig. 3-12) suggested similar characteristics to recrystallized O temper sheet (Fig. 3-8b), which indicated liquid clad penetration into the core during brazing was not extensive.
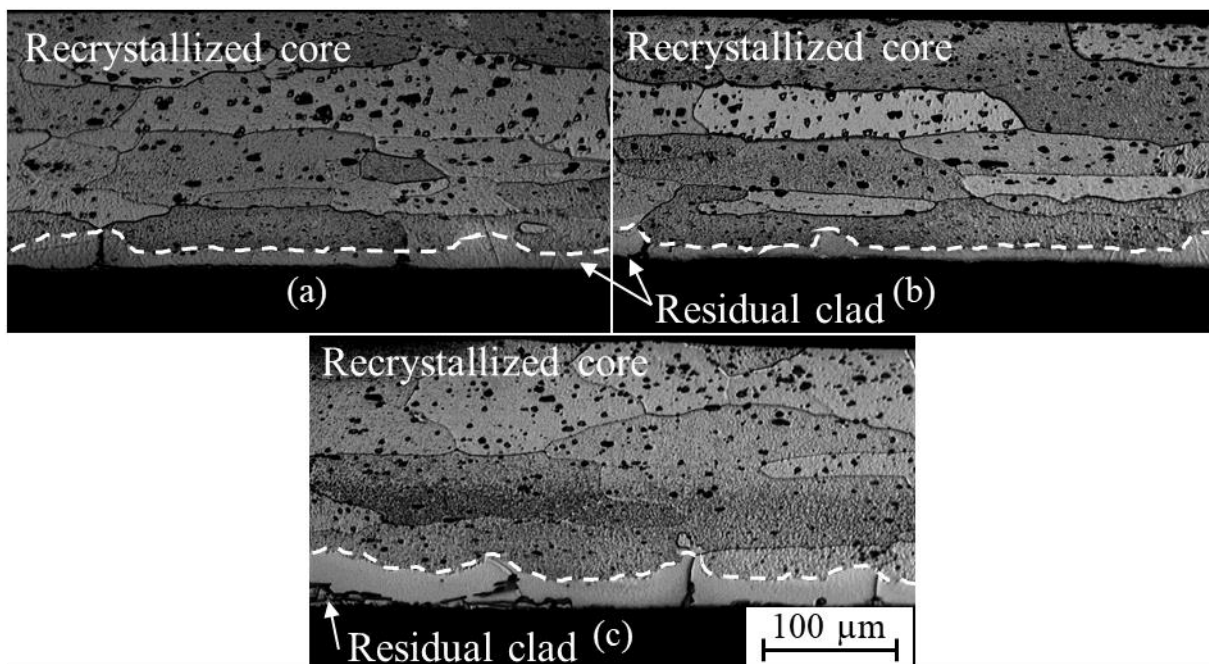
Fig. 3-11 Post-braze H24 microstructure (a) in the as-received condition, and after 6 % applied strain at (b) RT and (c) 250 °C. The estimated position of the interface between the core and residual clad layer is indicated by the dashed white line.
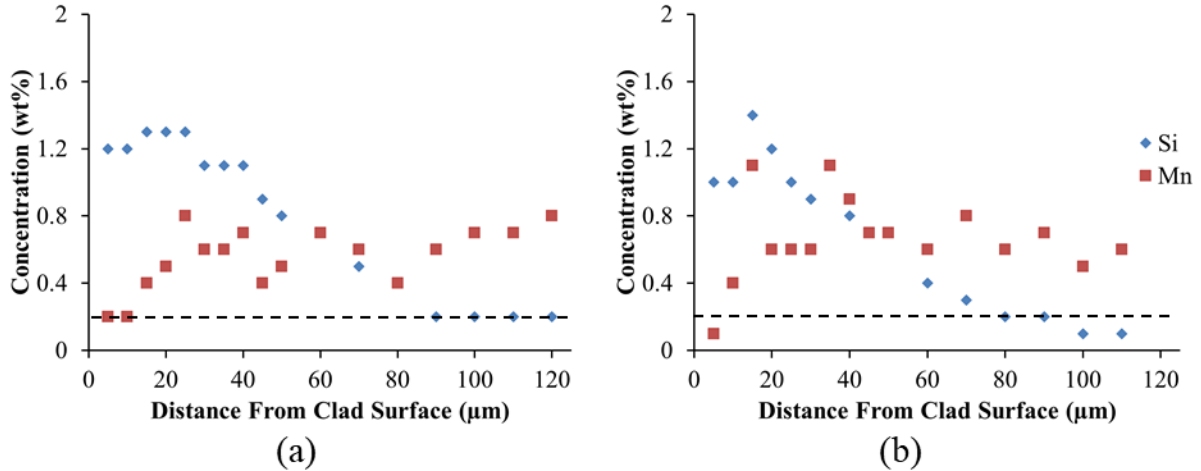
Fig. 3-12 Through-thickness EDS measurements of Si and Mn concentrations after simulated brazing of H24 temper sheet strained to 6 % engineering strain at (a) RT and (b) 250 °C. Si content of the core alloy as measured by ICP-OES is indicated by the dashed line.

3.4. Discussion
3.4.1. Total Liquid Duration Time Calculation

Fig. 3-6 indicated that the rate of melting peak area reduction (i.e. the rate of liquid clad removal) depends on strain and forming temperature for O temper sheet, but no relationship was clear for H24 sheet. To elucidate the effects of sheet temper, forming temperature, and applied strain, the peak area data were re-plotted against the square root of the cumulative LDT, a technique which has been shown to be effective for studying solid-liquid interactions in a number of material system [43, 78, 82, 83, 84, 85, 86]. The total LDT for complete liquid clad depletion, which was the parameter used to predict brazing performance in this chapter, was found by extrapolating the data to the x-axis. An example of this procedure is shown in Fig. 3-13 for two forming conditions; the difference in the rate of peak area reduction is clearly observed in the difference in the slopes for the two forming conditions.
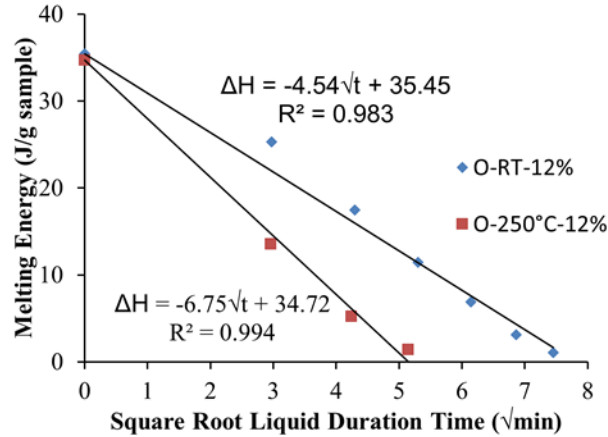
Fig. 3-13 Total LDT calculation method of re-plotting melting peak area data against the square root of the LDT and extrapolating to the x-axis.

The measured initial melting peak areas (i.e. data points at 0 min) are less than the value expected for the clad layer thickness and melting enthalpy of a eutectic Al-Si alloy. Solid state diffusion of Si out of the clad layer during heating to the brazing temperature suppresses the formation of liquid clad through the formation of the depleted zone [50]. However, losses due to solid state diffusion were previously shown to be insufficient to fully explain the difference between the measured and theoretical melting enthalpies [52]. The development the non-melting clad residue layer during diffusion controlled melting of the clad, as described by Zhao and Sekulic [45], could explain part of the remaining discrepancy. Kuntz *et al*. [78] also noted a discrepancy between measured and theoretical enthalpy values at 0 min hold times when studying isothermal solidification using DSC, and proposed a number of correction factors to adjust their data. These corrections were based on ratios of melting and solidification peak areas, measured during various heating and cooling segments in the test temperature profile. One of the proposed correction factors was reported to account for primary solidification and epitaxial growth during isothermal holds, which is not detectable using DSC. The reduction in the initial melting energy in the current study occurs before an isothermal hold, so if primary solidification is to explain the reduced melting energy value, it would have to occur during melting. While primary solidification likely occurs during melting, due to enhanced Si diffusion with increasing temperatures, it is unlikely that this can explain the entire discrepancy in energy values, given the short duration over which the melting peak occurs.

When the data extrapolation procedure was performed for all experimental trials, the total LDT as a function of strain and forming temperature was obtained for both sheet tempers (Fig.

50

3-14). From Fig. 3-14a, the relationship between total LDT and applied strain was not the same at both forming temperatures for O temper sheet. For RT forming, the LDT decreased with increasing levels of strain up to 4 %, indicating that liquid clad was being consumed more rapidly. As a result, the brazing performance of these forming conditions is predicted to be relatively poor. However, the LDT increased with increasing levels of strain above 4 %, which indicates that liquid clad is available for longer times at higher levels of strain, and thus improved brazing performance is expected at higher strains. The dependence of the O temper LDT on RT strain is in excellent agreement with previous studies, where the maximum extent of LFM occurred in sheets strained to between 2 % to 7.5 %, depending on how LFM was evaluated and the initial sheet conditions [12, 14, 57, 69, 70, 71].
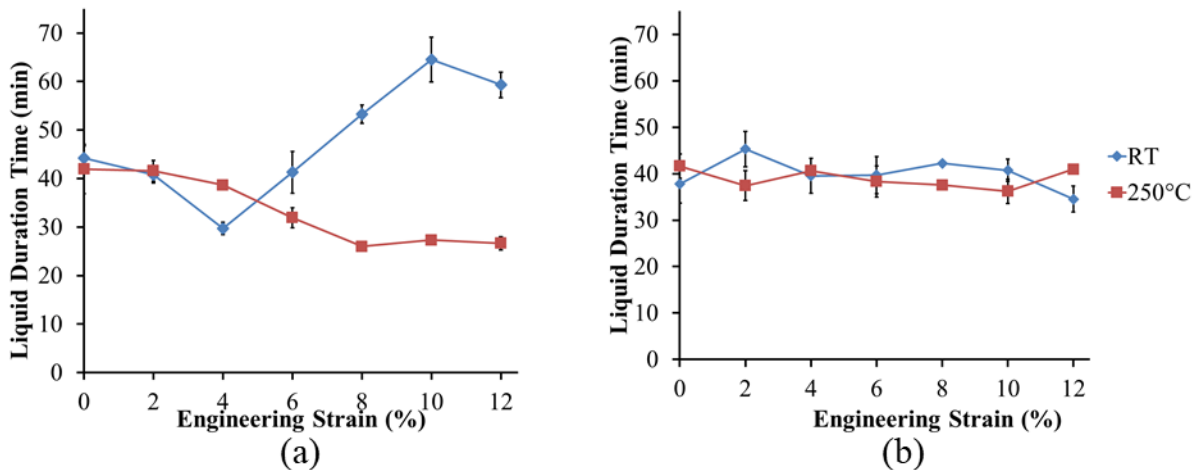
Fig. 3-14 Total LDT for complete liquid clad removal as a function of strain for both forming temperatures in (a) O and (b) H24 temper sheets.

The relationship between LDT and applied strain was different for warm formed O temper sheet. The LDT again initially decreased with increasing levels of strain, and reached a minimum LDT at a slightly higher strain (i.e. 8 %) than for RT stretching. Unlike for RT stretching, the LDT for warm formed samples did not increase at higher strains, but plateaued at the minimum value for the strains studied. Wittebrood *et al.* [71] showed that DSC data could accurately predict brazed joint fillet sizes; the comparatively low LDT at high strains indicates the possibility of undersized brazed joints in warm formed O temper sheet, due to relatively rapid

liquid clad loss by LFM during brazing. Therefore, the brazeability of warm formed O temper sheet is predicted to be inferior to RT strained sheet, particularly at high strains.

The LDT of H24 sheet as a function of strain and forming temperature can be seen in Fig. 3-14b. No clear dependence on applied strain was observed at either forming temperature, as was suggested in Fig. 3-6c and d. Again, any strain non-uniformity introduced by necking does not appear to have influenced the thermal data, because the H24 sheet temper is already highly deformed. More important was the lack of dependence of the LDT on the forming temperature observed in Fig. 3-14b. Insensitivity to forming temperature is ideal for warm forming of Al brazing sheet, as this suggests that springback of high hardness sheet can be reduced through warm forming without adversely affecting the LDT and, hence, brazeability.

3.4.2. Microstructural Evolution During Brazing

O Temper

As discussed in section 2.4.3 and shown schematically in Fig. 2-16, three possibilities exist for solid-liquid interactions during brazing of strained Al brazing sheet: (i) no detectable interaction, (ii) LFM, and (iii) recrystallization/SIBM [14]. At very low strains, insufficient stored energy is present in the core to provide a driving force for recrystallization or for liquid clad penetration, and no significant interaction is observed.

With further increases in strain, penetration of liquid clad occurs due to LFM. Yang and Woods [69] proposed that the driving force for LFM in Al brazing sheet is the reduction of stored deformation energy in the core, and that the severity of the attack increases with applied strain, up to the point that recrystallization occurs. More recently, Wittebrood [14] evaluated all of the possible driving forces proposed in literature, and also concluded that a reduction of deformation energy was the most viable explanation, where the LFM driving force is directly proportional to the dislocation density ahead of the liquid film (Eq. 8, pg. 29). According to McElroy and Szkopiak [25], the dislocation density in a strained material is proportional to the square of the material flow stress, as stated in Eq. 1 (pg. 10). A connection between forming and LFM can be made by combining Eq. 1 and Eq. 8. In doing so, it can be seen that the driving force for LFM increases with the square of the flow stress, all other variables being equal. From Fig. 3-14a, it was found that the O temper LDT depended on both the level of applied strain and forming temperature. The increased rate of liquid clad loss for O temper sheet strained up to 4 % at RT

was due to an increasing driving pressure for LFM, due to the work hardening of the sheet. On the other hand, the rate of LDT reduction in warm formed O temper sheet was more gradual than for RT forming, and did not reach a minimum value until a greater applied strain. It can be concluded from Fig. 3-3 that the more gradual reduction in LDT was due to the reduced flow stress at 250 °C, which led to a lower driving pressure for LFM, but also prevented the critical stored energy necessary to trigger SIBM from being reached. The lack of work hardening in warm formed O temper sheet resulted in a leveling off of the LFM driving force, and explains the LDT plateau at high strains. A distinct metallurgical characteristic of LFM in general is that the region through which the liquid film passes has a composition which is consistent with the equilibrium solidus composition at the brazing temperature [67]. The post-braze microstructures in Fig. 3-7a and Fig. 3-9, and the composition profiles in Fig. 3-8a and Fig. 3-10 displayed these characteristics.

As more deformation is applied to the sheet, a critical level of stored energy is reached, at which point the core alloy recrystallizes during brazing by SIBM, leading to a coarse recrystallized microstructure, and a reduction of the stored deformation energy [54]. Since SIBM and LFM are both driven by the reduction of stored deformation energy, the driving force for LFM is eliminated when SIBM occurs before the clad layer melts, and liquid clad penetration is minimized [14]. The coarse grain microstructure and lack of LFM attack on the core was observed in Fig. 3-7b and c for the O-RT forming condition. On the other hand, SIBM was not observed at any level of applied strain in the warm formed O temper sheet, leaving it susceptible to LFM (Fig. 3-9).

The post-braze microstructures are in agreement with the trend in LDT data in Fig. 3-14 for both forming temperatures. For RT forming, the LDT reached a minimum value at 4 %, where the core alloy was non-recrystallized and LFM occurred. When the strain was further increased to 6 %, the LDT began to increase, and the microstructure was characterized by a coarse, recrystallized core. On the other hand, the post-braze microstructure was characterized by a non-recrystallized core and LFM for the O-250 °C forming condition at all strains, and the LDT plateaued at a relatively low value for these conditions. The agreement between the thermal data and microstructure analysis demonstrate the suitability of using the LDT as a brazing performance indicator, and the utility of DSC for studying Al brazing sheet.

H24 Temper

The thermal data for the H24-RT forming condition (Fig. 3-14b) and the corresponding microstructures (Fig. 3-11) can be explained by the stress-strain data. The H24-RT flow stress was greater than that of the O temper sheet at all levels of applied strain and, thus, recrystallization was expected during brazing, as was observed (Fig. 3-11a and b). Furthermore, relatively little work hardening occurred during forming, so the LDT was expected to be independent of the level of applied strain, which was also shown in Fig. 3-14b. However, the stress-strain data do not explain the post-braze microstructures or LDT data for the H24-250 °C forming condition. The H24-250 °C stress in Fig. 3-3 was clearly below that of the H24-RT condition, and even below the stress corresponding to O-RT at 6 % strain, where SIBM was first observed (Fig. 3-7b). However, the LDT data were indistinguishable from the H24-RT data in magnitude, and were similarly independent of the level of applied strain.

Using hardness as a qualitative indication of the relative level of stored energy in the core alloy after forming [24, 87], the independence of the H24 temper LDT on strain and forming temperature can be explained. Cross sections of the strained Al brazing sheet prior to brazing were mounted, ground, and polished. Vickers microhardness measurements were performed on the core layer of these sheets, using a load of 25 gf and dwell time of 15 s, in order to qualitatively measure the relative stored energy in the core alloy for different forming conditions. Ten measurements were performed along the length of the mounted sample for each forming condition, and the average hardness and standard deviation for a number of forming conditions are presented in Fig. 3-15.
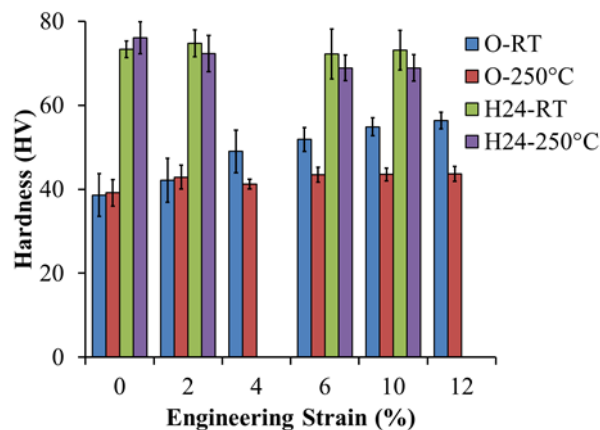
Fig. 3-15 Pre-braze core alloy hardness measurements of O and H24 temper sheet formed at RT and 250 °C.

The O temper hardness data mirrored the stress-strain curves in Fig. 3-3. Work hardening in RT strained samples was reflected by a continual increase in hardness with applied strain, while the lack of work hardening in warm formed samples resulted in plateauing of the hardness. Furthermore, the H24-RT hardness data reflected the stress-strain data, in that a lack of work hardening was observed, and that even in the as-received condition, the H24 hardness was significantly greater than the most highly strained O temper sheet. Using hardness as a qualitative indicator of stored deformation energy in the sheet, there was a high driving force for recrystallization to occur during brazing of H24 sheet, even in the as-received condition. As the sheet was further strained, the driving force for recrystallization did not significantly increase, and an independence of the LDT on applied strain was observed (Fig. 3-14b). A slightly greater variation in the hardness measurements can be seen for the H24-RT condition at 6 % and 10 % strain, which could be attributed to localized necking. However, the variation is not greater than what was observed for the O-RT condition at 0 % and 2 % strain, where the strain distribution is uniform. Therefore, any effect of localized necking does not appear to significantly impact the material hardness data. Previous studies noted that H temper sheet recrystallizes early in the brazing cycle, resulting in coarse core grains, which prevent extensive liquid clad penetration [12, 71]; the recrystallized microstructure and uniform residue layer were also observed in the current work (Fig. 3-11).

On the other hand, the warm formed H24 stress-strain data did not suggest why the LDT was independent of forming temperature. Clearly, the stress-strain curve at 250 °C was lower than the RT curve; however, when the sheets were cooled to RT, the core hardness remained comparable to the RT formed sheet, as seen in Fig. 3-15. The negative slope in the stress-strain curve for the H24-250°C condition in Fig. 3-3 is attributable to the formation of a diffuse neck during forming. However, a slight decrease in the average hardness value with increasing strain also suggests that some dynamic recovery could have occurred during forming, due to the relatively long time at 250 °C because of the low strain rate used in the experiments. Regardless, the core hardness of the warm formed H24 sheet remained significantly higher than the cold worked O temper sheet and, thus, recrystallized during simulated brazing (Fig. 3-11c), which prevented extensive liquid clad penetration and led to an independence of the LDT on forming temperature.

3.5. Summary

Warm forming was shown in prior studies to be a promising technique to improve formability and reduce springback of multi-layered Al brazing sheet. However, no investigations into the effect of an increase in forming temperature on brazing performance had been conducted, prior to the current project. This chapter was the first to investigate this relationship, and provided an understanding of some of the implications of warm forming on brazing performance. The experimental work led to the following conclusions:

1. The liquid duration time (LDT) is a suitable parameter for predicting brazing performance. The LDT data for the O-RT forming condition were well correlated with the post-braze microstructure, and displayed the same non-linear dependence between the severity of liquid film migration (LFM) and applied strain that had been observed in past studies. Forming conditions with poor predicted brazing performance (i.e. low LDT values) were found to have a post-braze microstructure characterized by a non-recrystallized core, and grains characteristic of LFM at the sheet surface. Conversely, a thin residual clad layer and recrystallized core were observed in conditions with a comparatively large LDT.

2. O temper sheet formed at 250 °C is predicted to have inferior brazing performance relative to O temper formed at room temperature, based on the LDT data. The LDT for the former plateaued at the minimum value, and did not increase over the range of strains studied. Microstructure analysis revealed that forming at 250 °C extended the range of strains over which LFM occurred, and delayed the onset of recrystallization to a level of strain greater than what was studied in this chapter.

3. The brazing performance of H24 temper sheet is predicted to be independent of both applied strain and forming temperature, up to 250 °C, as there was no clear difference in the LDT data with changes in strain or forming temperature.

4. The results provided indirect support for the strain induced LFM driving force. The reduction in flow stress and work hardening during forming at 250°C, resulted in a

continually increasing driving force for LFM in the O temper sheet, without reaching the critical level required to initiate recrystallization during brazing. The increased susceptibility to LFM was manifest in the distinct change in the relationship between the LDT and applied strain when the forming temperature was increased; the liquid clad was rapidly depleted over a range of strains in the warm formed sheet, without subsequent improvement at higher strains.

4. Effect of Forming Temperature on Sagging Resistance of O Temper Al Brazing Sheet[2]

4.1. Introduction

Earlier results outlined in Chapter 3 predicted that the brazing performance of O temper sheet formed at 250 °C will be impaired, due to increased kinetics of the interaction between the liquid clad and solid core during brazing, particularly at the highest strains studied. The greater interface kinetics were shown to be well correlated with an extension of the range of strains over which liquid film migration (LFM) occurred, which corresponded to the inability of the core alloy to recrystallize prior to reaching the brazing temperature. In contrast, the brazing performance of H24 sheet was predicted to be independent of both applied strain and forming temperature, up to 250 °C. The highly deformed core alloy of the H24 sheet was able to recrystallize prior to the onset of clad melting, and the driving force for LFM was consequently eliminated.

The objective of this chapter is to further elucidate the relationship between forming temperature and brazing characteristics of O temper sheet, to determine if there is a forming temperature which will provide enhanced formability without degrading brazing performance, relative to room temperature (RT) forming. Warm forming was again simulated by interrupted tensile tests at different forming temperatures, and brazing performance was predicted by the commonly used sagging test. The sagging test results were supported by microstructure and composition analysis.

4.2. Experimental Procedure
4.2.1. Sample Preparation

O temper Al brazing sheet tensile test specimens were prepared using the same dimensions as described in section 3.2.1. Warm forming was simulated by performing interrupted tensile tests up to pre-determined levels of strain between 2 % and 12 % engineering

strain, where the reported strains are the average value between two extensometer markers spaced approximately 12.7 mm apart. The samples were stretched using a cross head speed of 0.75 mm/min, which resulted in an average engineering strain rate of 6.6×10^{-4} s^{-1} for a nominal gauge length of 19 mm. Tensile tests were performed at RT, 150 °C, 200 °C, and 250 °C, using the same test equipment described in section 3.2.1.

4.2.2. Sagging Test

The sagging test is a common technique used to predict the brazing performance of Al brazing sheets. After clamping one end of a sample in a fixture and exposing the fixture to a simulated brazing temperature cycle, the deflection of the sample's free end is measured. As noted by Zhao and Woods [1], a strong resistance to sagging is desirable, as a large sagging distance indicates that the sheet will lose its rigidity during brazing, and the assembly may collapse under its own weight. In this chapter, sagging test samples were prepared by shearing off one grip-end of the strained tensile specimens. The opposite end of the specimen was clamped in the sagging test fixture such that 23 mm of the strained specimen was cantilevered over the test fixture. A schematic diagram of the test set-up can be seen in Fig. 4-1.
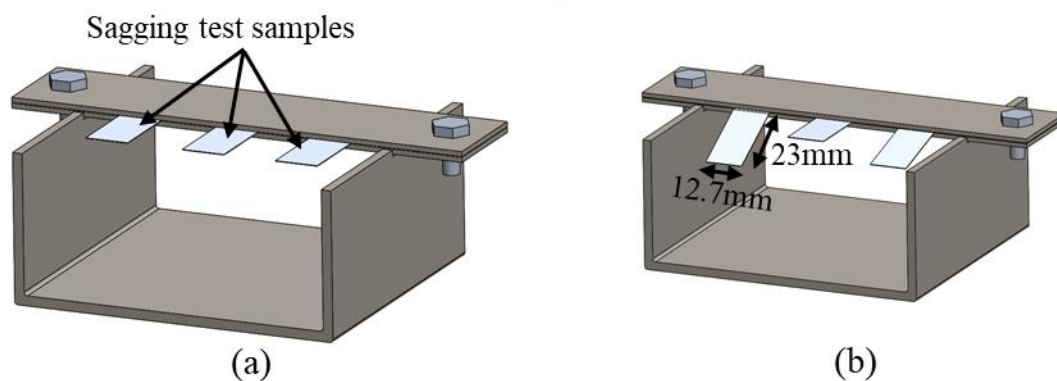
Fig. 4-1 Schematic representation of the sagging test fixture and samples (a) before and (b) after a simulated brazing cycle.

A Thermo Scientific Lindberg/Blue M Moldatherm box furnace was used to simulate an industrial brazing cycle for the sagging test. Prior to heating, the furnace was backfilled with high purity (99.999 %) nitrogen gas, which continued to be flowed through the furnace

throughout the test. The nitrogen gas flow was adjusted during furnace calibration such that the oxygen content in the furnace, measured using a Honeywell GMS-10 RVS sensor, was maintained below 2 % throughout the sagging test. Before the tests were conducted, the furnace temperature profile was calibrated using as-received brazing sheet samples. The samples were instrumented with thermocouples attached to the core side of the sheet using thermal paste, at both the free and clamped ends of the sample. The calibration set-up can be seen in Fig. 4-2. The furnace controller was set to 598 °C for the simulated brazing heat treatment; from the calibration data, the average maximum temperature at the free end of the samples was 601 °C, while the average temperature at the clamped end was slightly higher (605 °C) due to its proximity to the thermal mass of the test fixture. The nitrogen gas flow was stopped after complete solidification of the clad alloy during cooling around 550 °C, and the furnace door was opened when the sample temperature reached 525 °C to rapidly cool the samples. The average heating rate from RT to the peak temperature was approximately 15 °C/min, while the cooling rate to the point where the furnace door was opened was approximately 10 °C/min. The measured sample temperature profile over the entire test is given in Fig. 4-3a, and a magnified view of the sample temperature over the range where the clad alloy is liquid is given in Fig. 4-3b.
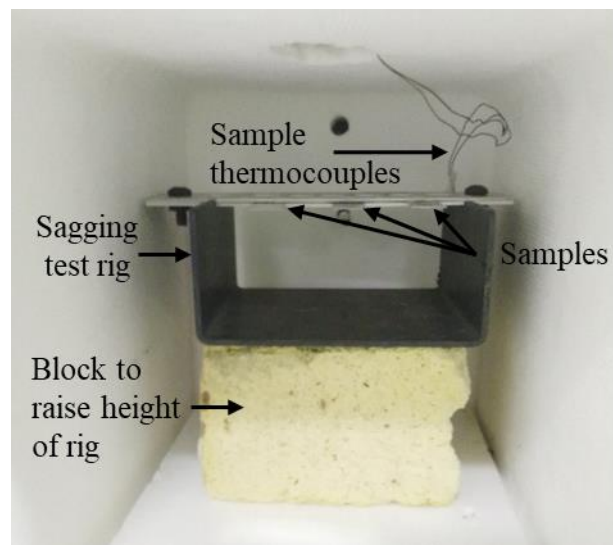
Fig. 4-2 Sagging test rig inside the furnace during temperature calibration.
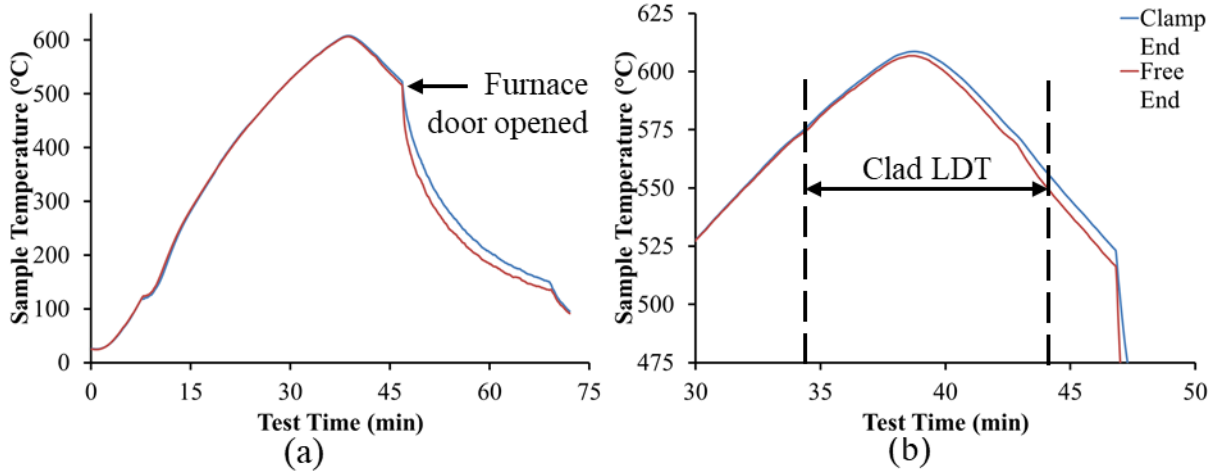
Fig. 4-3 Measured temperature profile at both ends of the brazing sheet sample over (a) the entire test duration and (b) the segment of the heating profile when liquid clad is present. The estimated liquid duration time (LDT) for the free end of the sample is indicated.

As previously noted, it is of interest to understand how a change in forming temperature could affect interactions between the liquid clad and solid core during brazing, such as LFM. Thus, it was important to estimate the clad liquid duration time (LDT), which is the time between the onset of clad melting and the end of clad solidification (Fig. 4-3b), as this is the time over which LFM can occur. The LDT at the clamped and free ends of the samples at each of the three specimen locations on the sagging test fixture was estimated using the calibration data (Fig. 4-4), using the elapsed time between the same clad melting onset and solidification end temperatures as measured in section 3.3.2. The average LDT was longer at the clamped end of the sample due to the proximity to the test fixture. The average LDT was similar across the three fixture locations (within 1 standard deviation), for both the clamped and free ends of the samples.

61
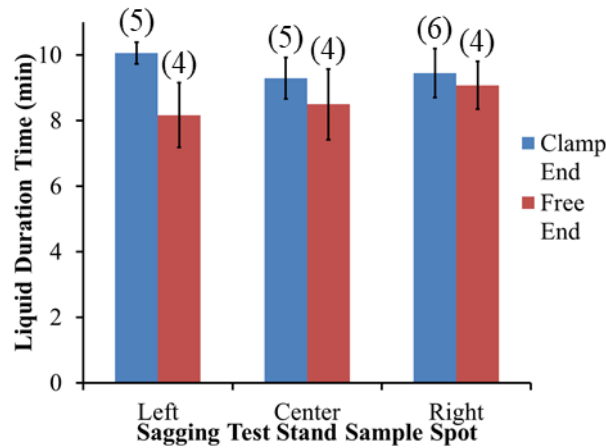
Fig. 4-4 LDT at the clamped and free ends of the sample at each fixture location estimated from thermocouple data during calibration. The number of measurements used to determine the LDT are indicated above each estimate.

After removing the test fixture from the furnace, the deflection of the free end of the samples was measured. In order to reduce the effect of lurking variables, two replicates were performed for each forming temperature-strain combination, where the second replicate was tested in a different clamp location than the first replicate, and the test order was completely randomized.

4.2.3. Microstructure and Composition Analysis

After the sagging test, the strained gauge lengths of the samples were mounted and prepared for microscopy by standard metallographic grinding and polishing. The sheet microstructure was revealed by etching the cross sections with Keller's reagent. A Philips XL30 scanning electron microscope (SEM) equipped with energy dispersive x-ray spectroscopy (EDS) was used to estimate the local chemical composition across the clad-core interface after the sagging test, using an accelerating voltage of 15 kV.

To investigate the driving force for LFM, transmission electron microscopy (TEM) analysis was conducted across the clad-core interface before and after simulated brazing for a number of forming conditions. The brazing cycle was simulated by punching 4.8 mm (3/16") discs from between extensometer markers on the gauge length of newly prepared strained samples, placing the discs within the differential scanning calorimeter furnace to simulate a controlled atmosphere furnace, and holding at 600 °C for 10 min. All heating and cooling was

performed at 20 °C/min below 500 °C and 10 °C/min above 500 °C (section 3.2.2). The samples were mounted along the direction of applied strain, ground, and polished. An FEI Helios NanoLab 650 focussed ion beam (FIB) microscope was used to prepare wedge lift out samples taken across the clad-core interface. TEM analysis was performed at CanmetMATERIALS in Hamilton, ON, using an FEI Tecnai Osiris microscope, using an accelerating voltage of 200 kV. Imaging was performed using bright field scanning TEM (BF-STEM) mode, where the electron beams were focussed to a probe and scanned in a raster pattern across the imaging area.

4.3. Results
4.3.1. Warm Forming

The brazing sheet stress-strain curves, up to the maximum strain studied, are given in Fig. 4-5 for all forming temperatures investigated. Thermal softening of the material and reduced work hardening were observed as the forming temperature increased. As noted in section 3.3.1, diffuse necking likely occurred during deformation of O temper sheet at 250 °C above 8 % strain, as a slight decrease in the stress-strain curve was observed; however, as noted previously, the strain gradient along the length of a diffuse neck is gradual, and the deformation can be considered practically uniform. Close inspection of the data in Fig. 4-5 did not reveal a decrease in the stress-stress curves for deformation at either 150 °C or 200 °C, so the deformation through the gauge length at these temperatures is uniform.
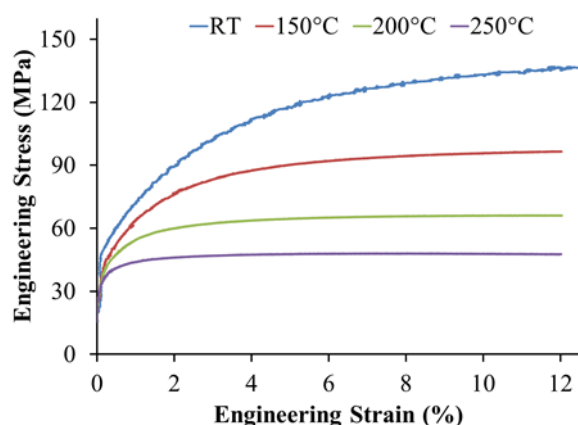
Fig. 4-5 Experimental stress-strain curves for O temper Al brazing sheet at a number of forming temperatures.

4.3.2. Sagging Test

The measured sagging distances after exposure to the simulated brazing treatment are plotted as a function of strain in Fig. 4-6. For all forming temperatures, the sagging distance initially increased with applied strain, but once a threshold level of strain was reached, the sagging distances decreased with the further application of strain. The decrease was most rapid for RT strained samples, followed by samples strained at 150 °C; at the highest levels of strain studied, the sagging distance of samples formed at RT and 150 °C were similar. The sagging distance for samples strained at 200 °C and 250 °C were large compared to those of samples formed at RT and 150 °C, particularly at the highest levels of strain. The data in Fig. 4-6 are the average of two measurements for each forming condition, plotted with error bars representing the standard deviation of the measurements. Overall, the experimental repeatability was excellent, where differences between sagging distance measurements for a given forming condition were at maximum 2 mm. The only exceptions were the RT-4 % and 150 °C-4 % forming conditions, where the differences in sagging distance measurements between the two replicates were 5 mm and 7.5 mm, respectively. The discrepancy in these measurements was suspected to be due to the fact that these forming conditions correspond to the peak sagging distance for their respective forming temperatures, separating regions where the sagging distance increased with applied strain from where sagging distance decreased with applied strain, and will be discussed in a subsequent section.
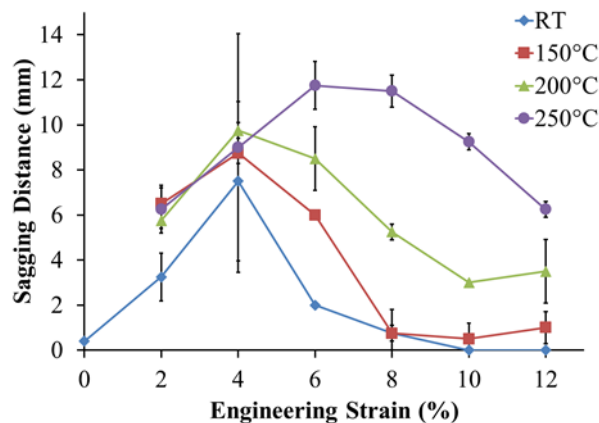
Fig. 4-6 Measured sagging distance of O temper Al brazing sheet as a function of strain for a number of forming temperatures.

4.3.3. Microstructure and Composition Analysis

Sheet microstructures after exposure to the sagging test (i.e. simulated brazing treatment) are shown in Fig. 4-7 to Fig. 4-9. It can be seen from the micrographs that, liquid clad alloy attack on the core occurred during the sagging test for forming conditions where the sagging distance was large, leaving large precipitate free grains at the sheet surface. Furthermore, the corresponding core alloy microstructures were characterized by small grains aligned along the direction of applied strain. Conversely, the microstructures of forming conditions corresponding to low sagging distances (i.e. >4 % at RT and >6 % at 150 °C) were characterized by coarse recrystallized core grains, with grain sizes approaching the sheet thickness, and minimal, if any, instances of liquid clad alloy attack on the core alloy.
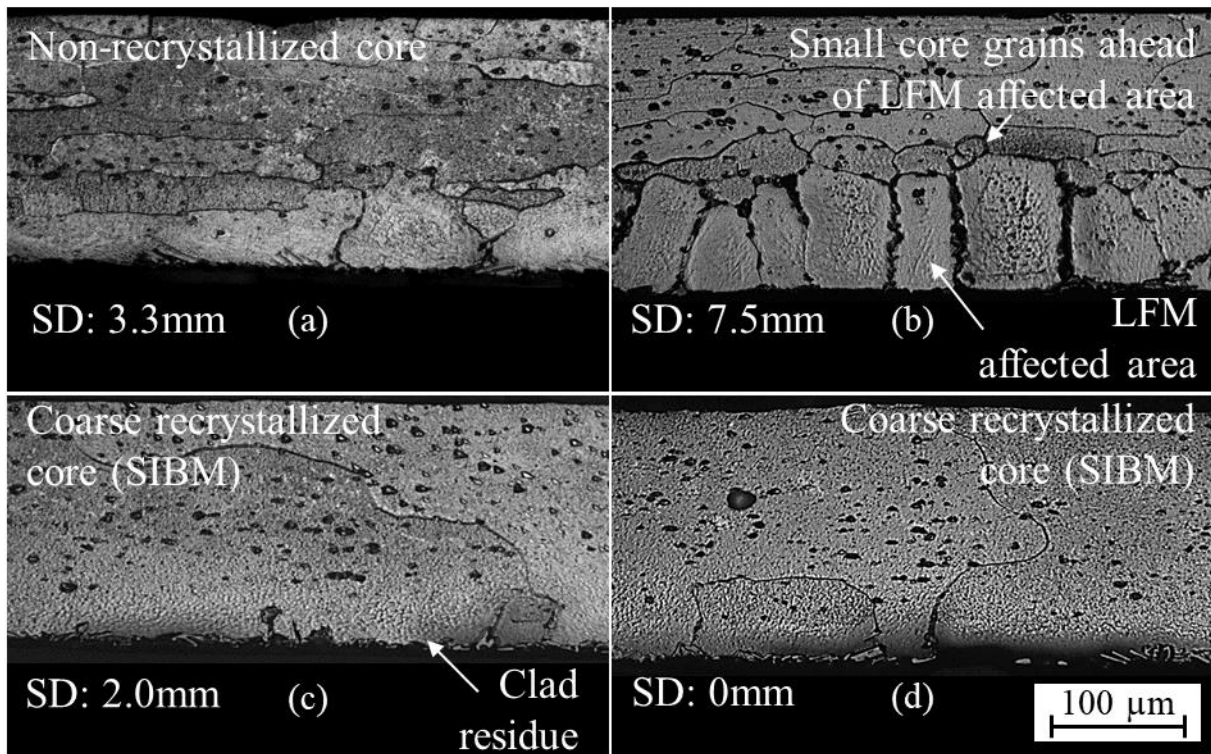
Fig. 4-7 Post-sagging test microstructures for sheets strained at RT to (a) 2 %, (b) 4 %, (c) 6 %, and (d) 10 % engineering strain. Note that the sagging distance (SD) is the average of the two specimens.
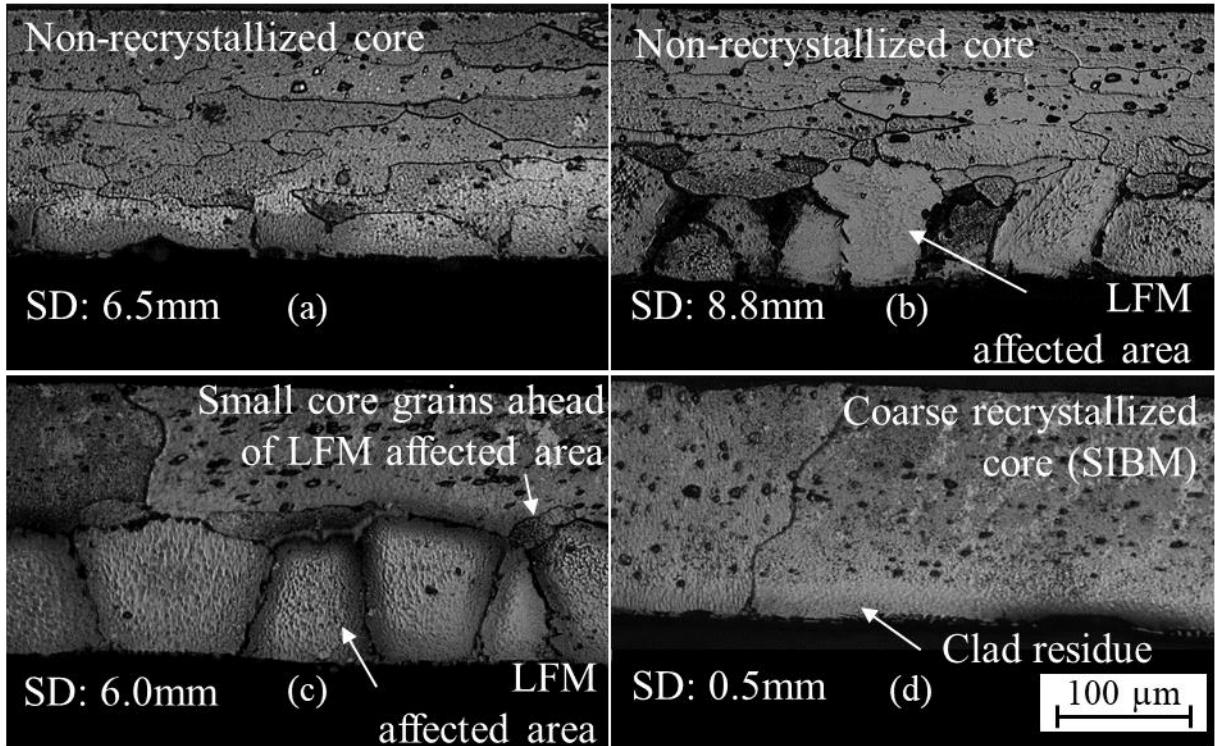
Fig. 4-8 Post-sagging test microstructures for sheets strained at 150 °C to (a) 2 %, (b) 4 %, (c) 6 %, and (d) 10 % engineering strain. Note that the sagging distance (SD) is the average of the two specimens.
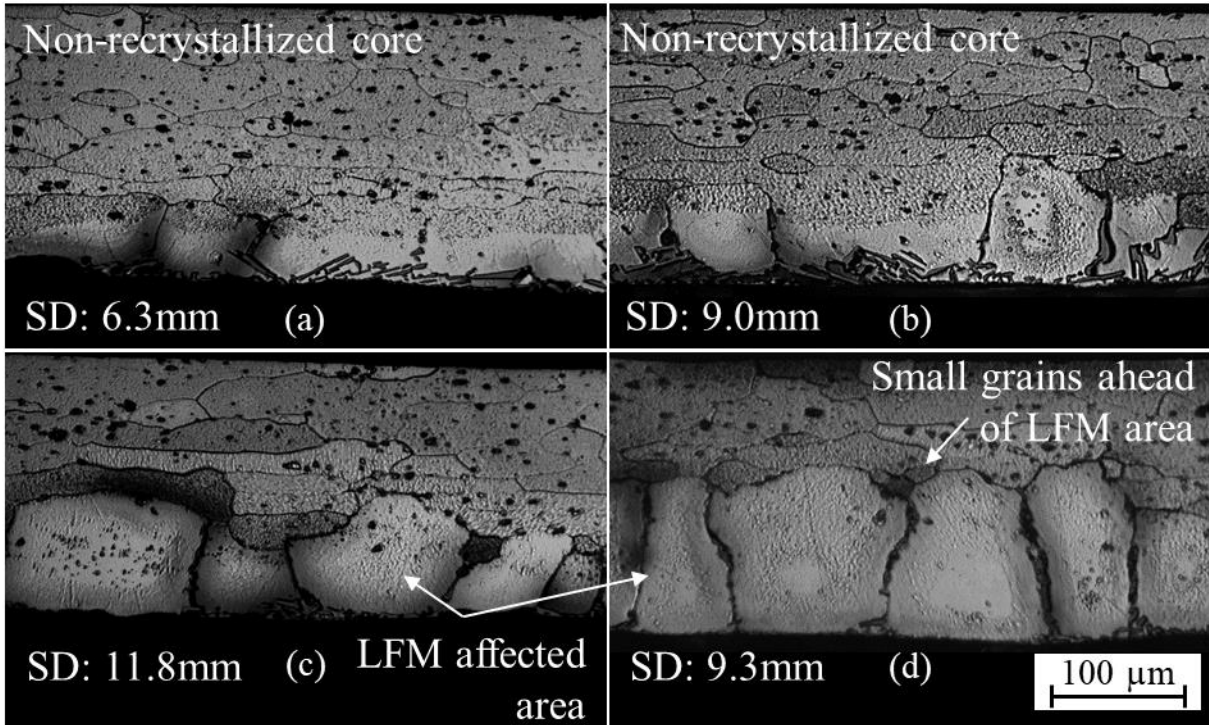
Fig. 4-9 Post-sagging test microstructures for sheets strained at 250 °C to (a) 2 %, (b) 4 %, (c) 6 %, and (d) 10 % engineering strain. Note that the sagging distance (SD) is the average of the two specimens.

EDS composition measurements through the sheet thickness after the sagging test for two forming conditions where severe liquid clad attack was observed are given in Fig. 4-10. The data have been overlaid on SEM images of the microstructure from which they were obtained, and all measurements were taken along a line corresponding with the abscissa in each plot. Measurements were performed on the Al matrix, avoiding scanning directly on second phase particles or the eutectic phase. It was found that the large surface grains, which were correlated with large sagging distances, had a Si content around the solidus composition at 600 °C and a diffusion profile ahead of these grains into the remaining core, which are consistent with LFM.
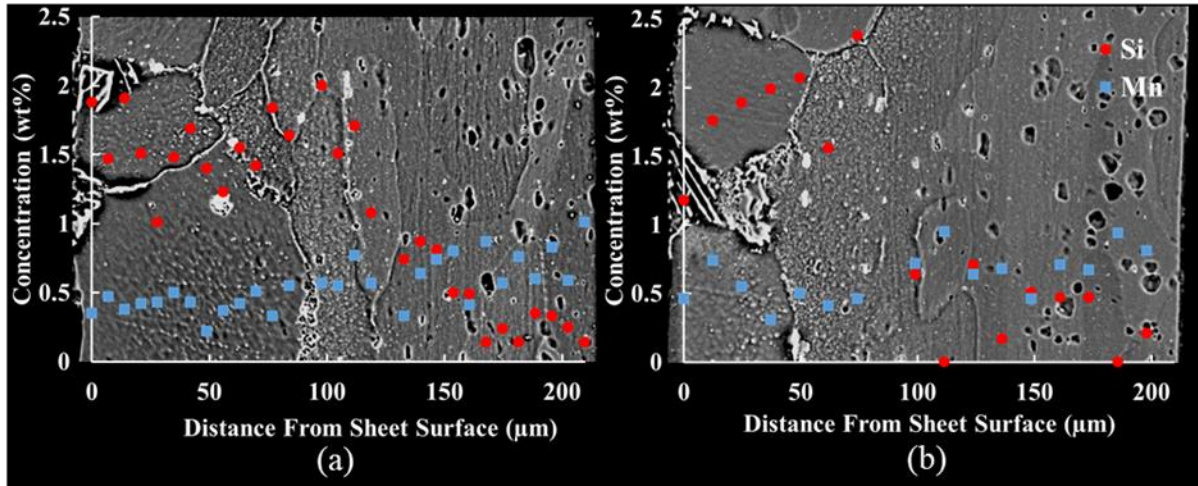
Fig. 4-10 Composition measurements of Si (red) and Mn (blue) through the sheet thickness after the sagging test for (a) RT-4 % and (b) 250 °C-10 % forming conditions. Measurements were taken along a line coinciding with the abscissa in both plots. The clad alloy is on the left side of each micrograph.

The BF-STEM images from the clad-core interface before and after a simulated brazing heat treatment are given in Fig. 4-11 for a number of forming conditions. In all images, the core alloy is toward the top of the image. Dislocations cells were observed in all forming conditions prior to the brazing heat treatment, due to the applied strain (Fig. 4-11a-c). After the brazing heat treatment, the dislocation density in the RT-10 % forming condition was significantly reduced (Fig. 4-11e), indicating that the coarse core grain structure observed in Fig. 4-7d was, in fact, a recrystallized microstructure. The presence of sub-grains in the core for the RT-4 % and 250 °C-10 % forming conditions (Fig. 4-11d and f) indicate that the core alloys did not recrystallize in conditions where LFM occurred during brazing.
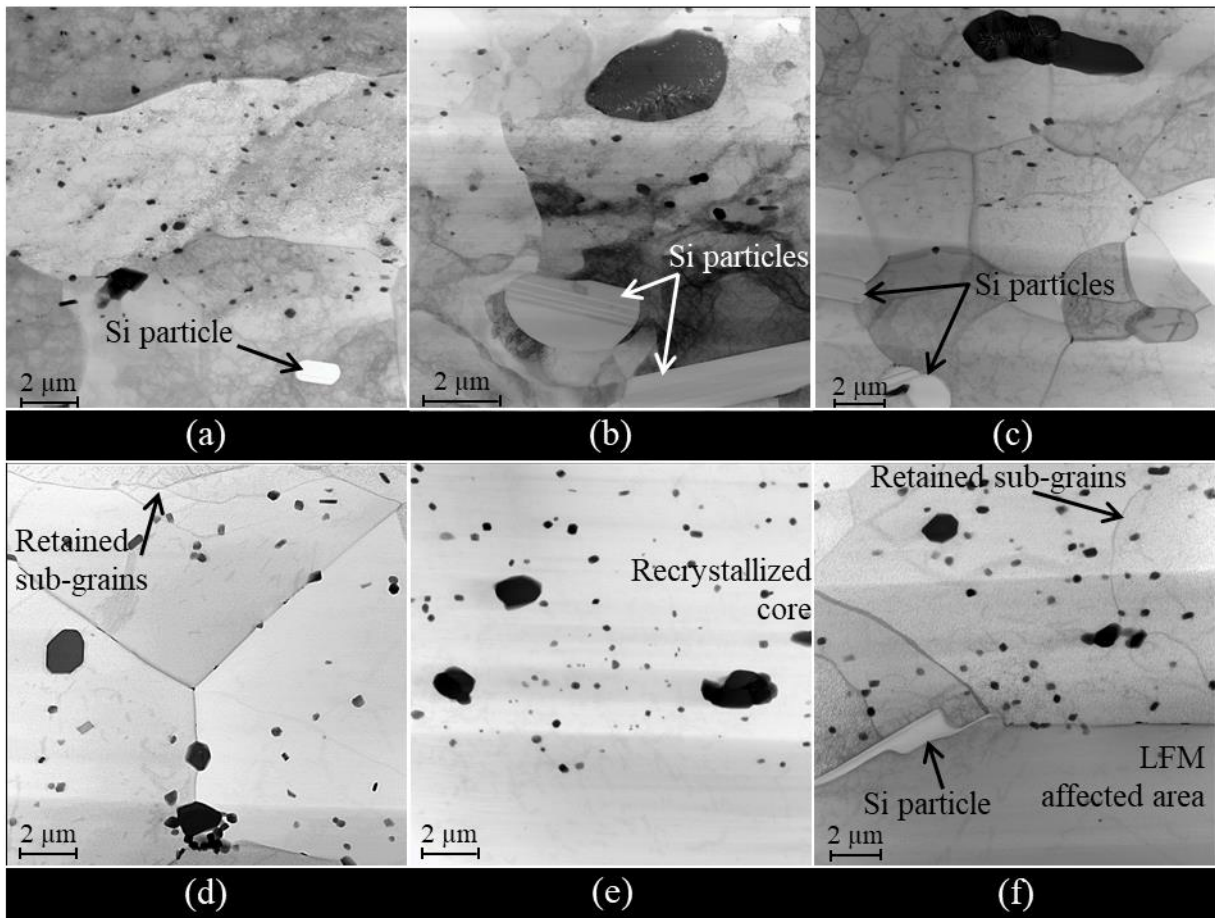
Fig. 4-11 BF-STEM images at the clad-core interface (a-c) before and (d-f) after a simulated brazing cycle for (a, d) RT-4 %, (b, e) RT-10 %, and (c, f) 250 °C-10 % forming conditions.

4.4. Discussion

A non-linear relationship between various parameters used to quantify LFM and applied strain has been documented in a number of other studies. For example, Yang and Woods [69] reported an increase in the depth of LFM attack with increasing strain up to 7.5 %, but a subsequent decrease in LFM depth at larger strains. Similarly, Wittebrood *et al.* [70] showed the same trend in LFM depth as a function of strain, where the maximum depth of attack occurred at 3 % strain, and the inverse relationship for braze joint fillet area; the smallest fillet area occurred at 3 % strain. The trend in the sagging distance as a function of RT applied strain in Fig. 4-6 was in excellent agreement with these prior studies, which indicated that the sagging distance can be considered a suitable parameter to predict the brazing performance of warm formed Al brazing sheets. Past studies have also noted that a coarse, recrystallized post-brazed core microstructure is necessary to prevent liquid clad attack during brazing. Tu *et al.* [62]

demonstrated the benefits of a coarse recrystallized microstructure by showing a drastic reduction in sagging distance when sheet processing parameters were adjusted to result in a recrystallized post-braze core alloy, but a subsequent increase in sagging distance when the processing parameters were further adjusted to produce a smaller recrystallized grain size. The benefit of a coarse recrystallized core alloy microstructure for brazing performance was observed in Fig. 4-7c and d and Fig. 4-8d. In these micrographs, the core alloy grains are characteristic of recrystallization by strain induced boundary migration (SIBM), and negligible, if any, liquid clad attack was observed. Consequently, the sagging distance for these forming conditions was low.

The microstructures presented in this chapter revealed that LFM occurred during simulated brazing for forming conditions with large sagging distances. According to Yoon and Huppmann [67], dissolution of the base metal occurs directly ahead of the liquid film, and is re-precipitated as a solid solution behind the film as the film migrates. Furthermore, the re-precipitated region should be in equilibrium with the solidus composition at the brazing temperature [68]. The precipitation of this Al-Si solid solution depletes the liquid film of its Si content, which is replenished by transport along the LFM grain boundaries, reducing the amount of liquid clad available for brazing. The composition data in Fig. 4-10 indicated that the LFM grains had a Si concentration close to solidus composition at the peak brazing temperature of 600 °C and a Si diffusion profile ahead of the film, as were also noted by Wittebrood [14].

As the sagging distance had a non-linear relationship with applied strain, and large sagging distances were correlated with the occurrence of LFM, the occurrence of LFM should be related to the level of strain applied prior to brazing. Recently, Wittebrood [14] suggested that LFM in strained Al brazing sheet is a special case of the more general phenomenon, which he denoted as strain induced LFM (SILFM), where the liquid clad film progresses into the core to reduce stored deformation energy. As the film progresses through the core, the dislocation density (i.e. stored deformation energy) is reduced, since the liquid film cannot support the dislocations. The driving pressure for SILFM was given in Eq. 8 (pg. 29), and is directly proportional to the dislocation density ahead of the liquid film; thus, both SIBM and LFM are driven by the reduction of stored deformation energy. When SIBM occurs before the onset of clad alloy melting during the brazing cycle, the driving pressure for LFM is reduced and liquid clad attack is minimized. The BF-STEM images in Fig. 4-11 provided compelling evidence for the strain induced driving force for LFM and the competition between SIBM and LFM during

70

brazing. When the dislocation density in the core is sufficiently high prior to brazing, the core recrystallizes early in the brazing cycle, eliminating core dislocations and preventing LFM (Fig. 4-11e). On the other hand, when the dislocation density is not sufficiently high to initiate SIBM, the retained dislocations provide the driving pressure for LFM, as indicated by the sub-grains observed directly ahead of the liquid clad front in Fig. 4-11d and f.

The interplay between SIBM and LFM, and the consequent effect on sagging distance, was demonstrated by further investigation of the RT-4 % and 150 °C-4 % forming conditions. As noted previously, these were the only forming conditions with a large discrepancy in sagging distance measurements, and were also the maximum sagging distance measurements in their respective curves. The sagging distances corresponding to the microstructures in Fig. 4-7b and Fig. 4-8b were 10 mm and 12.5 mm, respectively. In both cases, a non-recrystallized core and LFM were observed. The sagging distance of the second replicate for both of these forming conditions was 5 mm, and the corresponding microstructures are given in Fig. 4-12. In both cases, LFM occurred during the sagging test, with some small non-recrystallized grains ahead of the affected area, which lead to the relatively high sagging distance (i.e. 5 mm). The LFM grains appear to have a textured surface in the figure, which could be due to non-uniform composition through the grain thickness, as seen in Fig. 4-10, but also due to the relatively long etching time of 110 s required to reveal core alloy grain boundaries. Beyond the LFM affected area, however, the core alloy consisted of coarse recrystallized grains, which prevented further progression of LFM. As the sheets are polycrystalline, some grains would be favourably oriented with the direction of applied strain. Near the critical level of applied strain, these grains would have sufficient stored energy to initiate SIBM, but LFM could still occur locally in other regions of the sheet where the stored energy is below the critical level. Such localized LFM has also been noted elsewhere [14]. A similar mix of non-recrystallized grains near the LFM affected area and coarse recrystallized grains further in the core was observed by Nylen *et al* [65]. The authors proposed that Si diffusion during brazing induced the precipitation of fine α-AlMnSi particles near the clad alloy (similar to the formation of the band of dense precipitates described in 2.5), stabilizing the deformed microstructure. The core alloy further away from the clad-core interface would not be affected by Si diffusion, and recrystallization during brazing was possible. It is believed that the balance between SIBM and LFM for the same forming condition lead to the variability in sagging distance observed in the RT-4 % and 150 °C-4 % conditions.

71
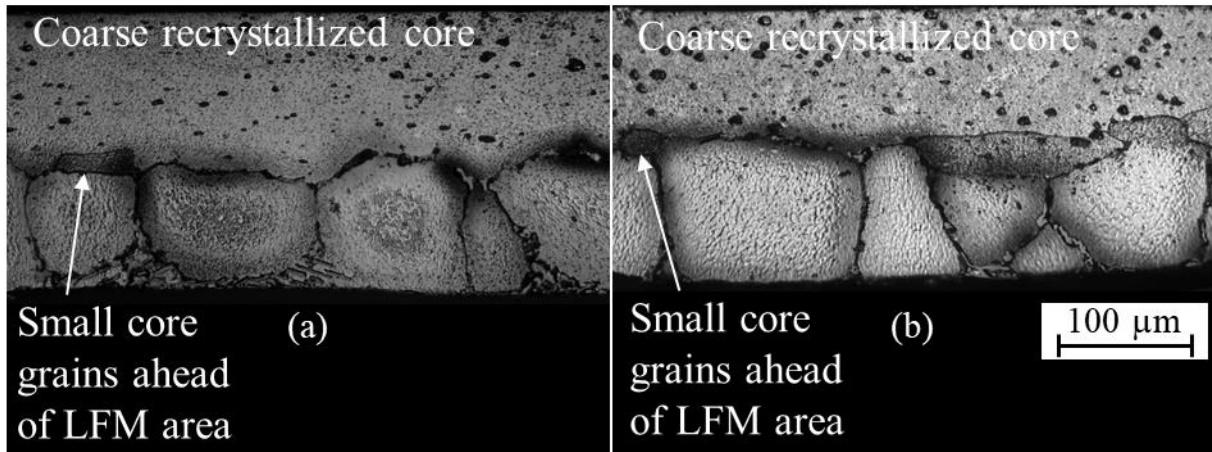
Fig. 4-12 Post-sagging test microstructures for the second replicate of the (a) RT-4 % and (b) 150 °C-4 % forming conditions.

To relate the sagging distance and microstructure results to warm forming, the dislocation density in the sheet prior to brazing can be approximated by Eq. 1 (pg. 10). By combining Eq. 1 and Eq. 8, the driving pressure for LFM is proportional to the square of the material flow stress. Thus, from Fig. 4-5, the driving pressure for LFM should change with changes in forming temperature. In theory then, above a critical stress (e.g. the stress corresponding to RT-6 %), SIBM occurs within the sheet but, up to this critical value, the driving pressure for LFM would rise with the square of the stress. During warm forming, the material flow stress and level of work hardening were reduced from their RT levels. Thus, the driving force for LFM increases more gradually during warm forming, but it becomes increasingly difficult to reach the critical stress to necessary for SIBM, and the regime of strains over which LFM can occur is extended. Coupling the LFM driving pressure of Eq. 8 to the material flow stress is, however, only a convenient approximation to relate the metallurgical phenomenon to warm forming, and is not without some discrepancy. For example, the RT-4 % microstructure (Fig. 4-7b) was non-recrystallized, while a coarsened grain structure was observed for 150 °C-6 % (Fig. 4-8c), despite a lower stress in the latter case. One explanation for the discrepancy is that the proposed LFM driving pressure is related to the dislocation density, even though it would be more accurately related to the energy associated with a sub-grain structure (Fig. 4-11d and f). The sub-grains may nucleate and grow as a result of dynamic recovery during warm forming or during the brazing cycle, but a complete discussion of recovery kinetics is beyond the scope of the current work. Another possible explanation for the discrepancy is that the driving pressure in Eq. 8 is related

to the dislocation density ahead of the film (i.e. in the core), while the stress-strain curves in Fig. 4-5 were for the multi-layered brazing sheet. However, bare core alloy with the same processing history as the multi-layered brazing sheet was not available for study.

4.5. Summary

In this chapter, the brazing performance of O temper Al brazing sheet strained at a number of forming temperatures was predicted using the sheet sagging distance after a simulated brazing thermal treatment. Sagging distance measurements were correlated with microstructure changes during simulated brazing. The experimental results lead to the following key findings:

1. The sheet sagging distance is an appropriate measurement to predict the brazing performance of warm formed Al brazing sheets. The sagging distance as a function of strain for RT formed sheet was in excellent agreement with prior studies, including the LDT measurements from Chapter 3. Further, the sagging distance measurements for all forming temperatures were consistent with the microstructures after a simulated brazing heat treatment.

2. Large sagging distances after simulated brazing were shown to be linked to the occurrence of LFM and a recovered core alloy. The BF-STEM images revealed the presence of sub-structures directly ahead of the re-solidified clad region, providing direct evidence for the proposed strain induced nature of the LFM driving force. Conversely, core alloys recrystallized by SIBM were observed in forming conditions with small sagging distances. SIBM during the brazing cycle reduces the stored energy in the core, eliminating the driving force for LFM. The change in the sagging distance as a function of strain with changes in the forming temperature, and consequently changes in stored deformation energy, provides indirect support for the strain induced LFM driving force.

3. Some improvement in sheet formability may be achieved without altering brazing performance by forming at 150 °C. The sagging distance as a function of strain was comparable for sheets formed at RT and 150 °C. The flow stress and work hardening were sufficiently high to accumulate the threshold level of stored energy to trigger SIBM

during brazing, preventing the onset of LFM above 6 % strain for both forming temperatures.

4. Warm forming of O temper Al brazing sheet at 200 °C and 250 °C is predicted to result in poor brazing performance due to the large sagging distances of sheets strained at these temperatures. The reduction in flow stress and work hardening observed during forming prevents the critical level of stored energy required to trigger recrystallization from being reached, resulting in a recovered core alloy, and consequently, the occurrence of LFM during brazing.

5. Microstructure Evolution During Brazing of Warm Formed Electric Vehicle Battery Cooling Plates[3]

5.1. Introduction

The preceding two chapters elucidated the effect that warm forming has on the post-braze microstructures and predicted brazing performance of strained O and H24 temper sheet. Warm forming was simulated by applying a uniaxial tensile load to Al brazing sheet samples at a number of forming temperatures. However, actual heat exchanger components often have complex geometries and loading throughout, such as combined tensile and bending stresses. Consequently, the strain will vary spatially throughout the formed component.

Given the dependence of the post-braze microstructure on applied strain and forming temperature observed in the prior chapters, the objective of this chapter was to understand the microstructure evolution at various locations in warm formed components with more realistic geometries. The analysis was performed on scaled-down electric vehicle battery cooling plates, which were formed at different temperatures and subjected to a typical industrial brazing temperature cycle. To facilitate the comparison of microstructures with those from uniaxial samples, a finite element model was used to predict strains throughout the plate.

5.2. Experimental Procedure
5.2.1. Materials and Sample Preparation

The microstructure evolution during brazing was assessed using a scaled-down commercial electric vehicle battery cooling plate design. The formed plate with major dimensions and annotated features can be seen in Fig. 5-1. In production, two identically formed plates are fixed together with their clad alloy layers in contact to form coolant channels, and passed through a furnace for brazing to form a leak-free battery cooling plate. However, in this chapter, only one-half of the full battery cooling plate assembly (i.e. individual formed plates) was used to assess the microstructure evolution during brazing.

---

[3] The contents of this chapter have been adapted with permission from: M. J. Benoit, K. B. Han, M. J. Worswick, M. A. Wells and S. Winkler, "Brazing characteristics of warm formed automotive heat exchanger components", originally published in the *16th International Conference of Aluminum Alloys Proceedings* (ICAA16), 2018. ISBN 978-1-926872-41-4
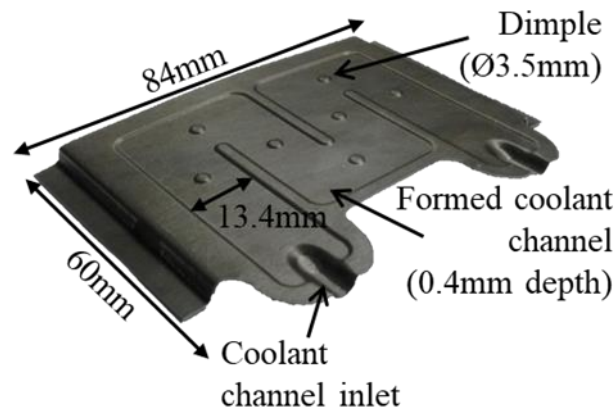
Fig. 5-1 One half of a simulated electric vehicle battery cooling plate assembly, with major formed features and dimensions indicated. The upper surface in this image is the clad alloy layer.

Battery cooling plates were formed from both O and H24 sheet tempers. Based on the results of Chapters 3 and 4, O temper sheets were formed at room temperature (RT), 150 °C, and 250 °C, while H24 sheet was formed only at RT and 250 °C. A custom tooling assembly, mounted on an Instron 1331 mechanical testing apparatus, was used to form the plates. The punch and die were equipped with cartridge heaters and embedded thermocouples, which provided feedback to a thermal controller for forming temperature control. The core side of the brazing sheet blanks were sprayed with MS-153BN boron nitride lubricant to avoid cracking of the components during forming [88]. Prior to forming, the punch and die were brought together such that the punch contacted the blank for 45 s to conductively heat the blank for plates formed at 150 °C and 250 °C [11]. After pre-heating, forming was performed using a punch speed of 1 mm/s, punch force of 80 kN, and a hold time in the fully closed position of 2 s. Further details regarding the forming process can be found elsewhere [89].

After forming, the plates were ultrasonically cleaned with acetone, followed by an industrial aqueous de-greasing procedure, to remove the lubricant and any surface contaminants from forming. The cleaned plates were then subjected to a simulated brazing cycle, using a nitrogen gas controlled atmosphere furnace, where the plates were heated to a peak temperature between 590 °C and 600 °C, held for 3 min, and were then cooled. This procedure was carried out using Dana Corporation's proprietary fluxless brazing process, whereby a nickel (Ni)-based braze promotor (instead of the commonly used potassium fluoroaluminate-based NOCOLOK® flux) was deposited on the clad alloy surface of the sheet prior to forming. Upon reaching the

76

ternary Al-Si-Ni eutectic temperature of 565 °C, an exothermic reaction occurs between the braze promoter and clad layer, which disrupts the oxide layer at the sheet surface and allows the liquid clad to flow [42, 43].

The battery plates were sectioned at a number of critical locations after brazing, as determined using the uniaxial test data from prior chapters and a finite element model of the formed battery plate. The cross-sections were mounted and prepared for metallographic analysis by grinding and polishing using progressively finer sandpaper and diamond particle size, respectively. The core alloy grain structure was revealed by etching with Keller's reagent.

5.2.2. Battery Plate Finite Element Model

A finite element (FE) model of the battery plate was developed by Han *et al.* [88, 89], and was used in this chapter to predict the strain and strain rate experienced throughout the plate, in order to correlate past uniaxial test data with the microstructures in the formed plate after simulated brazing. Forming simulations were performed using commercial LS-DYNA software [90], with a non-linear dynamic explicit formulation, in which the plate was modeled using quadrilateral shell elements 0.15 mm in size. The material model used the von Mises yield surface criterion and the extended Nadai phenomenological model to capture thermal softening and strain rate sensitivity during forming at elevated temperatures. The simulations used a punch speed of 1 mm/s to match experimental conditions.

5.3.   Results

Microstructure analysis was performed at two critical cross-sections in the battery plate. The first section was taken through the inlet to the coolant channel, at a distance of 4 mm from the front of the battery plate, and the second was taken through the four collinear formed dimples across the width of the battery plate. These sections are brazed joint faying surfaces in the full assembly but, unlike the flange areas surrounding the formed channels, these two sections experience a wide range of strains, which could lead to variable post-braze microstructures. Magnified images of the FE model predicted effective plastic strain (von Mises) contours at each of the two locations are given in Fig. 5-2a and b. For the channel inlet cross section, microstructure analysis was performed at: (i) the radius leading into the inlet where the strain is relatively large, and (ii) along the side of the inlet where the plastic strain is comparatively low.

The microstructure at the top of the formed dimples was also investigated, where the plastic strain was around 4 % for all forming conditions, which, from uniaxial tests in Chapters 3 and 4, was a level of strain predicted to have poor brazing performance for the fully annealed sheet at all forming temperatures. The FE membrane strain predictions from the mid-plane of the sheet along both cross-sections are given in Fig. 5-2c and d for the O temper sheet and all forming temperatures. Due to symmetry assumptions, the strain predictions in Fig. 5-2d are shown only up to the mid-plane of the plate. The trends in the strain predictions are similar for the H24 sheet, although the exact values differ slightly, due to differences in the material hardening behaviour and the earlier onset of diffuse necking in the H24 sheet during forming at high temperature [36].
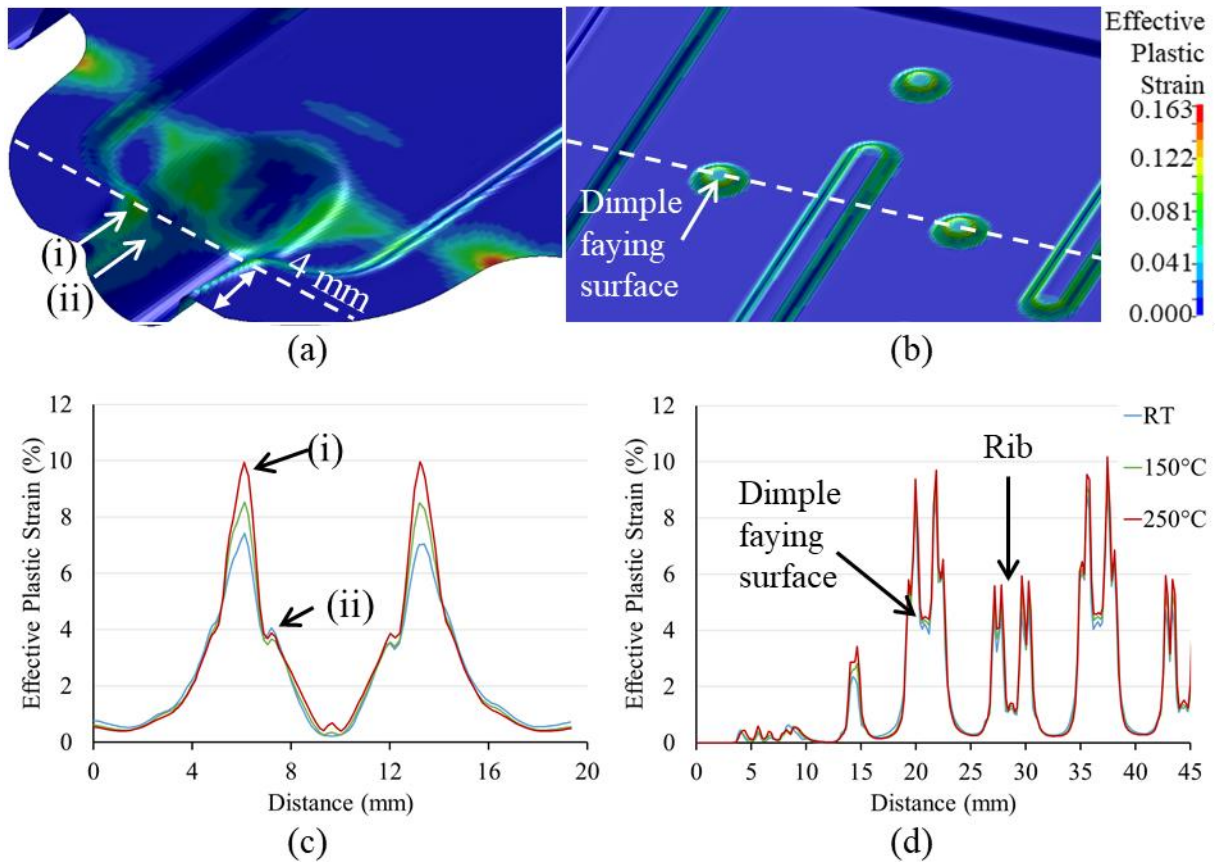
Fig. 5-2 Magnified view of FE model (a, b) and corresponding membrane strain predictions (c, d) with locations of interest indicated at the (a, c) channel inlet and (b, d) dimple cross-sections.

The plastic strain at location (i) of the channel inlet was estimated to be between 7.4 % (RT) and 9.9 % (250 °C) for the O temper sheet, and between 10.0 % (RT) and 12.9 % (250 °C) for the H24 temper. The average strain rate during deformation was estimated from the FE model to be between $3.0x10^{-2}$ s^{-1} (O-RT) and $6.0x10^{-2}$ s^{-1} (H24-250 °C). Consequently, the post-braze microstructure from location (i) of the channel inlet depended on both the forming temperature and initial sheet temper, as seen in Fig. 5-3. For the RT formed O temper sheet (Fig. 5-3a), the core alloy was characterized by coarse grains, with the grain size approaching the full sheet thickness, indicating that the sheet was recrystallized by strain induced boundary migration (SIBM) at this location [54, 57]. Furthermore, a thin, relatively uniform clad residue layer was present at the surface of the sheet. When the forming temperature was increased to 150 °C (Fig. 5-3b), a coarse core alloy characteristic of SIBM and uniform clad residue layer were observed at the radii of the channel inlet. However, directly adjacent to this region, where strain rapidly decreases (Fig. 5-2c), a stark contrast in the microstructure was observed. There, the core alloy was characterized by a mixture of small and elongated grains, similar to the pre-braze condition, suggesting recrystallization did not occur at that location during brazing. Furthermore, the thin clad residue layer transitioned to large, blocky grains protruding into the core layer, which are consistent with the morphology of liquid film migration (LFM) [12, 14]. A non-recrystallized core alloy and large surface grains consistent with LFM were prevalent across location (i) of the channel inlet for the O temper plate formed at 250 °C (Fig. 5-3c). On the other hand, the core alloy of the H24 sheets, which was originally comprised of pancaked grains from prior sheet processing (Fig. 3-1b), recrystallized during brazing, regardless of forming temperature (Fig. 5-3d and e). It should be noted that the recrystallized grains in the H24 sheets are finer than those characteristic of SIBM. As a consequence of core recrystallization, a uniform clad residue layer was present at the sheet surface, and no LFM was observed.
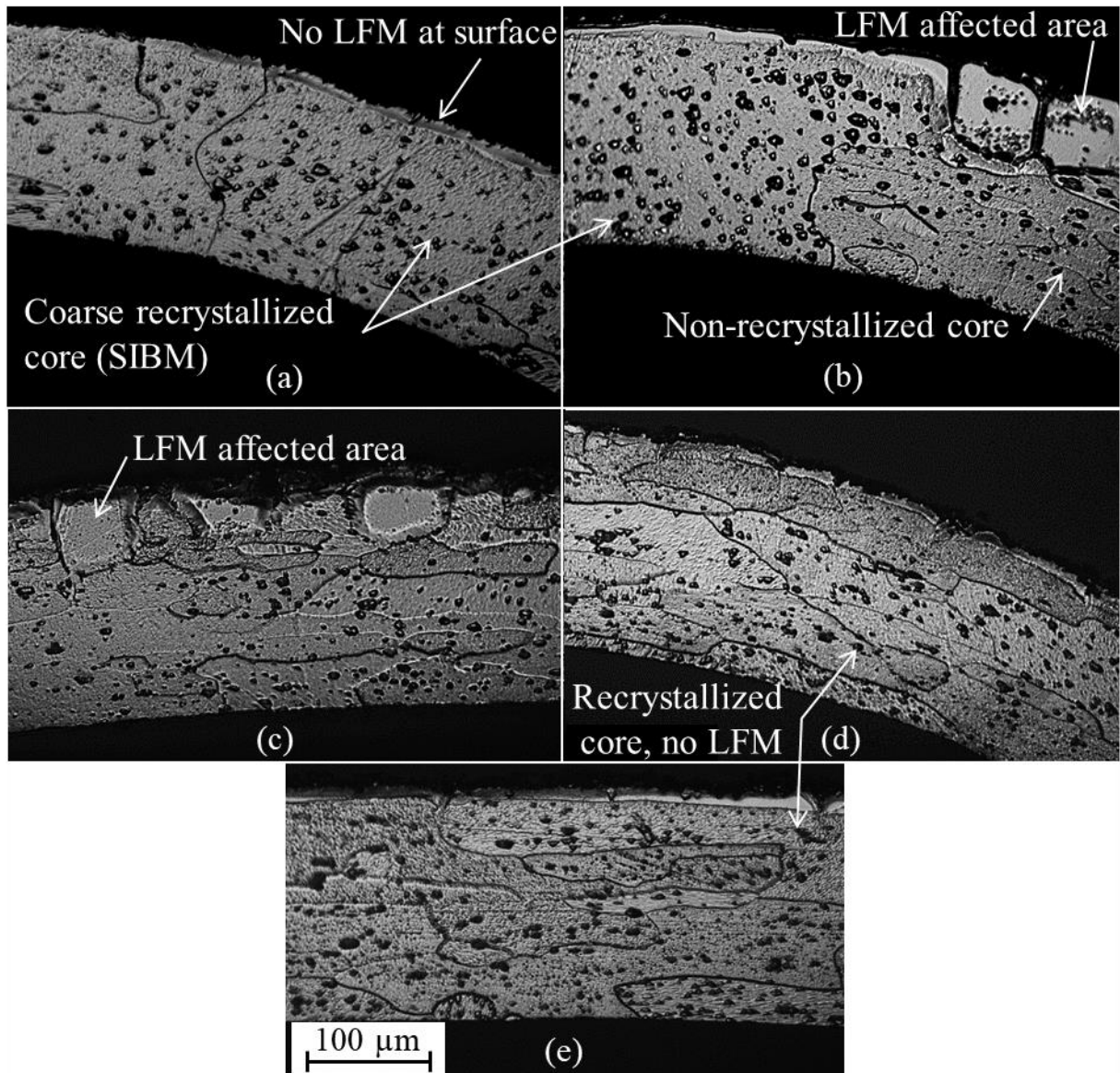
Fig. 5-3 Post-braze microstructures from location (i) for (a) O-RT, (b) O-150 °C, (c) O-250 °C, (d) H24-RT, and (e) H24-250 °C forming conditions.

The plastic strain at location (ii) in the channel inlet reaches a relatively low level, between 3.1 % (H24-RT) and 4.1 % (O-RT), and the average strain rate was estimated to be approximately 2.0×10^{-2} s^{-1} for all forming conditions. LFM and a non-recrystallized core were observed in the plates formed from the O temper sheet at RT and 150 °C (Fig. 5-4a and b). A non-recrystallized core was also found at location (ii) in the O temper plate formed at 250 °C (not shown), although LFM was not observed. Similar to location (i), the H24 post-braze

microstructure was insensitive to an increase in forming temperature, and a recrystallized core alloy with no LFM was observed at the surface (Fig. 5-4c and d).
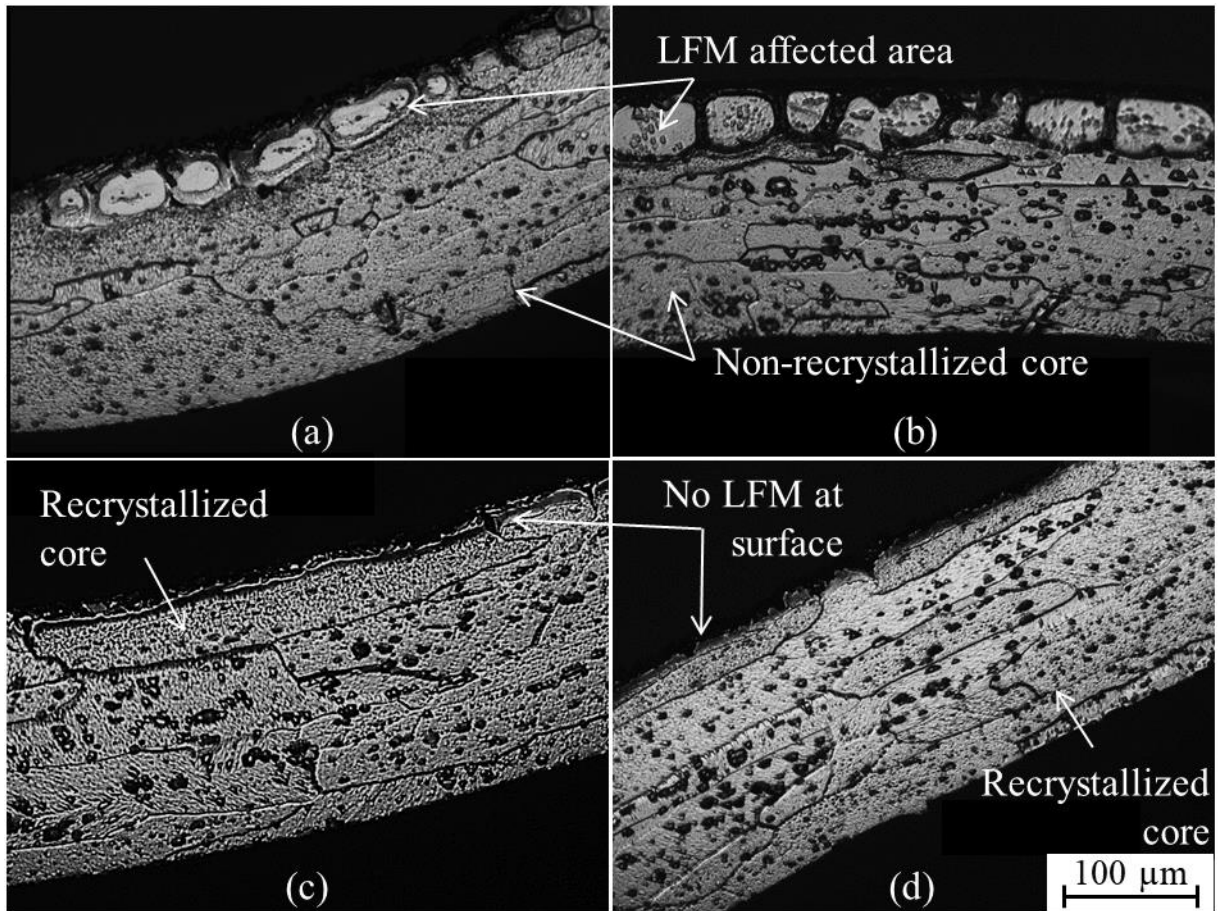
Fig. 5-4 Post-braze microstructures from location (ii) of the channel inlet for (a) O-RT, (b) O-150 °C, (c) H24-RT, and (d) H24-250 °C forming conditions.

The post-braze microstructures at the faying surface of the formed dimples, where for all forming conditions the plastic strain and strain rate were estimated to be 4 % (Fig. 5-2d) and $6.0 \times 10^{-2}\,\text{s}^{-1}$, respectively, are shown in Fig. 5-5. A non-recrystallized core alloy and LFM attack were observed in the dimples of the O temper plates for all forming temperatures (Fig. 5-5a to c), while the H24 sheet again had a recrystallized core alloy without LFM for both forming temperatures (Fig. 5-5d and e).

81
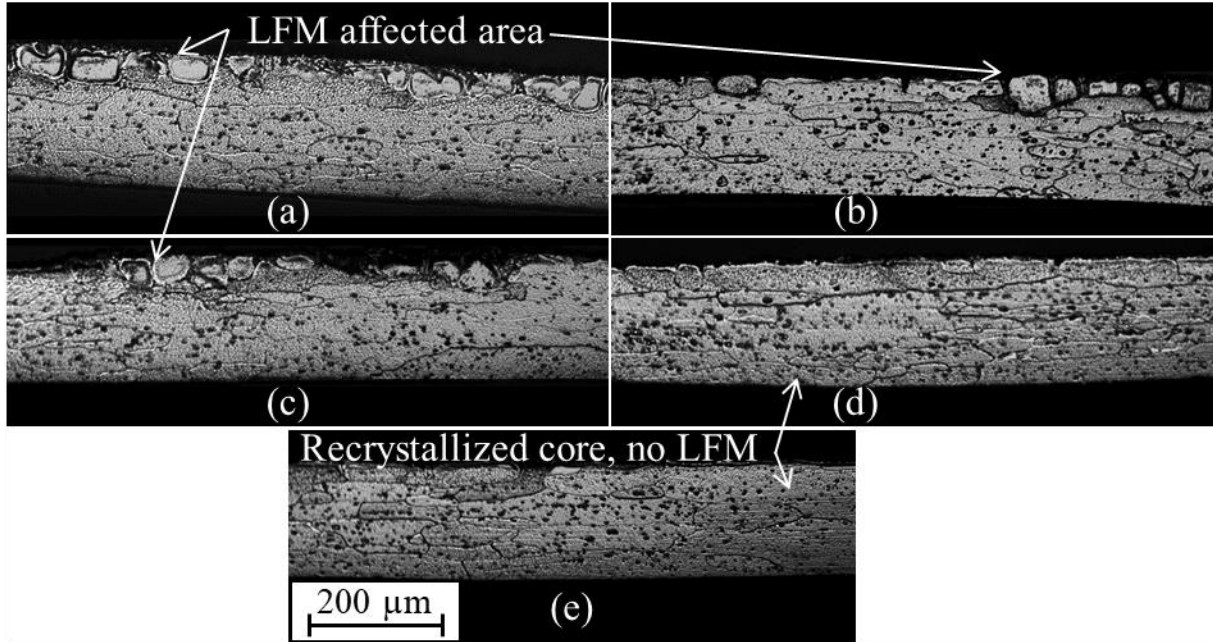
Fig. 5-5 Post-brazed microstructures at the faying surface of the dimples for the (a) O-RT, (b) O-150 °C, (c) O-250 °C, (d) H24-RT, and (e) H24-250 °C forming conditions.

5.4. Discussion

Overall, the results from the formed battery plates were consistent with the results from the warm deformed uniaxial coupons from Chapters 3 and 4, despite an order of magnitude increase in the strain rate for the formed plates. The strain rate at the three locations of interest in the plate during deformation was estimated from the FE model to be between $2.0\text{x}10^{-2}\,\text{s}^{-1}$ and $6.0\text{x}10^{-2}\,\text{s}^{-1}$, while the strain rate in the prior tensile tests was $6.6\text{x}10^{-4}\,\text{s}^{-1}$. For the plate formed from the O temper sheet at RT, a non-recrystallized core and LFM were observed at locations with low strain (i.e. ≤ 4 %), while negligible LFM and a core alloy recrystallized through SIBM were found in locations of greater strain. For the O temper sheets formed at 150 °C, LFM and a non-recrystallized core were observed over a slightly greater range of strains than for RT forming. At the highest levels of strain studied in the plate (i.e. location (i) of the channel inlet), the coarse SIBM grains were observed in the core alloy (Fig. 5-3b). Finally, in the O temper plates formed at 250 °C, LFM was observed at locations with 4 % strain and locations strained up to 10 %. While warm forming can increase the material forming limits for the O temper sheet, it also extends the range of strains over which LFM will occur, and can shift its presence to critical brazing locations (Fig. 5-3c). The driving force for the LFM phenomenon was proposed to be the reduction of stored deformation energy within the core alloy by the migrating liquid

82

film [14, 69]. The extension of the regime over which LFM occurs when the sheets are warm formed has been attributed to the reduction in material flow stress and work hardening during warm forming, making it increasingly difficult to reach the critical level of stored energy to trigger recrystallization during the brazing cycle. Post-braze transmission electron microscopy images have shown that, in cases where LFM occurs, the core alloy undergoes recovery during brazing, leaving sub-grains in the core, which are a source of excess stored energy (Fig. 4-11d and f). The resultant post-braze microstructure will vary with strain throughout a component fabricated from the O temper sheet, and the spatial distribution of phases will change with an increase in forming temperature. Thus, warm forming will require careful consideration of the physical design of the components with respect to local strains and strain rates imparted to the sheet, compared to RT formed components.

In contrast, the H24 temper sheet microstructure was characterized by a recrystallized core alloy and a uniform clad residue layer, irrespective of location in the plate or the forming temperature. During processing of the H24 sheet, the sheet was rolled from an intermediate thickness to the final sheet thickness, with only partial annealing afterward, leaving the final sheet in a partially work hardened condition. The microhardness results from section 3.4.2 showed that the H24 core alloy, even in the as-received condition, has a greater level of stored energy compared to O temper sheet strained to 12 % at RT. Thus, the battery plates formed from the H24 sheet have a sufficiently high level of stored energy at all locations to trigger recrystallization during the brazing cycle, eliminating the driving force for LFM. Warm forming of the H24 sheet at 250 °C did not alter the post-braze microstructure. During warm forming, the sheet was heated to 250 °C and held for less than 1 min; the temperature and time during warm forming were not high or long enough to cause significant recovery in the sheet. The warm formed sheet contained sufficient stored energy to induce recrystallization during brazing, and prevent the onset of LFM.

5.5. Summary

The results of the prior chapters indicated that the brazing performance of the O temper sheet could be impaired by increasing the forming temperature, while sheets initially in the H24 temper would not be adversely affected. However, these predictions were based on simplified uniaxial test results. In this chapter, the microstructure evolution during brazing within a scaled-

down heat exchanger component, with a geometry and forming conditions more akin to high volume production, was investigated. The results of the study led to the following conclusions:

1. The same metallurgical interactions observed in warm formed uniaxial tensile specimens were observed in the formed battery cooling plates after simulated brazing, at comparable levels of strain, despite greater strain rates in the formed plates. Of particular importance was the balance between core alloy recrystallization and the occurrence of LFM.

2. The post-braze microstructure of plates formed from the O temper sheet varied with local strain, where the local stored energy determined if recrystallization or LFM occurred during brazing. Warm forming altered the post-braze microstructure of O temper sheets by extending the range of strains over which LFM can occur. The extension of the LFM regime can lead to the occurrence of LFM at critical locations in warm formed components, which may not have been an issue with RT forming.

3. The duration and temperature during warm forming were not high enough to significantly reduce the stored deformation energy within the H24 sheet, allowing recrystallization to occur everywhere throughout the plates after forming at both RT and 250 °C. Consequently, LFM was not observed at any location in the H24 plates.

6. Brazing Performance of Warm Formed Battery Cooling Plates[4]

6.1. Introduction

The objective of this thesis is to investigate the effects of forming temperature and initial sheet temper on the brazing performance of laminate Al alloy sheets used in automotive heat exchanger production. The results of Chapter 3 noted that the predicted brazing performance, as a function of strain and response to forming temperature, would differ for the two sheet tempers studied. The predicted brazing performance of H24 sheet was shown to be independent of both strain and forming temperature, due to the ability of the core alloy to recrystallize during the brazing cycle. On the other hand, the predicted brazing performance of the O temper sheet not only varied with applied strain, but this relationship was shown to distinctly change when the forming temperature increased to 250 °C. The occurrence of liquid film migration (LFM) and the inability of the core alloy to recrystallize over a range of strains in warm formed specimens was predicted to result in poor brazing performance. The measurements presented in Chapter 4 corroborated the findings for the O temper sheet, showing that the sagging distance of O temper sheet formed above 150 °C was unacceptably high, and were consistent with LFM at the sheet surface and a recovered core alloy after brazing. The microstructure evolution in formed battery cooling plates during simulated brazing, presented in Chapter 5, showed that microstructures similar to those presented in Chapters 3 and 4 were found throughout the plate, at comparable levels of strain.

The results outlined in the previous chapters did not consider the actual brazing behaviour of warm formed components, but instead examined the effect of warm forming on interactions within the sheet, from which brazing performance was inferred. The purpose of this chapter is to test these predictions, by fabricating scaled-down functional battery cooling plates. The brazing performance of the components was studied at the component level, using radiography to investigate braze fillet formation within the plate, and by the ability of the plates to withstand an internal pressure. The microstructure was analyzed to understand the fundamental processes occurring within a real assembly, and a finite element model were used to facilitate comparison with prior results from the uniaxial specimens reported in Chapters 3 and 4.

---

[4] The contents of this chapter have been adapted from: M. J. Benoit, K. B. Han, S. Winkler, M. J. Worswick, and M. A. Wells, "An assessment of the brazing behaviour of warm formed automotive heat exchangers." The manuscript has been prepared and is to be submitted.

6.2. Experimental Procedure
6.2.1. Materials and Sample Preparation

Scaled-down battery cooling plates were formed from industrially produced Al brazing sheets, received in the: (i) fully annealed (i.e. O) and (ii) work hardened and partially annealed (i.e. H24) sheet tempers. The composition and initial thicknesses of these sheets are described in section 3.2.1. The Ni-based braze promoting layer discussed in section 5.2.1 was also present on the clad alloy surface, to disrupt the oxide layer during brazing and allow liquid clad flow.

During preliminary brazing trials with the formed plate design used in Chapter 5, it was observed that the coolant channel would sag and then completely collapse during the brazing cycle, making the part unusable. A second iteration of the plate design was developed, where the number of formed dimples within the channel was increased from 7 to 21. This extra support was able to prevent the channel from collapsing during brazing. Nevertheless, few of the dimples successfully formed brazed joints, and the location of successfully joined dimples was not consistent across samples. A number of non-brazed dimples along the length of a coolant channel can be seen in the opened section in Fig. 6-1.
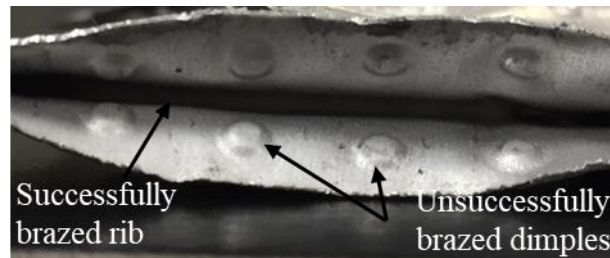
Fig. 6-1 Non-brazed dimples along a coolant channel in the second design iteration of the battery cooling plate.

Digital optical microscope measurements of the clad surface of the formed plate revealed that the faying surfaces of the dimples were lower than the outer flange and ribs of the plate design. As a result, when two plates were assembled for brazing, the dimple surfaces were not in contact, and a joint could not form. As advised by technical staff at Dana Canada, a third design iteration of the battery cooling plate was developed, where the nominal height of the formed dimples was 76 µm (0.003") greater than the height of both the outer flange and the adjacent ribs. The plates were formed from both O and H24 temper sheets, using forming

temperatures of RT, 150 °C, and 250 °C. Forming was conducted using the same procedure and parameters as outlined in section 5.2.1. The resultant formed geometry can be seen in Fig. 6-2.
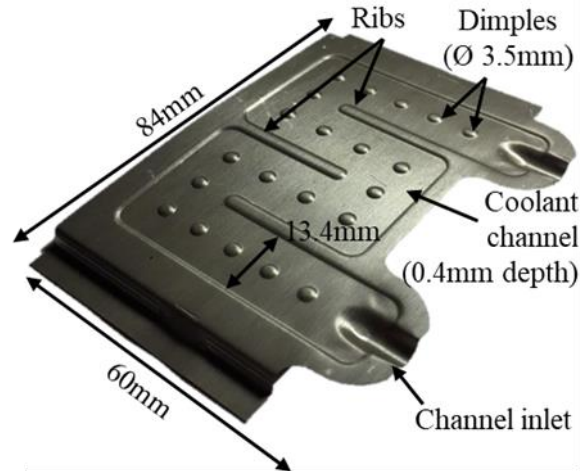
Fig. 6-2 Formed battery cooling plate, with the major formed features noted. The clad alloy surface is facing 'up' in the figure.

The formed plates were ultrasonically cleaned in acetone, followed by an industrial aqueous de-greasing procedure to remove surface contaminants such as residual lubricants and oils. After cleaning, two plates of the same forming condition were clamped together in a fixture, such that the clad layer of the outer flange, rib, and dimple surfaces of the two plates would contact one another in a sandwich-type joint configuration [40]. Unfortunately, poor brazed dimple yield was still observed during preliminary brazing trials with the third iteration of the formed plate design. At this point, a new carbon-based fixture was machined, where the dimensions of the milled channel in the carbon blocks matched the nominal dimensions of the formed channel in the plate. Thus, the fixture applied pressure to the flange and ribs of the plates, without directly applying pressure to the coolant channel. Tubular fittings were placed within the channel inlets during assembly, to provide attachment points for pressurized fluid lines, and a filler metal-flux paste mixture was manually applied to the channel inlet radii. The final assembly prior to brazing can be seen in Fig. 6-3a. A controlled atmosphere, multi-zone belt furnace was used to simulate a typical industrial brazing temperature profile. The belt speed and furnace temperatures were adjusted such that the assembly was exposed to a peak brazing

87

temperature of 600 °C for approximately 3 min. An example of a fully brazed assembly can be seen in Fig. 6-3b.
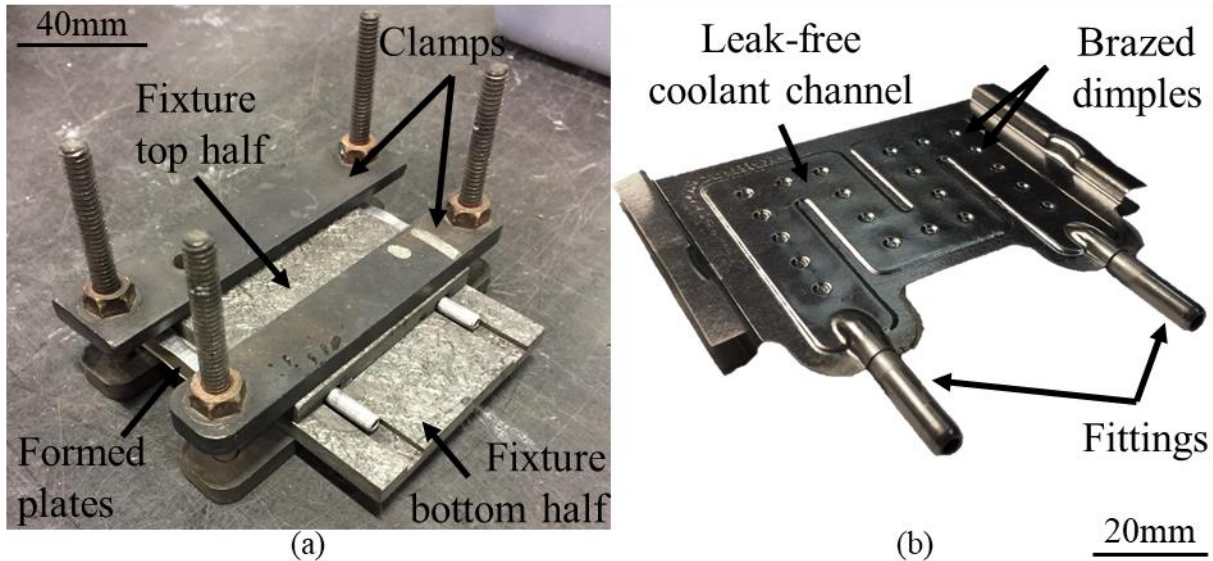
Fig. 6-3 Battery cooling plate (a) in fixture prior to brazing and (b) after the brazing cycle.

6.2.2. Finite Element Model

A finite element (FE) model of the third design iteration of the formed plate was developed using commercial LS-DYNA software. The model parameters and set-up were the same as those used in section 5.2.2, and additional detail on model development is provided by Han *et al.* [88, 89]. Strain predictions at the sheet mid-plane throughout the plate were used in Chapter 5. However, due to combined tensile and bending loading conditions, the strain also varies through the sheet thickness, which was captured using seven integration points. In this chapter, the effective plastic strain predictions are taken from the second integration point from the clad alloy surface, at a depth of approximately 25 µm; this location is of particular interest, as it corresponds to the location of the clad-core interface. The selection of this integration point was intended to provide a more realistic estimate of the level of deformation present directly ahead of the clad alloy when melting occurs, to better understand the resultant post-brazed microstructure.

6.2.3. Brazing Assessment

All brazed prototype battery cooling plates were non-destructively examined using 2D digital radiography. Defects such as inconsistent or missing brazed joint fillets and irregular liquid clad pooling can be identified using this technique due to localized differences in contrast. All radiography was performed at Dana Canada using a North Star Imaging X5000 system, with a Varian flat panel x-ray detector. Scans were performed with an accelerating voltage of 110 kV, 110 µA current, resulting in a reported resolution of 0.046 mm.

Leak tests were also performed to assess the continuity of the brazed joints at the clamping surfaces around the coolant channels and the overall integrity of the plate design [2]. The fittings in the channel inlets were attached to a custom fixture, which was connected to a pressurized air supply. The assembly was submerged in a pool of water, and an internal pressure of 0.28 MPa (40 psi) was applied to the coolant channels. Any leaks in the brazed component were identified by the formation of air bubbles in the pool during the test.

The brazed battery cooling plate samples were sectioned to investigate the microstructure and brazed joint formation. Cross-sections were selected using information from the FE model of the formed plate and radiography of the brazed plates. Cross-sections were cold mounted and prepared for optical microscopy by grinding and polishing, using 0.04 µm colloidal silica for final polishing. The cross-sections were etched with Keller's reagent for 110 s to reveal the post-brazed grain structure. A Hitachi SU3500 scanning electron microscope (SEM) equipped with energy dispersive x-ray spectroscopy (EDS) was used to further investigate the post-braze microstructure and local compositions, using an accelerating voltage of 30 kV.

6.3. Results

Fig. 6-4 shows predicted contours of effective plastic strain (von Mises) in a formed plate, as well as the corresponding distributions of strain versus position along two sections of interest for the three forming temperatures. The strain predictions in shown Fig. 6-4 are taken from the O temper FE model; the predictions for the H24 sheet produce slightly different values, due to different material hardening behaviour and the earlier onset of diffuse necking of the H24 sheet at elevated forming temperatures, but have the same overall trend as a function of position. From Fig. 6-4a, it can be seen that the cross section through the channel inlet was taken 10 mm from the front edge of the plate, as opposed to 4 mm as in Chapter 5. The microstructure analysis was

shifted to the cross section 10 mm from the front of the plate, to avoid complicating the analysis with the fittings and filler metal paste placed in the channel inlet prior to brazing (section 6.2.1). From the figure, there is a significant variation in strain along the section. For the cross-section through the dimples and ribs, the strain data are plotted only up to the middle rib, due to symmetry assumptions in the model. From the figure, it is clear that the local strain rapidly changes along the cross-sections as formed features are encountered, with high levels of bending strain at the feature radii.
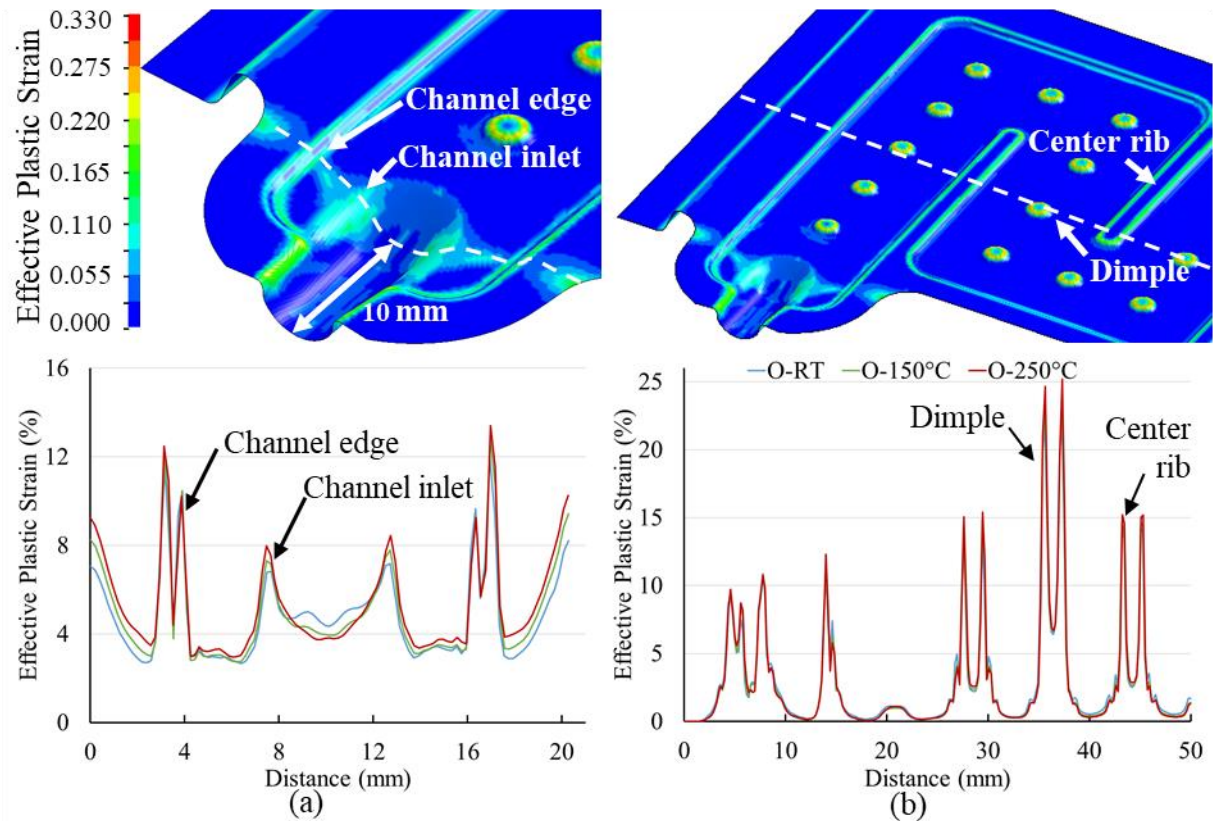
Fig. 6-4 FE model effective plastic strain predictions along the cross section, as indicated by the dashed white line, (a) through the channel inlet 10 mm from the front of the plate and (b) through the dimples and ribs.

Plates from all forming conditions were successfully brazed. During preliminary brazing trials, the only identifiable leaks in the plates occurred at the channel inlet-fitting interface, due to an insufficient amount of filler metal paste applied to this location prior to brazing. After increasing the amount of filler metal paste applied to the fittings, all plates were found to be

leak-free, demonstrating the integrity of the brazed joints and soundness of the prototype battery cooling plate design.

Digital radiography images of as-brazed assemblies from selected forming conditions are presented in Fig. 6-5. Some non-uniform clad pooling was identified at the flanges of the plates (indicated by arrows). Brazed joint fillet formation was also identified in Fig. 6-5 by areas of increased contrast around the edges of the channels, and around each dimple, due to the increased amount of material at these locations. Instances of missing or inconsistent brazed joint fillet formation (circled in the figure) were identified at the edges of the channels and at a small number of dimples. The number of brazed fillet inconsistencies was greater for H24-RT plates than for any other forming condition. However, as neither clad pooling nor inconsistent brazed fillet formation resulted in leaks or failure of the brazed plates, these defects were not of particular concern. The lack of inconsistencies in brazed fillet area for the H24-250 °C plate in Fig. 6-5d indicates the benefit of using warm forming to reduce springback and improve brazing performance of H24 sheet.
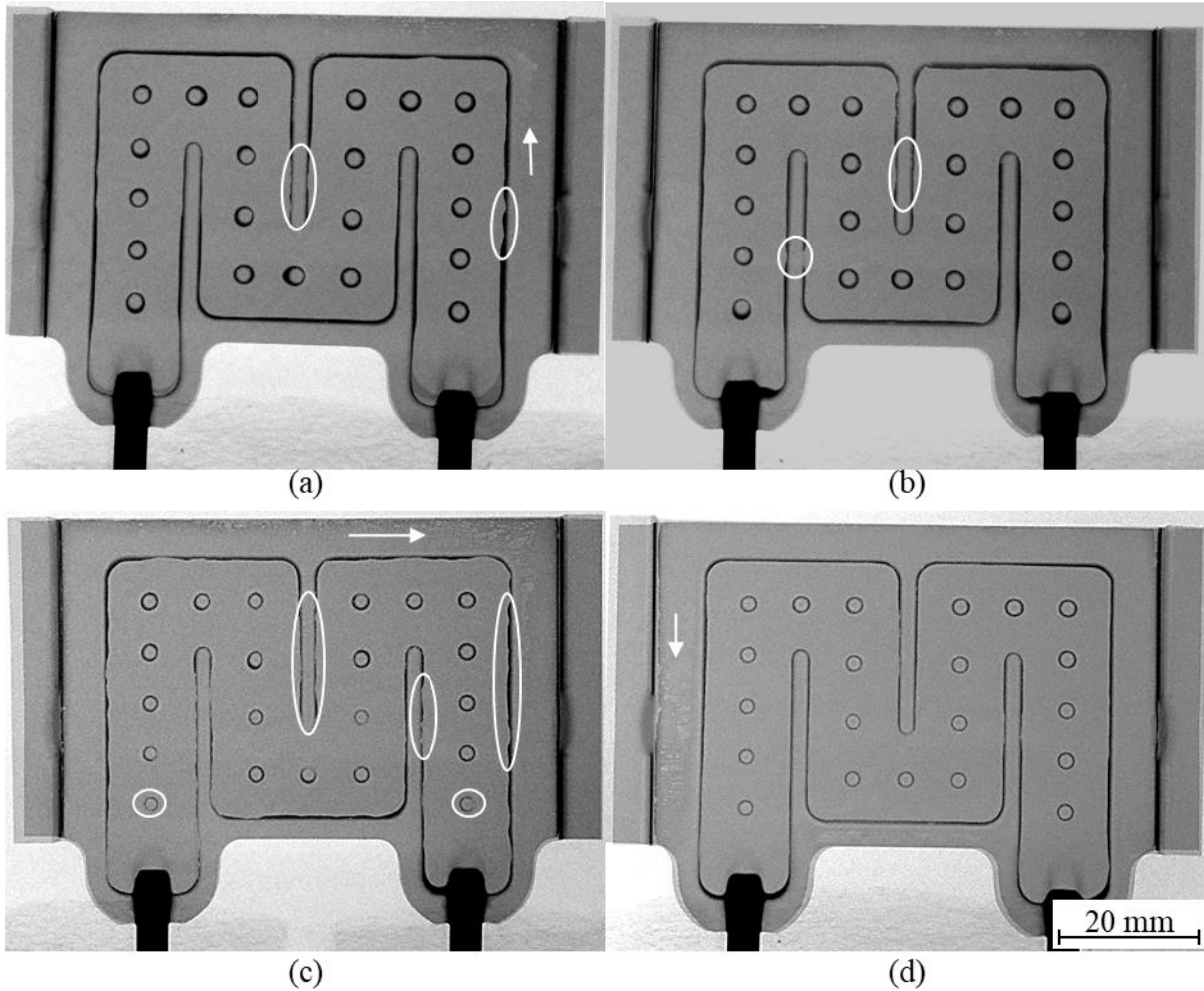
Fig. 6-5 2D digital radiography of brazed battery cooling plates fabricated from (a) O-RT (b) O-150 °C, (c) H24-RT, and (d) H24-250 °C forming conditions. Instances of clad pooling are indicated by arrows, while missing or inconsistent brazed fillets are circled.

Micrographs of brazed fillets at dimples and ribs from various forming conditions are shown in Fig. 6-6. As expected, the re-solidified joints are characterized by primary α-dendrites (Al-Si solid solution), surrounded by the Al-Si eutectic structure [48]. From the micrographs, it can be seen that the core grain structure, and consequently the interface with the re-solidified metal, changes with the forming condition.
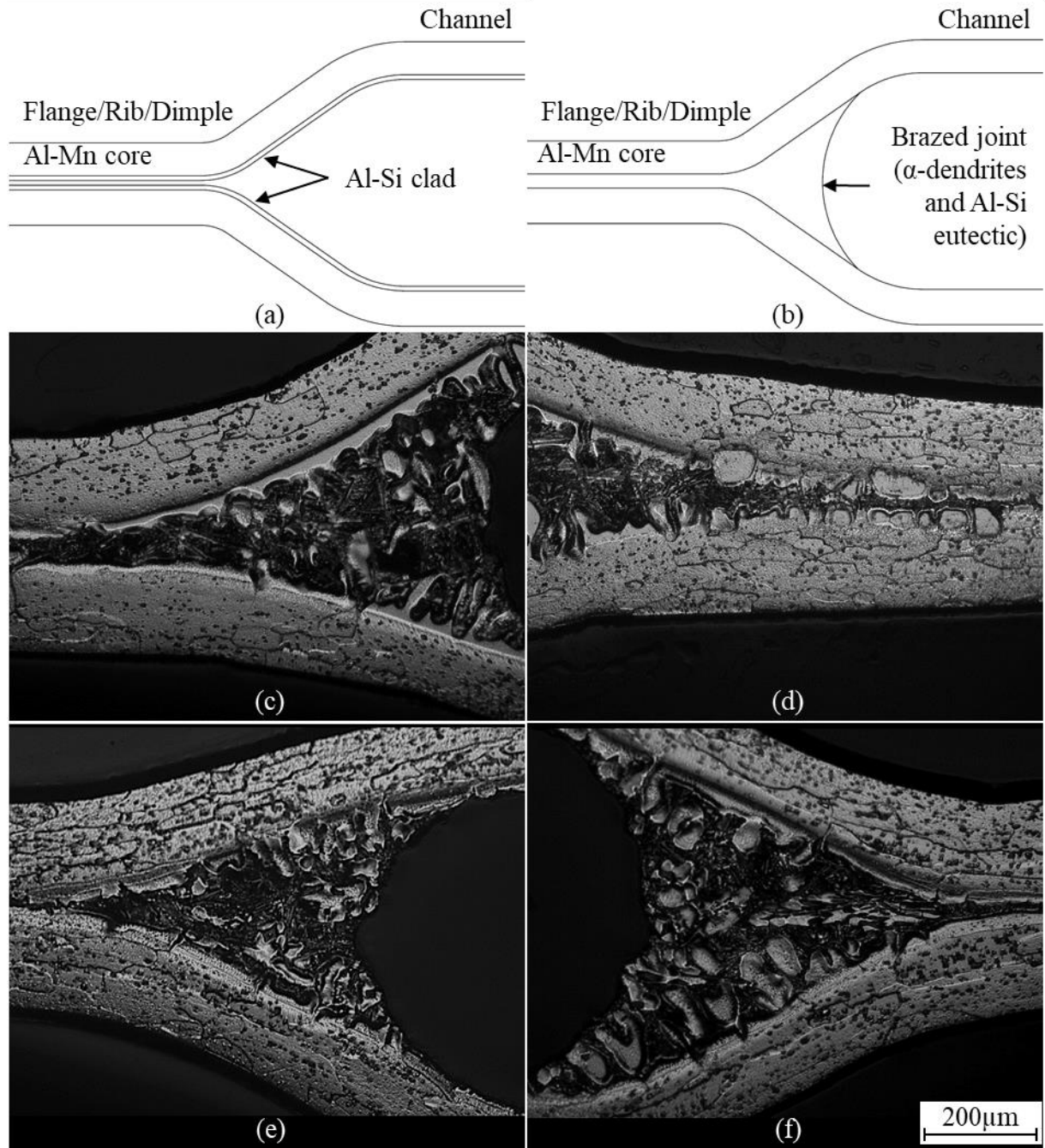
Fig. 6-6 Schematic of brazed joint fillet formation at plate faying surfaces (a) before and (b) after brazing. Actual brazed joints at dimples for (c) O-RT and (d) O-250 °C, and at ribs for (e) H24-RT and (f) H24-250 °C forming conditions.

The differences in post-braze microstructures for different forming conditions are more obvious in Fig. 6-7 and Fig. 6-8. The microstructures presented in Fig. 6-7 were taken from unsuccessfully brazed dimples in otherwise leak-free battery cooling plate assemblies, joined

during the development of the brazing process. Thus, only one of the two dimple faying surfaces is shown in the figure for each forming condition, which enabled the microstructure to be studied without the confounding effect of a large volume of re-solidified clad in a brazed fillet. The effective plastic strain at the clad-core interface varied from 6.7 % at the 'top' of the dimple (i.e. the faying surface) to 25.2 % at the radii (Fig. 6-4b). A difference in the re-solidified clad morphology and core alloy microstructures can be seen for the two sheet tempers in Fig. 6-7. A number of blocky grains characteristic of LFM were found protruding into the core layer at the dimple faying surface of the O temper sheets for all forming temperatures, while a more uniform re-solidified layer was found at the surface of the H24 sheets. The O temper post-braze core alloys were characterized by two types of grains: (i) small, non-recrystallized grains at locations of relatively low strain, such as directly below the LFM grains at the dimple faying surface, and (ii) coarse elongated grains characteristic of strain induced boundary migration (SIBM) at the dimple radii. The coarse grains are particularly evident in Fig. 6-7a and c, and it can be seen that the re-solidified clad at these grains is thin and fairly uniform. On the other hand, the H24 temper sheet post-braze core alloy was comprised of recrystallized grains elongated along the sheet rolling direction in both cases.
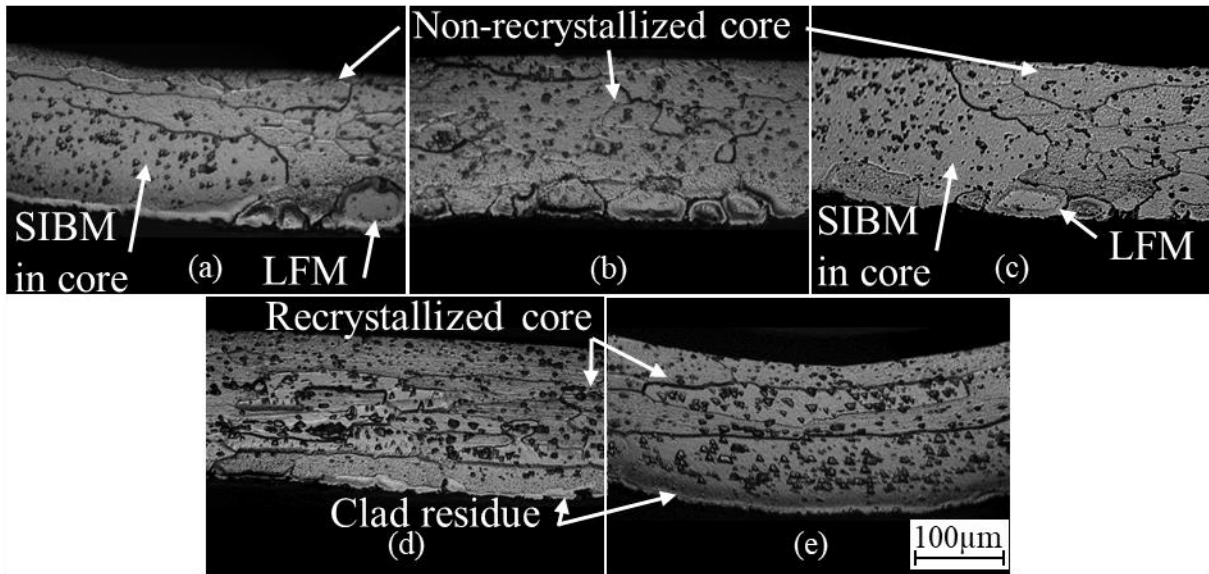
Fig. 6-7 Post-braze microstructure from unsuccessfully brazed dimples in battery cooling plates for (a) O-RT, (b) O-150 °C, (c) O-250 °C, (d) H24-RT, and (e) H24-250 °C forming conditions. Thus, only one of the formed plates is shown in each image, and the clad alloy surfaces are located at the bottom. Dark spots in the image are etching pits from second phase particles, due to the long etch time to reveal grain boundaries.

The post-braze microstructures from a location 8 mm along the channel inlet cross-section (see Fig. 6-4a) are presented in Fig. 6-8. While a brazed joint is not expected at this location, this location is exposed to the coolant during operation of the heat exchanger. Since the sheet corrosion resistance depends on the phases present after brazing [13], the microstructure evolution during brazing at this location is of critical importance. The predicted strains at this location are relatively low, and rapidly change between 3 % and 8 % (Fig. 6-4a). The overall microstructure trend is similar to that of the dimples, in that the re-solidified clad morphology and core alloy microstructures are distinctly different for the O and H24 temper sheets. Blocky grains protruding into the core again characterize the re-solidified clad surface of the O temper sheet. This morphology was found in both the top and bottom formed plates in the assemblies, indicating that it occurs despite gravity. The O temper post-braze core was characterized exclusively by non-recrystallized grains, similar to the pre-braze grain structure; unlike the dimples, no coarse and elongated grains were observed at the channel inlet. On the other hand, no obvious interactions were observed at the re-solidified surface of the H24 sheet; the remaining re-solidified clad was thin and of relatively uniform thickness. Similar to the dimple

95

microstructure, the H24 core alloy was comprised of coarse, elongated, recrystallized grains for both forming temperatures.
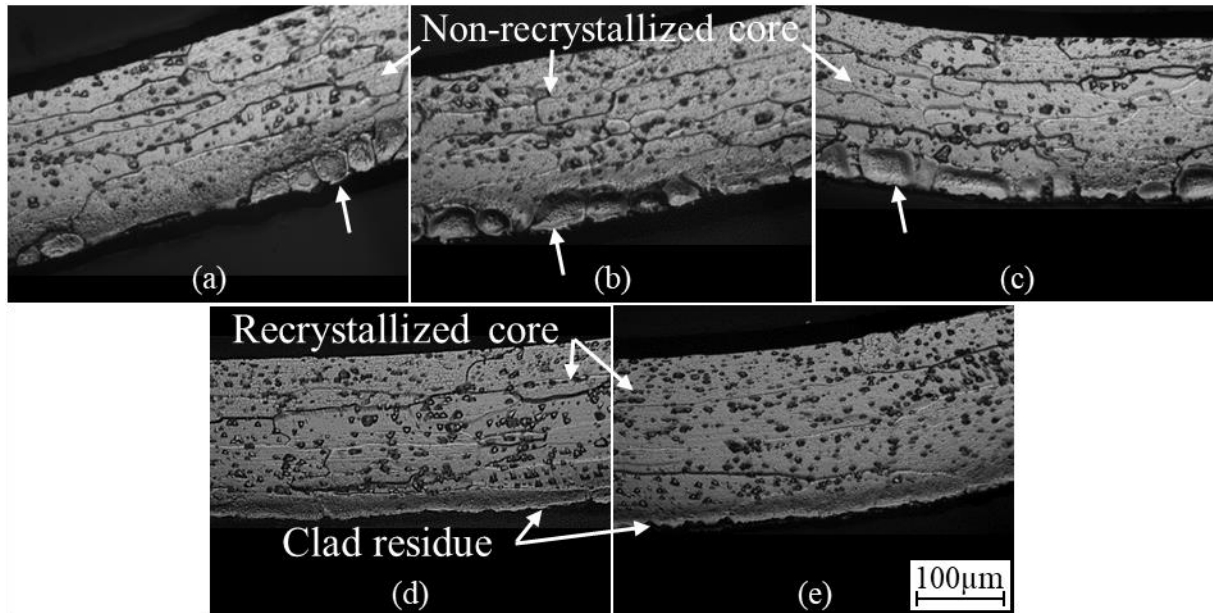
Fig. 6-8 Channel inlet post-braze microstructure at the cross section 10 mm from the front of the plate for (a) O-RT, (b) O-150 °C, (c) O-250 °C, (d) H24-RT, and (e) H24-250 °C forming conditions. The clad layer is at the bottom of each image.

The SEM and EDS data presented in Fig. 6-9, taken from the O-250 °C post-braze sheet (Fig. 6-8c), provide more details on the nature of the blocky re-solidified clad morphology. From the SEM image, the blocky surface grains (labelled 'LFM affected area'), have a thickness on the order of 50 µm, twice the initial clad layer thickness. The affected area is nearly void of all second phase particles, and is separated from the remaining core alloy by an interface containing second phase particles. EDS line scan data for Si, Mn, and Ni content through these particles, along lines b and c, are given in Fig. 6-9b and c, respectively. The EDS data along line b show a simultaneous 'double peak' for Si and Mn content across the interface. A sharp increase in Ni content was observed directly between the two peaks in the Si and Mn data. For line scan c, the Si content was high within the affected area (note the change of scale on the y-axis), before falling slightly to a still relatively high level in the core directly adjacent to the interface. The Mn content increased through the affected area as the interface was approached, at which point

the Mn concentration plateaued around the nominal value in the core. A sharp peak in the Ni content was again evident at the interface.
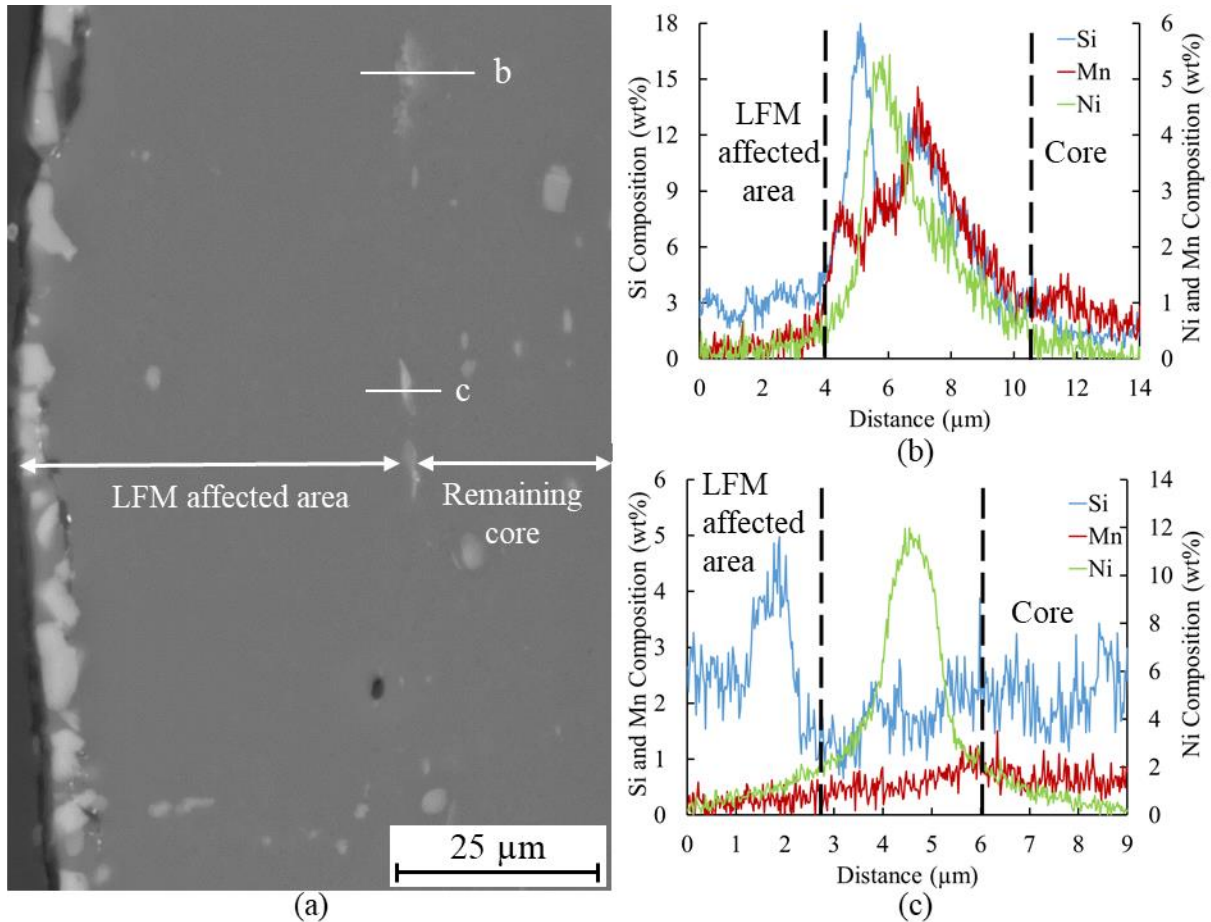
Fig. 6-9 (a) SEM image from the post-braze channel inlet cross-section, from an O-250 °C condition plate. Si (blue), Mn (red), and Ni (green) compositions, taken along lines b and c, are given in (b) and (c), respectively. Note change of scale and label on the y-axis.

6.4. Discussion

The results presented in this chapter provide new insights for processing technology advances and fundamental metallurgical processes occurring at the microstructure-scale during brazing. In the current study, the primary advantage of warm forming was to reduce springback of the H24 sheet, which led to more consistent braze joint formation when the sheet was formed at 250 °C compared to RT. The utility of warm forming to improve component flatness and, consequently, brazing performance of H24 sheet is expected to be even more apparent with full-scale geometry, where the linear deviation from flatness will be greater. Furthermore, the current

results demonstrate that warm forming, up to 250 °C, does not negatively impact the brazing process by, for example, inducing Si diffusion into the core and reducing liquid clad formation [50, 52], or preventing core recrystallization in H24 sheet due to dynamic recovery during warm forming. Thus, warm forming can be used to expand design possibilities of next generation heat exchangers by increasing the material forming limits, and to enable the use of higher initial strength sheets by decreasing springback.

The results for the H24 sheet are well aligned with the results from the uniaxial test results of Chapters 3, in that no difference in brazing performance was predicted for an increase in forming temperature to 250 °C. However, in Chapters 3 and 4 it was predicted that brazing of O temper sheets formed at 250 °C would result in excessive levels of LFM, depleting the liquid clad available for brazed joint formation, but plates were successfully brazed for all forming temperatures in the current study. As previously noted, warm forming was simulated in the prior chapters using uniaxial samples strained in a furnace, and during the brazing heat treatments, the samples were nearly horizontal, so the liquid clad alloy did not flow. In the present work, a number of capillaries were formed when the plates were brought into contact by the brazing fixture. During the brazing heat treatment, the liquid clad flowed to the faying surfaces to form brazed joints by capillary action. Since brazed joint fillets are formed with liquid clad from the area surrounding the faying surfaces, not just the clad at the faying surfaces, brazed joints were successfully formed in the plates, even with localized instances of core dissolution by the liquid clad (Fig. 6-6d).

The re-solidified clad within brazed joint fillets was comprised of a mixture of α-dendrites and Al-Si eutectic (Fig. 6-6). Away from the braze joint locations, two distinct re-solidified clad morphologies were observed: (i) a relatively uniform layer on the surface of the core grains and (ii) blocky grains protruding into the core alloy. The re-solidified layer of relatively uniform thickness is the clad alloy residue (section 2.3), which forms on the surface of the sheet at locations far from the brazed joints [46, 47, 91]. During non-equilibrium, diffusion-controlled melting of the clad alloy, Si-rich liquid first forms at the clad alloy grain boundaries, and is drawn by surface tension to the faying surfaces to form the brazed joint. A relatively uniform layer of pro-eutectic Al-Si solid solution, consistent with the solidus composition, is left at the sheet surface with little Al-Si eutectic phase. The interface between the clad residue and core is planar, as a negligible amount of core dissolution by the liquid clad

occurs [45]. This re-solidified morphology was observed for the H24 sheet in all cases, and for the O temper sheet where the core was characterized by coarse grains.

The blocky grains at the surface are the result of liquid film migration (LFM), as evidenced by a number of characteristics of the LFM process (section 2.4.3). The resultant morphology appears as large Al-Si solid solution grains protruding into the core, void of second phase particles and consistent with the solidus composition, reducing the remaining core thickness [12, 57, 69]. This morphology is consistent with the present study, although the depth of attack in the battery cooling plates was less severe than that observed in the prior chapters, since the liquid clad flowed due to gravity and capillary flow in the formed plate geometry, rather than pooling on top of the core as in a horizontal sample.

When the heat exchanger cools from the brazing temperature and the liquid film solidifies, clusters of second phase particles are expected at the interface with the remaining core, due to the high alloying content of the liquid film from the dissolved core precipitates [12, 16, 69]. While the exact identification of second phase particles is beyond the scope of this chapter, the line-scan data from Fig. 6-9 nevertheless provide useful insights. Fig. 6-9b and c indicate that the particles at the interface are rich in Si, Mn, and Fe (Fe was omitted from the plots for clarity). These are likely the α-$Al_{15}(Mn, Fe)_3Si_2$ particles commonly observed in the post-braze condition [3, 17, 21]. Furthermore, both line scans revealed the presence of Ni-rich particles at the interface, which are likely one of the Al-Ni intermetallic phases (e.g. Al_3Ni), reported to be present after the Al-Si-Ni ternary reaction [43]. Wittebrood [14] previously argued that since all Ni in the brazing sheet was from the braze-promoting layer at the clad alloy surface, its presence at the interface with the remaining core after brazing demonstrated that the migrating liquid film was maintained by liquid transport along the affected area grain boundaries, and confirmed the post-braze morphology was the result of LFM.

Finally, the LFM driving force was proposed to be the reduction of stored deformation energy in the core [14, 65, 69]. As the liquid film sweeps through a recovered microstructure, the liquid cannot support the dislocation structure, and the stored energy is reduced. The results of this chapter provide indirect evidence for the strain induced LFM driving force, through the FE local strain predictions and the corresponding post-braze microstructure. The post-braze core alloy grains can be categorized into a few distinct groups.

The O temper core alloy microstructures directly below the dimple faying surfaces (Fig. 6-7a to c), and at the channel inlet cross-section (Fig. 6-8a to c), were similar to the pre-braze core grains and, thus, are likely recovered. The transmission electron microscope images in Fig. 4-11 revealed that sheets with similar levels of applied strain were recovered after brazing. As recovery is only a rearrangement and partial elimination of dislocations, some level of deformation energy remains in the sheet, which provides the LFM driving force upon reaching the clad alloy eutectic temperature during brazing [14]. The LFM morphology was found in each of these micrographs, directly below the recovered grains.

As the level of deformation increases, the driving force for recrystallization also increases. The dominant recrystallization mechanism for moderately deformed Al alloys (i.e. $\varepsilon \leq$ 20 %) is strain induced boundary migration (SIBM), discussed in section 2.4.2 [54]. Grains resulting from SIBM were found in the formed plate at the radii of formed dimples (Fig. 6-7a and c), where the applied strain was estimated to be $\varepsilon = 25.2$ % from the FE model. The SIBM grain thickness was in the order of the overall sheet thickness, and similar microstructures have been reported elsewhere [57, 56]. When these locations in the plate reached the clad alloy eutectic temperature during brazing, the stored energy in the core (i.e. the driving force for LFM) was eliminated. Clad residue formation on the surface of the SIBM grains was shown in Fig. 6-7a and c, which is in stark contrast to the LFM grains and recovered core alloy directly adjacent in the same micrographs. Theyssier and Driver [92] have also shown SIBM to be an important recrystallization mechanism for certain grain boundary combinations found in hot rolled Al alloys, although the deformation temperatures and amount of deformation were greater than the current study (300 °C-400 °C and $\varepsilon \geq 100$ %).

It is interesting that SIBM was observed in the O temper sheet formed at 250 °C (Fig. 6-7c), as it was not observed in the prior chapters at any level of applied strain at 250 °C. However, both the level of deformation and the strain rate in the formed plates were greater than in the prior chapters. The tensile coupons were stretched to a maximum 12 %, at a strain rate of 6.6×10^{-4} s^{-1}, while in this chapter, the FE model predicted plastic strain at the dimple radii clad-core interface was 25 %, with an average strain rate of 2.0×10^{-1} s^{-1}. While the Al brazing sheet work hardens during RT deformation, the effect is diminished at warm forming temperatures. However, Al brazing sheet has been shown to display strain rate sensitivity when forming above 100 °C (section 2.2). For example, Abedrabbo *et al.* [34] showed that for H24 AA3003 sheet,

the strain hardening exponent (n) decreased from 0.215 to 0.116, while the strain rate sensitivity exponent (m) increased from 0.003 to 0.080, as the forming temperature increased from RT to 260 °C. Clearly, the strain rate must be considered during warm forming of Al brazing sheet to understand the microstructure changes during brazing. If the material flow stress is approximately proportional to the square root of the dislocation density [25], the occurrence of SIBM in warm formed plate samples, but absence in prior uniaxial tests, may be explained by the greater strain rate sensitivity at elevated forming temperatures and higher local strains.

Finally, a threshold strain is eventually reached, at which point, recrystallization through nucleation and growth of new grains becomes possible. The post-braze microstructures throughout the H24 plates for both forming temperatures were recrystallized, and were insensitive to the local strain, due to the significant cold work already present in the sheet. The recrystallized grains were slightly elongated along the sheet rolling direction, similar to the recrystallized H24 microstructure observed elsewhere [2, 21]. As with the SIBM grains, the clad residue was present at the sheet surface, since the LFM driving force was eliminated prior to reaching the clad eutectic temperature during heating to the brazing temperature.

6.5. Summary

The brazing behaviour of scaled-down prototype battery cooling plates was assessed for O and H24 temper sheets, formed at RT, 150 °C, and 250 °C. The results of this chapter were also intended to test the predictions made from the results of the prior chapters. The following conclusions can be drawn from the results:

1. Leak-free battery cooling plates were successfully brazed for all sheet temper-forming temperature combinations. Warm forming of H24 temper sheet to reduce springback resulted in more consistent brazed joints in the plates. No obvious difference in brazeability was observed for O temper plates formed at different temperatures.

2. The re-solidified clad alloy surface away from the brazed joints was categorized into two distinct groups: (i) a thin, relatively uniform surface layer, or (ii) blocky grains protruding into the core alloy. The uniform layer was identified as the clad residue, while the blocky grains were the result of LFM. LFM grains were found only in O temper plates at

locations of relatively low local strain. In the brazed joint fillets, the re-solidified clad alloy was comprised of primary dendrites and the Al-Si eutectic structure, as expected for solidification of a nearly binary Al-Si hypoeutectic alloy.

3. The O temper post-brazed core alloy was either recovered, at locations of relatively low strain, or recrystallized by SIBM at locations with greater imparted strains. SIBM was observed in O temper sheets formed at 250 °C at the dimple radii, due to high local strains (i.e. 25.2 %) and increased strain rate sensitivity of the Al brazing sheet during warm forming. Further, the occurrence of LFM at locations with a recovered microstructure, but a clad residue layer at locations with a recrystallized core, suggests a strain-induced driving force for LFM.

4. The H24 temper post-brazed core alloy was recrystallized at all locations throughout the plate, due to the cold work imparted during sheet production. A clad residue layer was present at the H24 sheet surface after brazing at all locations.

7.   Discussion

The research outlined in the previous chapters has shown that the initial sheet temper, forming temperature, strain, and strain rate all play a role in determining the post-braze microstructure of the Al brazing sheet. Furthermore, the warm forming of uniaxial specimens was able to represent the post-braze microstructure in more complex formed components at locations of comparable strain reasonably well. However, some post-brazed microstructures were found in the formed cooling plates that were not observed in the uniaxial specimens, and are believed to be due to greater local strains and strain rates during forming of the plates. Additionally, brazing of the battery cooling plates showed that the brazing performance predictions made in Chapters 3 and 4 were not always able to accurately predict the ability to form brazed joints, since the brazing predictors did not account for the liquid clad flows in real assemblies. The first part of this chapter summarizes the relationship between process variables and the post-braze microstructure for the two sheet tempers studied, and discusses the implications these have on brazing and component design. As the two sheet tempers used throughout this thesis (i.e. O and H24) are processed to have significantly different initial microstructures and properties, and thus behave differently during brazing, they will be considered separately.

The brazed cooling plates described in Chapter 6 did not reveal any obvious differences in the brazing performance (i.e. ability to fabricate leak-free cooling plates), regardless or forming temperature or sheet temper. Thus, if differences exist between the different sheet temper-forming temperature combinations, they are expected to manifest in the performance of the plates. The second part of this chapter discusses the preliminary results of an internal corrosion test used to simulate corrosive failure during service of the cooling plates.

7.1.   Microstructure Evolution During Brazing
7.1.1. O Temper Sheet

A non-linear relationship between various brazing performance predictors and the level of strain imparted to O temper sheets prior to brazing has been shown in a number of past studies [12, 57, 65, 69, 70, 71]. In all cases, the worst predicted brazing performance occurred for low to intermediate levels of strain (i.e. 2 % to 7.5 %). This relationship is strongly correlated with the post-braze microstructure, where poor predicted brazing performance was consistent with a

non-recrystallized core alloy and the occurrence of liquid film migration (LFM) during brazing, while core alloy recrystallization in more highly strained sheets improves the predicted brazing performance by preventing LFM. Due to the relationship between the applied strain, predicted brazing performance, and observed post-brazed microstructure, the LFM driving force was proposed to be the reduction of stored deformation energy in the core alloy (section 2.4.3) [14].

Chapters 3 and 4 showed that both the liquid duration time (LDT) and sagging distance had a non-linear dependence on room temperature (RT) applied strain, demonstrating their suitability to predict brazing performance. Using these indicators, the brazing performance of the O temper sheet was predicted to be impaired when formed above 150° C, which was due to an increase in the critical level of strain necessary to trigger core recrystallization during brazing and, consequently, an increased range of strains over which LFM occurred. In addition, the results from these chapters provided both direct and indirect evidence for the stored deformation energy LFM driving force. Direct evidence came in the form of sub-grain boundaries observed directly ahead of the re-solidified liquid front in samples with large sagging distances, while a fully recrystallized core was present in forming conditions with small sagging distances (Fig. 4-11). Indirect evidence was provided by the change in the dependence of the LDT and sagging distance on applied strain when the forming temperature was increased and, consequently, the material flow stress was lowered.

The analysis of formed and brazed battery cooling plates in Chapters 5 and 6 showed that, in general, the microstructure phenomena occurring within the uniaxial specimens were also present in formed components, and at similar levels of strain. However, analysis of the formed plates provided two additional important observations. First, brazed joints were successfully created throughout the plates, despite the poor predicted brazing performance from the uniaxial results. Brazed joint formation was due to wetting and capillary flow of the liquid clad alloy to the joint locations, which did not occur in the uniaxial coupons. Second, certain microstructural phenomena were observed in the formed plates, which were not predicted to occur, based on the uniaxial specimens. For example, grains characteristic of strain induced boundary migration (SIBM) were observed at dimple radii in plates formed at 250 °C, but were not observed in any uniaxial specimens formed at 250 °C. However, it was difficult to attribute this result to a specific cause; both the strain and the strain rate at the dimple were greater than those applied to the uniaxial specimens, and the strain rapidly changed along the cross section

and through the sheet thickness, due to the more complex tensile plus bending loads in the plate. In contrast, the uniaxial specimens were limited in the range of strains studied, only experienced uniaxial tensile loading, and were restricted to one strain rate.

To better understand the effect of process parameters on the microstructure evolution within warm formed Al brazing sheet during brazing, interrupted tensile tests were performed using a range of strain rates and higher levels of strain; the test parameters are listed in Table 7-1. The same sample geometry and experimental set-up as described in section 3.2.1 was used. After stretching, 4.8 mm diameter discs were punched from between the extensometer markers on the gauge length of the tensile specimens. The disc samples were exposed to a simulated brazing cycle, consisting of a 3 min hold at 600 °C, using the differential scanning calorimeter as a controlled atmosphere furnace. Nitrogen gas of 99.999% purity was flowed through the furnace during the test. The heating and cooling rates were 20 °C/min up to 500 °C and 10 °C/min above 500 °C.

Table 7-1 Interrupted tensile test parameters used to study the microstructure evolution during brazing.

Forming Temperatures (°C)	Engineering Strains (%)	Average Engineering Strain Rates (s^{-1})
150, 250	4, 6, 10, 20	6.6×10^{-2}, 6.6×10^{-3}, 6.6×10^{-4}

The Al brazing sheet stress-strain data for all forming temperature-strain rate combinations are presented in Fig. 7-1, along with the RT data from Chapter 3. From the figure, the material behaviour clearly depends on both forming temperature and strain rate, and the level of work hardening rapidly decrease with increasing forming temperature. The material flow stress clearly decreases with increasing forming temperature, but increases with greater strain rates. As noted in section 3.3.1, a slight decrease in the stress-strain curves was observed during forming at 250 °C, due to the onset of diffuse necking. No clear decrease in stress was observed for samples stretched at 150 °C, so the strain can be considered uniform through the gauge length.
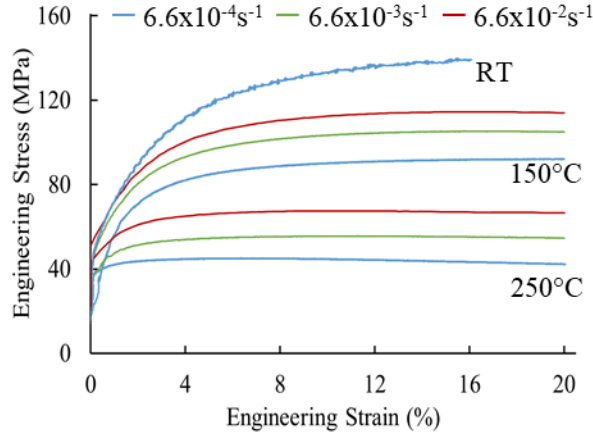
Fig. 7-1 Experimental stress-strain data for O temper sheet formed at different temperatures and strain rates. The RT stress-strain data from Chapters 3 and 4 are plotted for reference.

The extended Nadai phenomenological model, with a modified strain rate dependence term (Eq. 9), was shown to adequately describe the hardening response of Al brazing sheet [88]:

$$\sigma = C\left(\epsilon_p + \epsilon_0\right)^n \left(1 + B\log\left(\frac{\acute{\epsilon}}{\acute{\epsilon}_0}\right)\right) \qquad \text{Eq. 9}$$

where σ is the flow stress, ϵ_p and ϵ_0 are the plastic and reference strains, $\acute{\epsilon}$ and $\acute{\epsilon}_0$ are the true and reference strain rates, C is the strength coefficient, n is the work hardening exponent, and B is a material constant analogous to the strain rate sensitivity exponent. The model was modified from the original form by taking the logarithm of the strain rate term, rather than using a power law dependency, since the power law resulted in non-physical stress values at high strain rates [88]. The temperature dependence of the model is captured by allowing C, n, and B to vary with temperature. The general form of the equation used to calculate each value of C, n, and B is given in Eq. 10:

$$\beta = a + b\left(1 - \exp\left(c\frac{T - 273}{T_m}\right)\right) \qquad \text{Eq. 10}$$

where β is C, n, or B, T is the forming temperature, T_m is a fitting parameter, and a, b, and c are model parameters determined by non-linear regression of experimental data, and are different

for each of C, n, and B. Calculating n and B can quantify the relative importance of work hardening and strain rate sensitivity of the Al brazing sheet for different forming temperatures. Using data provided by Han [88], the variations in C, n, and B as a function of forming temperature were calculated (Fig. 7-2). From the figure, it can be seen that the Al brazing sheet hardening response during RT forming is governed by strain hardening, with negligible contributions from the strain rate. Conversely, the flow stress behaviour is more strain rate sensitive and less dependent on strain hardening when forming at 250 °C. Forming at 150 °C has contributions from both strain- and strain rate-hardening, as the values of n and B are nearly equivalent at this temperature. These observations are well aligned with the findings of Bagheriasl *et al.* [7], who showed that the effect of strain rate on total elongation of the Al brazing sheet only began to be noticeable at 150 °C.
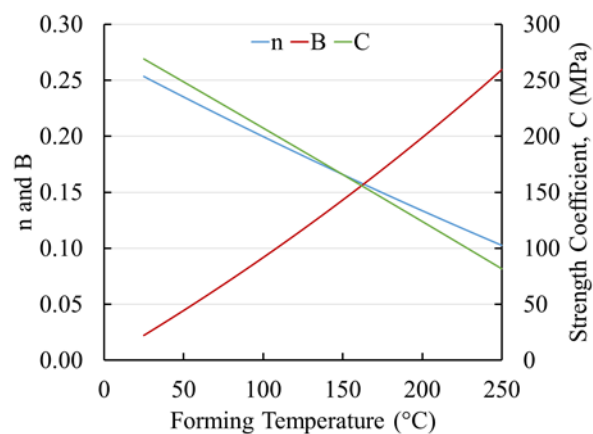
Fig. 7-2 Calculated Nadai model parameters C, n, and B, as a function of forming temperature, using data for O temper sheet from Han [88].

Interestingly, none of the past studies on the relationship between brazing performance and strain referred to the strain rate used, but as these studies were all concerned with RT forming, the strain rate effect was negligible. However, the strain rate effect on the material hardening behaviour becomes much more pronounced as the forming temperature is increased. The microstructures after simulated brazing at 600 °C for 3 min, as a function of strain and strain rate, can be seen in Fig. 7-3 and Fig. 7-4, for sheets formed at 150 °C and 250 °C, respectively. From the figures, the micrographs are categorized into four groups: (1) a non-recrystallized core with no LFM at the clad surface, (2) a non-recrystallized core with LFM at the clad surface, (3) a partially recrystallized core *via* SIBM with LFM at the clad surface, and (4) a fully

recrystallized core with clad residue at the surface. These are the same general interactions which were outlined by Wittebrood [14], although the case of the partially recrystallized core (i.e. case 3) has been added.
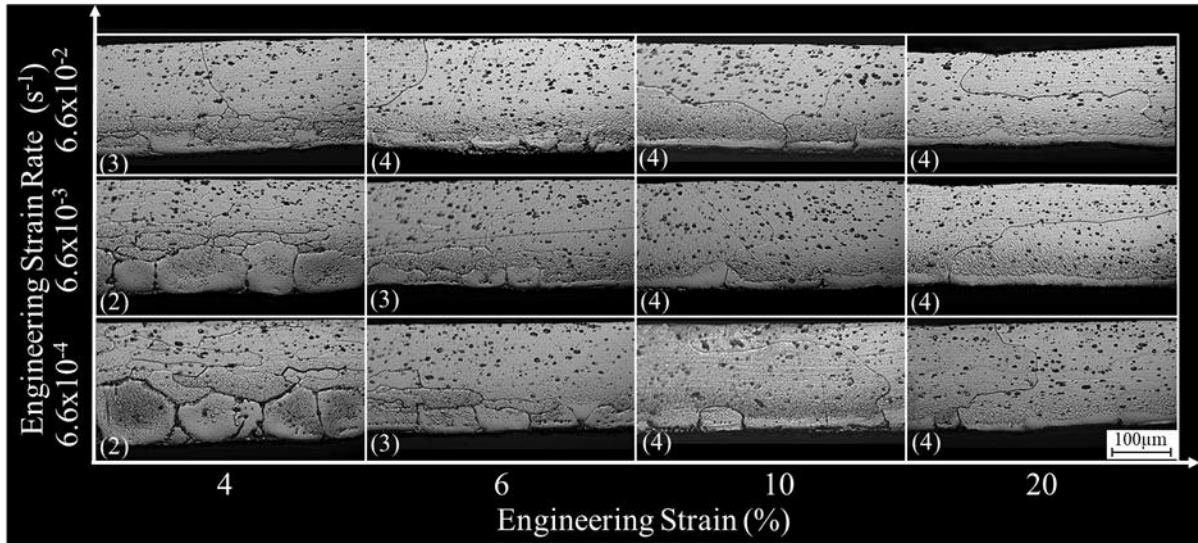
Fig. 7-3 Microstructures after simulated brazing at 600 °C for 3 min, as a function of strain and strain rate, for O temper samples formed at 150 °C. Numbers in parentheses indicate classification of interactions within the sheet.
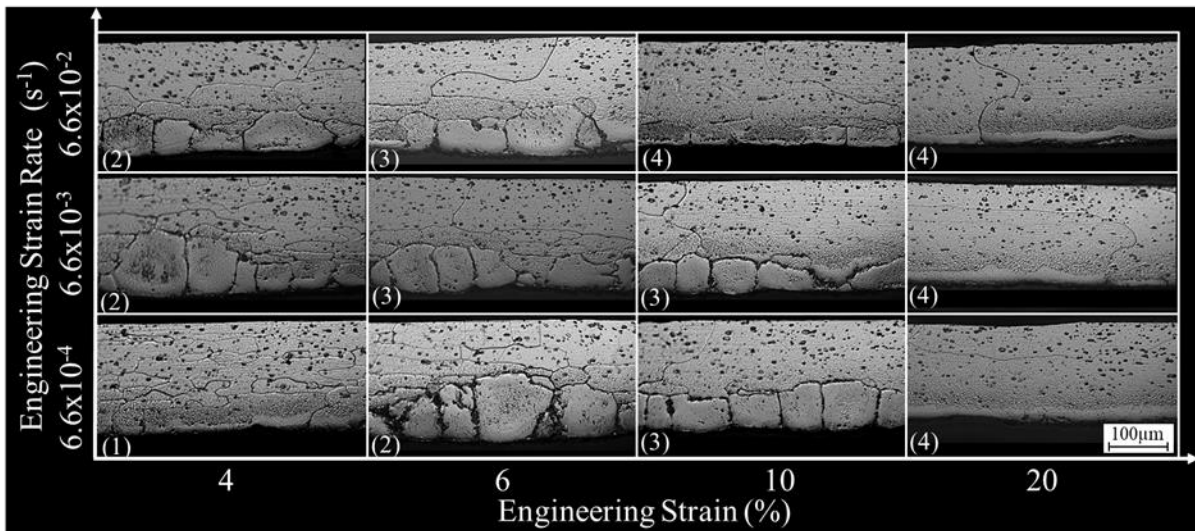
Fig. 7-4 Microstructures after simulated brazing at 600 °C for 3 min, as a function of strain and strain rate, for O temper samples formed at 250 °C. Numbers in parentheses indicate classification of interactions within the sheet.

108

The first class of interactions occurs when the stored deformation energy within the core alloy is too low to trigger either LFM or recrystallization during brazing. An example of this lack of interaction can be seen in Fig. 7-4 for the 250 °C- 6.6×10^{-4} s^{-1}-4 % condition. As the core alloy stored deformation energy increases, but remains below the level required to trigger recrystallization, the driving force for LFM increases. The resultant microstructure is characterized by large grains at the surface protruding into a non-recrystallized core, and was observed when the strain increased (250 °C-6.6×10^{-4} s^{-1}-6 %), the strain rate increased (250 °C-6.6×10^{-3} s^{-1}-4 %), or when the forming temperature was lowered (150 °C-6.6×10^{-4} s^{-1}-4 %). A partially recrystallized core with LFM at the surface (i.e. case 3) was observed with further increases in stored deformation energy, which resulted from greater strain (250 °C-6.6×10^{-4} s^{-1}-10 %), higher strain rate (250 °C-6.6×10^{-3} s^{-1}-6 %), or a lower forming temperature (150 °C-6.6×10^{-4} s^{-1}-6 %). Nylen *et al*. [65] reported similar post-braze microstructures, with narrow bands of non-recrystallized grains directly ahead of the liquid film, but coarse recrystallized grains deeper into the core. The authors proposed that the non-recrystallized grains were due to the inward diffusion of Si from the clad alloy, resulting in the precipitation of fine α-Al(Mn, Fe)Si particles, which stabilized the deformed sub-structure to provide a driving force for the liquid film. Beyond the diffusion zone, the core alloy was able to recrystallize. Similar microstructures were also presented in Chapter 4 for the sagging distance measurements. Finally, a critical level of stored energy is reached, at which point recrystallization *via* SIBM occurs during the brazing cycle. Again, the change in post-braze microstructure was observed with a greater strain (250 °C-6.6×10^{-4} s^{-1}-20 %), higher strain rate (250 °C-6.6×10^{-2} s^{-1}-10 %), or lower forming temperature (150 °C-6.6×10^{-4} s^{-1}-10 %). In all cases, the core alloy grains were coarse and elongated, and a relatively uniform clad residue layer was present at the sheet surface.

The observation in Chapters 3 and 4 that warm forming leads to an extension of strains over which LFM can occur was accurate, but not complete. Fig. 7-3 and Fig. 7-4 indicate that for warm forming, the microstructure evolution as a function of strain will shift when the strain rate changes. For example, it was noted in Chapter 4 that the sagging distance as a function of strain was similar for sheets formed at RT and 150 °C, with nearly equivalent sagging distances above 6 % strain. It can be seen from Fig. 7-3 that the occurrence of LFM and the onset of recrystallization shifted to lower strains as the strain rate increased, becoming very similar to the microstructures of RT formed sheet (Fig. 3-7 and Fig. 4-7). This is not surprising, as it can be

seen from Fig. 7-1 that as the strain rate increased at 150 °C, the stress-strain curve approached the RT curve.

The microstructure evolution shown in Fig. 7-3 and Fig. 7-4 is in agreement with the proposed deformation energy theory dictating the relationship between LFM and recrystallization. However, the findings also indicate some discrepancies in using the flow stress to approximate the stored energy in the core alloy, as was suggested in past chapters. For example, a fully recrystallized core was present in the 250 °C-6.6×10^{-4} s^{-1}- 20 % condition. However, the data in Fig. 7-2 indicate that, due to the lack of strain hardening at 250 °C (n=0.10), the stress at 20 % strain is very similar to the value at 10 % strain, yet the core is only partially recrystallized and suffers from LFM at 10 % strain. Furthermore, the stress at 20 % strain is less than that for the 250 °C-6.6×10^{-2} s^{-1}-4 % condition, but in the latter case the microstructure consists of a non-recrystallized core with LFM at the sheet surface.

One possible explanation for the noted discrepancy is that the driving pressure for LFM depends on the dislocation density in the core (Eq. 8). However, the dislocations can be arranged in dislocation cells after forming to low strains and, due to dynamic recovery, the cells can become well defined sub-grains at higher strains [93]. This is particularly important during warm forming, where dislocation re-mobilization is more feasible [27]. Furthermore, it has been reported that recovery occurs in the order of seconds during annealing of an Al-1% Mn alloy [94], so recovery is expected to occur during heating to the brazing temperature. As it is the stored energy in the core alloy just before the clad alloy melts which determines if LFM occurs, it would perhaps be more suitable to relate the LFM driving pressure to the energy associated with a sub-grain structure, rather than the dislocation density. For example, it may be more useful to relate the likelihood of LFM to the core alloy microhardness of samples heated to 570 °C, as microhardness has shown to be a relatively straightforward way of estimating stored energy [87].

Finally, functional battery cooling plates were successfully brazed from plates formed up to 250 °C, regardless of the predicted increase in the material susceptibility to LFM after warm forming. In fact, brazed joint fillets were successfully formed despite LFM occurring within the joint (Fig. 6-6), due to liquid clad flow to the faying surfaces by wetting and capillary action. No clear differences were observed between brazed plates formed at different temperatures at the component level using digital radiography, or in their ability to be pressurized. Thus, if any

differences exist between plates formed at different temperatures, they are expected to manifest in the corrosion resistance of the cooling plates.

7.1.2. H24 Temper Sheet

Unlike with the O temper sheet, the H24 post-brazed microstructures observed throughout the current work were fairly homogeneous; recrystallized core grains elongated along the sheet rolling direction, and a relatively uniform clad residue layer were observed, regardless of the level of strain or forming temperature. This finding was consistent across the uniaxial test specimens described in Chapter 3, and in the formed plates in Chapters 5 and 6. Due to the homogeneity of the post-braze microstructure, the LDT data in Chapter 3 did not suggest there would be any difference in the brazing performance after warm forming. The predicted brazing performance was shown to be in agreement with actual brazing performance, in terms of the ability to braze leak-free battery cooling plates.

As noted by Han *et al* [11]., to reduce springback of H24 sheet to the level of fully annealed sheet when forming complex components, a higher forming temperature than that used with simple formed geometries was required. For example, a forming temperature of 325 °C was needed to completely reduce the level of springback of the H24 sheet to the level of the O temper sheet for the battery cooling plate geometry, compared to 250 °C for a simple 'U' channel geometry used in a prior study [9]. Since warm forming at 250 °C has been shown to have no adverse impact on the brazing performance of the H24 temper sheet (Chapter 6), H24 temper plates should be formed above 250 °C and brazed. In the cooling plate geometry used in Chapter 6, springback of RT formed H24 sheet was overcome by fixturing, and parts were successfully brazed. However, the full benefits of warm forming are expected to be apparent with the full-scale geometry, since the deviation from flatness will be larger for the same angular deflection. Thus, preliminary brazing trials were performed for plates formed at 325 °C; all forming and brazing parameters and procedures were the same as those used in section 6.2.1. It can be seen from the radiographic images in Fig. 7-5 that brazed fillets were successfully formed around all dimples and around the edges of the channels, although some inconsistencies were noted. The first sample formed at 325 °C had a leak at the fittings, due to insufficient filler metal paste applied to the channel inlet prior to brazing, but no leaks were identified at any other locations. The second sample was found to be leak-free when tested up to 0.28 MPa (40 psi). Thus, forming

at 325 °C without impairing brazing performance appears to be feasible, and should be investigated further.
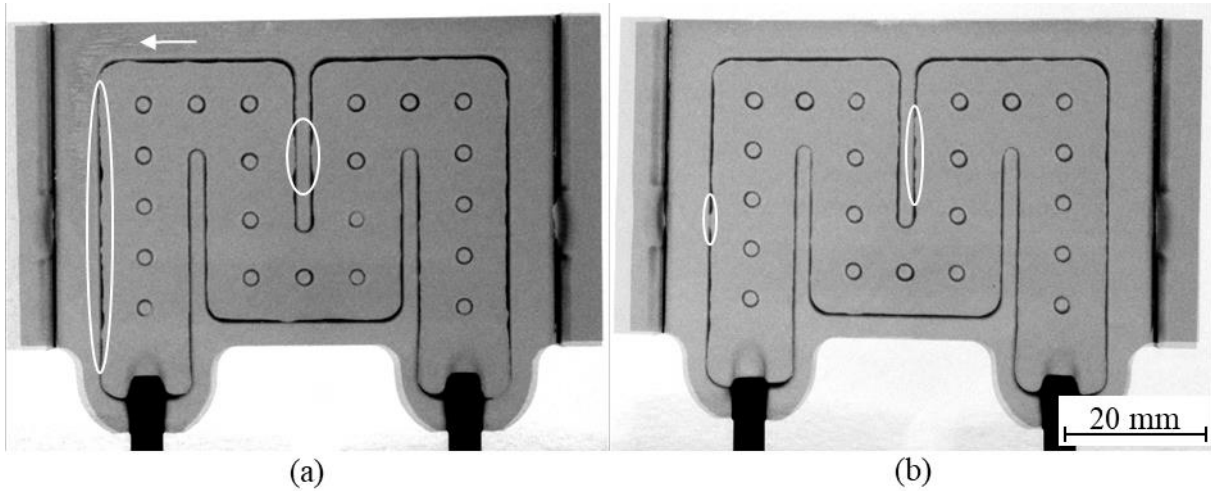
Fig. 7-5 Radiographic images of (a) first and (b) second replicates of brazed battery cooling plates formed from H24 sheet at 325 °C. Missing or inconsistent braze fillet formations are circled, and the arrow indicates irregular clad pooling on the flange.

The similarity in brazing performance of H24 sheets formed at RT and 250 °C does not preclude the possibility of a difference in the sheets' resistance to corrosive failure. Fig. 3-3 revealed that thermal softening of the material occurred during forming at 250 °C, and that the stress-strain curve had a negative slope, due to diffuse necking. These observations have also been reported in prior studies [36]. These results are also reflected by changes in the Nadai model parameters (Table 7-2), where a significant decrease in the strength coefficient occurs when the forming temperature increases to 250 °C, and the strain hardening exponent becomes slightly negative. From the table, the effects are expected to be more exaggerated at 325 °C.

Table 7-2 Variation in the Nadai model parameters as a function of forming temperature, calculated using data from Han [88].

T (°C)	n	B	C (MPa)
25	0.13	0.00	300.76
250	-0.08	0.19	85.17
325	-0.11	0.25	41.11

Despite thermal softening during warm forming, microhardness measurements after forming revealed that the warm formed H24 core alloy hardness was in the same order of magnitude as the RT formed sheet, although the warm formed sheet consistently had a slightly lower hardness (Fig. 3-15). This observation was partially attributed to a slight amount of dynamic recovery during warm forming. According to the recrystallization laws outlined by Burke and Turnbull [58], the recrystallized grain size depends on the level of deformation imparted to the sheet prior to annealing. If the stored energy in the core is reduced during warm forming by dynamic recovery, the recrystallized grain size of the warm formed sheet is expected to be coarser than for the RT formed sheet. While the warm formed H24 sheet appears to have a slightly coarser grain size (e.g. Fig. 3-11 and Fig. 6-6 to Fig. 6-8), these results are anecdotal, as the grain size was not quantified in the current investigation. However, large recrystallized grains are favorable for improved brazeability, as they limit the number of high diffusivity paths for liquid clad penetration (sections 2.4.2 and 2.4.3), while coarse and elongated grains are desirable for corrosion resistance, as this minimizes the total grain boundary area for intergranular attack [2]. Thus, the effect of forming temperature on recrystallized grain size should be quantified. Slight changes in the initial condition of the H24 sheet can impact the post-braze microstructure; a recent investigation has shown that, by increasing the Mg content in the core from 0.1 wt% to 0.5 wt%, the length of the recrystallized grains decreased from 100 µm to 70 µm [21]. If the post-braze recrystallized grain size in warm formed sheet is, in fact, coarser than in RT formed sheet, enhanced corrosion resistance would be expected, which would be a non-obvious benefit of warm forming.

7.2. Corrosion Resistance of Warm Formed Battery Cooling Plates

As noted in section 2.5, the corrosion resistance of the brazing sheet depends on the phases present at the surface in contact with the corrosive environment. In particular, the LFM morphology has been suggested to increase the susceptibility of the core alloy to corrosive attack, as it provides pathways for corrosion propagation into the core alloy along the affected area grain boundaries, and the intermetallic particles which form where the film solidifies can lead to preferential corrosion of the adjacent core [12, 19, 65, 69, 95]. Thus, the increased range of strains over which LFM may be present in a warm formed component could lead to an increased susceptibility to corrosive failure in certain locations, which may not have been a concern with

RT formed components. As corrosive failure of automotive heat exchangers may take years to occur during field service, accelerated corrosion tests are used in alloy and product development. Scott *et al.* [96] outlined several criteria that an accelerated corrosion tests should meet:

1. The test should replicate the corrosion morphology observed after field service.

2. The test environment should be a plausible analogue to the actual service environment.

3. The test sample should reasonably reflect the actual heat exchanger component.

4. The test performance criterion should be suitable to the application and should provide objective and quantifiable results.

5. The test duration should be relatively short.

The ability to replicate the corrosion morphology after field service is the most important criterion, since a test that fails to do so cannot predict in-service corrosion performance. Accelerated corrosion testing of Al brazing sheet and automotive heat exchangers are classified as either external (i.e. air side) or internal (i.e. coolant side) tests. External tests are intended to simulate the material's corrosion resistance to the external environment, such as road salts and exhaust fume by-products, while internal tests are used to investigate the corrosion resistance of the sheet surface in contact with the engine coolant. The Sea water acetic acid test (SWAAT), described in ASTM G85 [97], and the Old Yokohama (OY) River Water Test [98], are the most common external and internal accelerated corrosion tests used for automotive heat exchangers, respectively. However, comparison of accelerated test specimens with components retrieved after field service revealed that the accelerated tests only replicate the corrosion morphology of the most severe environmental conditions [99]. Consequently, a number of alternative standard and self-developed accelerated tests have been used to assess corrosion performance of Al brazing sheets, with varying success. A more thorough history of the development of accelerated corrosion tests is presented elsewhere [19]. As noted by Zhao and Woods [1], the variation in accelerated tests makes the comparison of results across studies difficult, and an industry-wide

standardization is needed. Further complicating the comparison of results is the fact that corrosion results may be performed on either Al brazing sheet coupons or full heat exchanger assemblies, and that the metric used to evaluate corrosion performance can change from one study to the next.

To determine the relative corrosion resistance of the various forming conditions in the current study, the battery cooling plates brazed in Chapter 6 were subjected to an accelerated internal corrosion test. The cooling plates are clearly a suitable representation of the actual heat exchanger components (criterion 3). The test was adapted from ASTM D2570 "Standard test methods for simulated service corrosion testing of engine coolants" [100], and was performed at Dana Canada. Four replicates from each forming condition, for a total of 20 samples, were connected in series, and a neutral salt solution was circulated through the assembly at a flow rate of 0.056 L/min. The solution was of the same composition as the 'corrosive water' outlined in ASTM D2570, which is comprised of deionized water with the addition of sodium salts of chloride (NaCl), sulphate (Na_2SO_4), and bicarbonate ($NaHCO_3$), such that the final solution had a concentration of 100 ppm of each anion; the mass of each salt required to make 1 L of solution is given in Table 7-3. While this test solution does not replicate the service environment of the cooling plates (criterion 2), the solution was used to ensure a relatively short test duration (criterion 5), and because it is the relative, not absolute, corrosion resistance which is of interest here. Furthermore, the corrosive solution was maintained at 65 °C ± 5 °C throughout the test duration, to simultaneously reflect the service environment of battery heat extraction by the coolant (criterion 2), and to accelerate the rate of failure (criterion 5). The total volume of test solution prepared was greater than 10 times the total volume of all samples.

Table 7-3 Mass of the three sodium salts used to make 1 L of corrosive water solution [100].

Salt	Mass (mg)
Sodium Chloride	165
Sodium Sulphate	148
Sodium Bicarbonate	138

The test was performed either until failure of each cooling plate, in the form of a visible leak, or for a duration of 1000 hrs. The battery plates were visually inspected for leaks at a

minimum of once every 24 hrs, with the exception of weekends. The time to sheet perforation is the most meaningful result for the cooling plate application, as perforation during service would lead to coolant leaks and, consequently, loss of heat transfer performance. Furthermore, time to perforation is both quantitative and objective (criterion 4). The location of perforation is also of interest, as consistencies in this metric could elucidate problem areas for specific forming conditions, related to the sheet microstructure at that location, or problem areas across all forming conditions, related to the geometric design of the cooling plates.

Only one sample was reported to fail during the test, after 432 hrs of exposure. The sample was removed from the series connection of samples for analysis, and the remaining plates were re-connected to continue to test. The failed sample was from the O-150 °C forming condition, and the perforation occurred near one of the ribs as seen in Fig. 7-6a. The radiographic image of the plate taken prior to the corrosion test did not indicate any obvious defects at the location of failure (Fig. 7-6b). The sample was sectioned across the width of the plate at the failure location and prepared for metallographic analysis. Fig. 7-7a and b revealed that the failure location was adjacent to the rib, not at the brazed joint. The corrosive attack progressed through the core alloy thickness by mixed intergranular and pitting mechanisms, and also propagated laterally. Obviously, the original microstructure at the initiation point was not available for examination, but it is reasonable to assume the microstructure would be similar at the same location on the opposite side of the channel (Fig. 7-7c). A non-recrystallized core alloy was observed in Fig. 7-7c, but there was no evidence of LFM grains or localized corrosive attack. Instead, the corrosion morphology at this surface consisted of broad and smooth hemispherical pits, which has previously been reported for accelerated corrosion tests using neutral salt solutions [96]. Furthermore, no clear sign of preferential corrosive attack was observed at a location in the same channel cross-section where grains characteristic of LFM were observed (Fig. 7-7d).
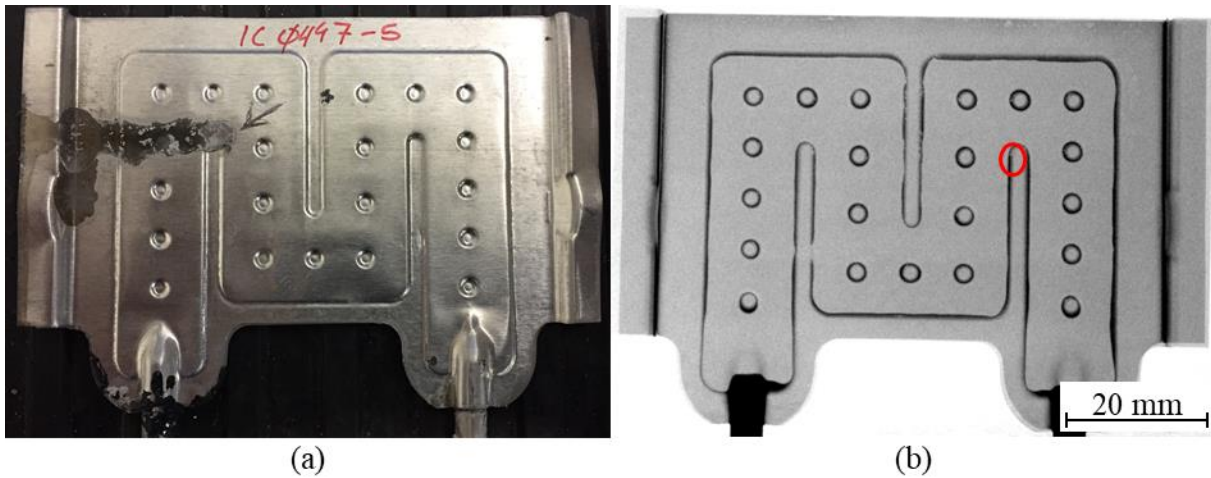
Fig. 7-6 O-150 °C battery cooling plate (a) external surface after 432 hrs of testing, with an arrow indicating the failure location, and (b) radiographic image prior to corrosion testing, with the failure location circled.
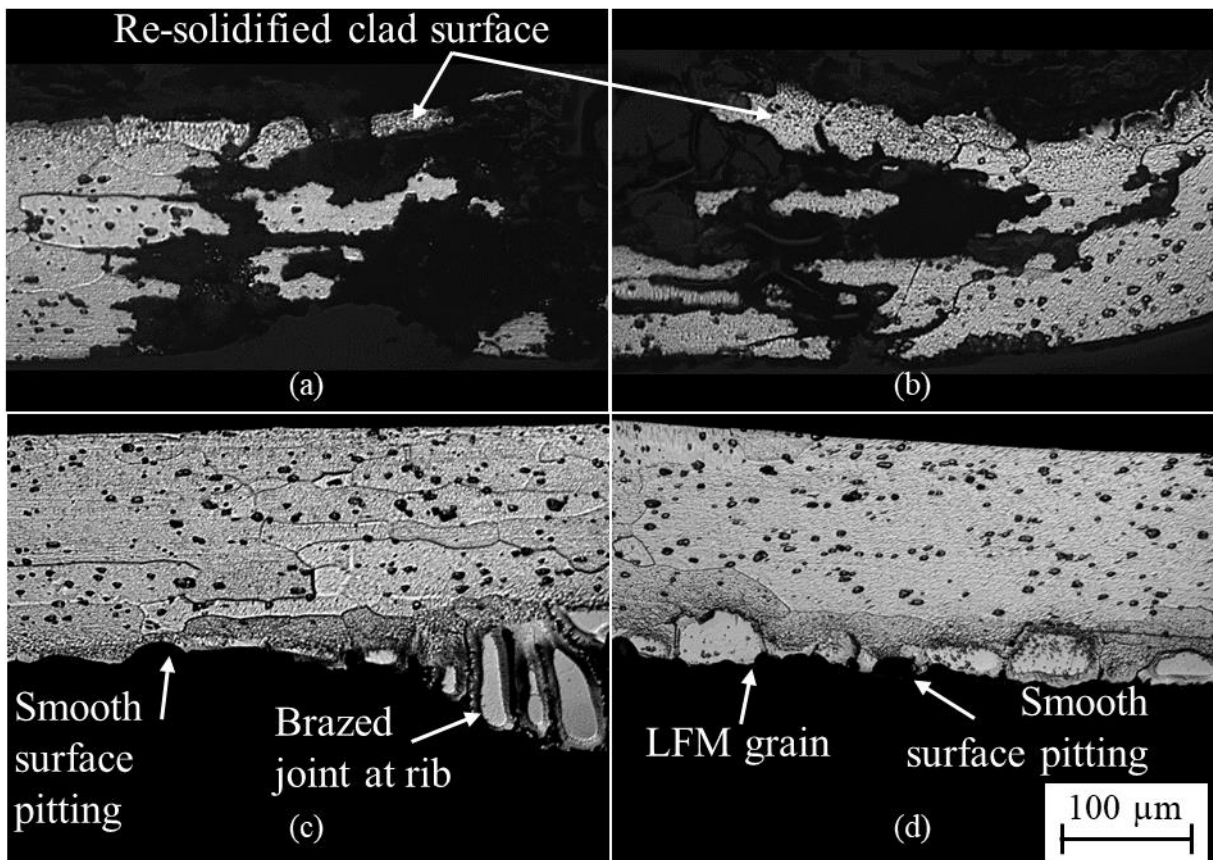

Fig. 7-7 O-150 °C battery cooling plated after 432 hrs of exposure to neutral salt solution. Micrographs in (a) and (b) indicate intergranular corrosion at the failure location, while superficial hemispherical pitting can be seen (c) near the brazed joint at the same location as (a) and (b) but in the other formed plate, and (d) near grains characteristic of LFM.

117

The test was stopped after 1000 hrs, with no additional samples noted to fail during the test. However, visual inspection of the external surface of the battery plate samples after the test revealed the presence of a residue on a number of samples, similar to that observed in Fig. 7-6a, suggesting that leaks were present. Radiographic scans of the remaining 19 plates were performed after visual inspection to non-destructively examine the extent of corrosion within the plate, followed by leak testing of each sample to identify possible failure locations. Radiography and leak tests were performed using the same experimental settings as described in section 6.2.3.

The leak test revealed that a number of samples had failed during the test, which was evidenced by the evolution of air bubbles when the samples were submerged in a pool of water and pressure was applied to the channels. The number of samples for each forming condition with identified leaks are summarized in Table 7-4; the O-150 °C sample which failed at 432 hrs is also included in the table. However, the time to perforation data were not recorded, since the leaks were not detected by visual inspection during the test. Scott *et al.* [96] noted the difficulty in reliably detecting perforations by visual inspection, and attributed this to a gelatinous aluminum hydroxide corrosion product which can block the small perforation. It is possible that the leaks were not detected during the test due to the low flow rate of the solution, but became evident when a pressure of 0.28 MPa (40 psi) was applied to the channels. Clearly, an improved inspection process is necessary to identify leaks when they occur.

Table 7-4 Number of cooling plate samples with identified leaks (out of four replicates).

Forming Temperature	Sheet Temper	
	O	H24
RT	2	2
150 °C	3	-
250 °C	2	1

While the time to perforation data were not recorded during the corrosion test, the perforation locations were determined from the leak test. The locations of identified perforations from all forming conditions are summarized in Fig. 7-8. It should be noted that the number of perforations for a given forming condition in Fig. 7-8 does not necessarily match the number of failed samples reported in Table 7-4, since some samples had multiple perforations. For example,

4 perforations were identified for the H24-RT condition, but only 2 samples from this condition were observed to leak. The perforation locations are overlaid on an image of one half of a brazed battery cooling plate, due to symmetry in the geometry of the plate, to better identify patterns in perforation locations.

Fig. 7-8 Summary of perforation locations from failed samples for all forming conditions. Leak locations are overlaid over an image of one half of a brazed battery cooling plate.

It is apparent from Fig. 7-8 that there is not any clear relationship between the susceptibility to perforation by corrosion and the sheet temper-forming temperature combination. However, it can be seen that the perforations were mainly concentrated around either: (i) the channel inlet and fittings, or (ii) formed features such as ribs and dimples. Since the post-braze microstructures throughout the formed plates were shown, in sections 5.3 and 6.3, to differ for the different forming conditions, the perforations near the formed features are not expected to be the result of preferential attack due to unfavourable microstructures at these locations. Rather, it is believed that these failures could be initiated by the fluid flow pattern in

the channel, inducing a combination of cavitation or impingement, which would degrade the passive film at the sheet surface, and subsequent pitting initiation by the ingress of Cl^- ions from the solution [74]. However, a more detailed study of the fluid flow through the channel needs to be conducted to determine if the fluid pressure at the locations of interest falls below the vapour pressure at 65 °C to cause cavitation.

The radiographic scans for two brazed plates after the corrosion test are presented in Fig. 7-9. The radiographic scans provide valuable insights into the nature of the corrosive attack on the plate, which are not easily obtained by other inspection methods. For example, in Fig. 7-9c and d, the radiographic scans have been magnified around the perforation, which appears brighter than the surrounding region, due to thinning of the material. In both cases, it can be seen that the failure location is not a small, well-defined pin hole, but appears to have laterally spread through the plate. While the leak test could identify the location of the failure, and microstructure analysis could elucidate the corrosion mechanisms and extent of corrosion within a given cross section, neither method could identify the failure location and two dimensional extent of corrosion as easily as the radiographic analysis.
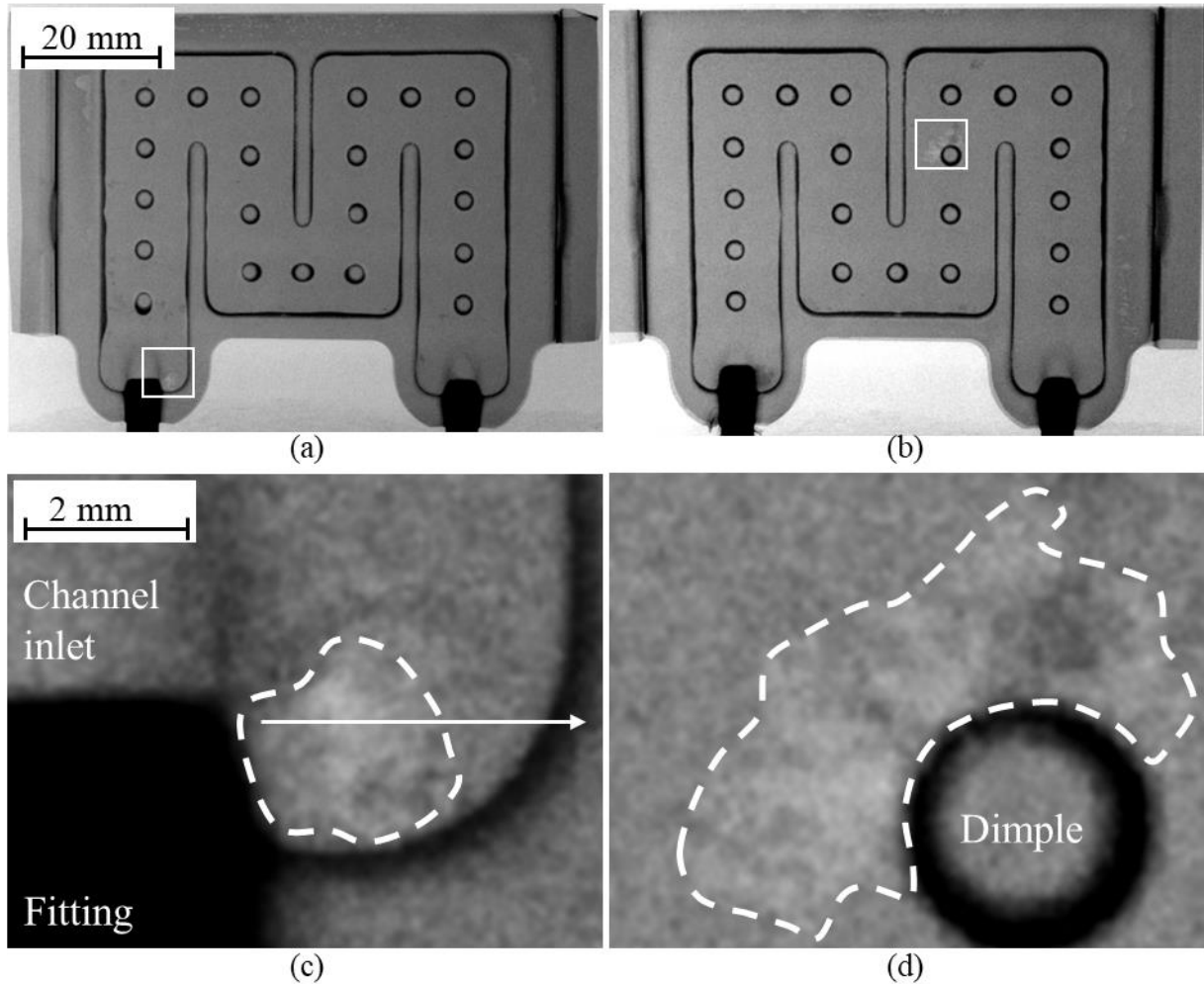
Fig. 7-9 Radiographic images of (a) O-RT and (b) O-150 °C brazed assemblies after the internal corrosion test with the perforation location enclosed by a white square. The perforations are magnified in (c) and (d) for the O-RT and O-150 °C plates, respectively, with the corrosion affected region enclosed by a dashed white line.

Micrographs taken along the arrow through the failure location in Fig. 7-9c are presented in Fig. 7-10. From Fig. 7-10a, it can be seen that corrosion progressed through the sheet thickness along core alloy grain boundaries, beginning at the re-solidified sheet surface and eventually leading to perforation of the sheet, which is the typical corrosion propagation mechanism in Al brazing sheet [1, 2, 3]. Mixed intergranular and pitting mechanisms were found at all perforation locations in the current study, regardless of sheet temper or forming temperature. Microstructures from the same cross section, adjacent to the perforation but closer to the brazed joint at the edge of the channel are presented in Fig. 7-10b and c. It can be seen that even after 1000 hrs of testing,

the corrosion morphology is uniform and consists of shallow hemispherical pits at locations away from the perforation (Fig. 7-10b). Similar to Fig. 7-7d, Fig. 7-10c shows regions where the re-solidified surface is characterized by LFM-like grains that do not appear to be more susceptible to corrosive attack. While past studies had noted that LFM would lead to greater susceptibility to corrosive failure, these studies used more aggressive corrosive environments (i.e. higher Cl^- concentrations and lower pH) than that used in the current investigation [12, 101]. The lack of localized attack at these locations likely explains why no clear relationship between forming condition and susceptibility to corrosive failure was observed. A more comprehensive study is required to elucidate the relationships between processing, microstructure, environment, and corrosion performance.
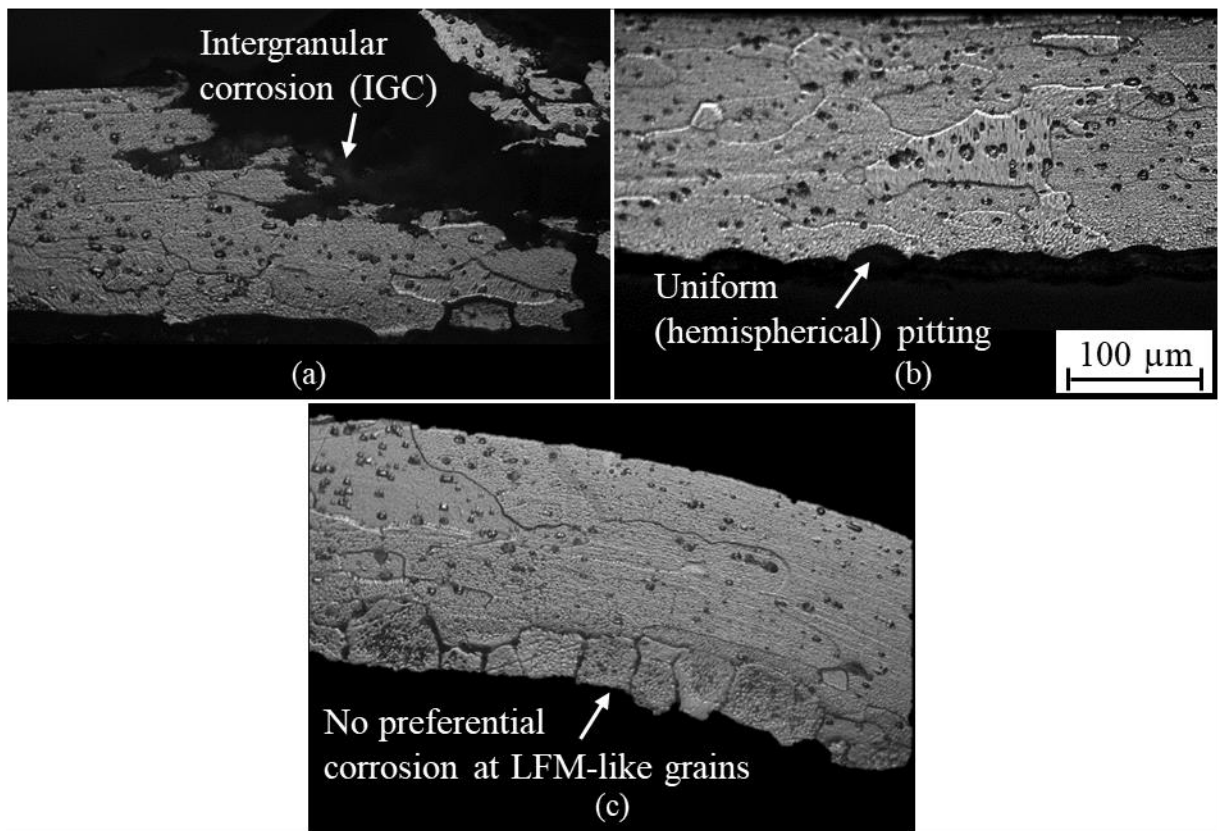

Fig. 7-10 Post-corrosion test microstructure taken along the arrow in Fig. 7-9c for the O-RT cooling plate (a) at the perforation, (b) adjacent to the perforation, and (c) toward the brazed joint at the edge of the channel where LFM-like grains were observed.

122

Finally, the failures which were observed between the channel inlets and the tubular fittings can be understood by examination of the microstructures at the failure locations. An example of a typical microstructure from one such failure location is shown in Fig. 7-11, taken from an O-250 °C brazed sample. As noted in section 6.2.1, a filler metal-flux paste was manually applied between the channel inlet and fitting during assembly of the components prior to brazing. It can be seen in Fig. 7-11 that no filler metal is present at the location where the channel inlet perforated. As a result, a crevice was formed in the assembly at this location where the test solution could become trapped, forming a local concentration cell. After initiation of corrosion, the attack was able to progress through the sheet thickness by mixed intergranular and pitting mechanisms. Therefore, the failures observed at the interface between the fittings and channel inlet are manufacturing defects, and are attributable to the manual application of filler metal paste during assembly. This issue should be eliminated if a more robust method of application is used during high volume production of the plates.
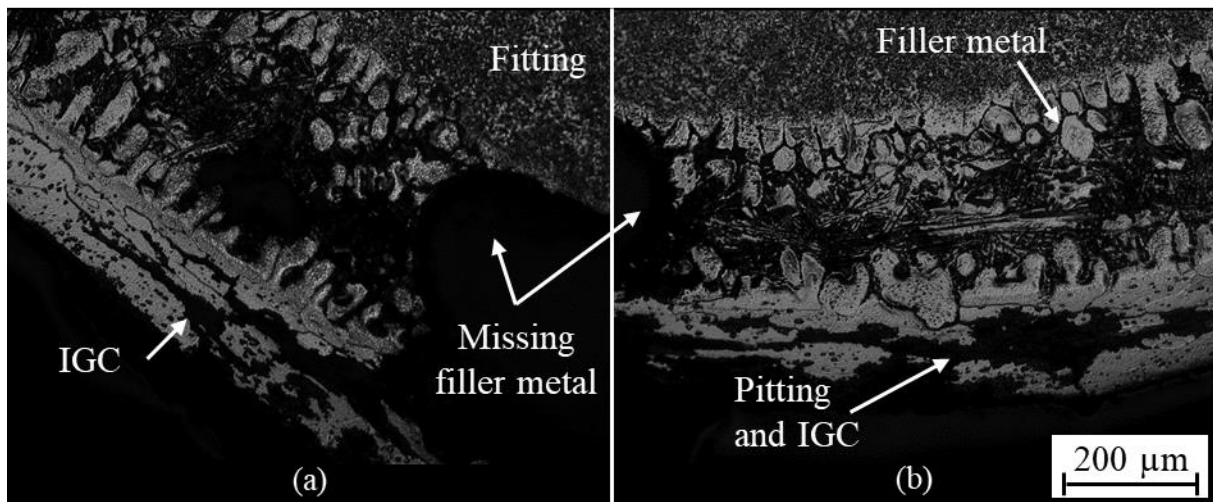

Fig. 7-11 Crevice corrosion at the interface between the fitting and channel inlet, due to insufficient application of filler metal paste prior to brazing the assembly. Image taken from an O-250 °C sample, and is typical for all samples which failed at the fittings.

8.   Summary, Conclusions, and Future Work

8.1.   Summary and Conclusions

Warm forming can be used to expand heat exchanger design possibilities and enable the use of higher strength sheets. However, the relationships between the material initial condition (i.e. sheet temper), forming temperature, and brazeability had not previously been studied, which forms the basis for the objective of the research contained in this thesis. The results presented throughout were the first to investigate this relationship, and provided a number of fundamental and applied discoveries. The following conclusions can be drawn from the current research:

1. The post-braze microstructure of fully annealed Al brazing sheet depends on the applied strain, strain rate, and temperature at which the sheet was formed. When the forming conditions were such that the stored deformation energy in the core alloy was relatively low, the post-braze microstructure was characterized by a non-recrystallized core alloy, with Al-Si solid solution grains at the re-solidified clad surface protruding into the core due to liquid film migration (LFM) during brazing. The core alloy stored energy was increased when a lower forming temperature was used, when the strain rate was increased, or when a greater level of strain was applied. When a critical level of stored energy was reached, recrystallization by strain induced boundary migration (SIBM) occurred in the core alloy during heating to the brazing temperature. SIBM produced coarse and elongated grains in the core alloy, and a clad residue layer of relatively uniform thickness at the original clad surface. Forming above 150 °C extended the range of strains over which LFM occurred during brazing, and increased the threshold level of strain to initiate SIBM. This was particularly true for low strain rates (i.e. $6.6 \times 10^{-4}\,\text{s}^{-1}$), while the regime over which LFM occurred shifted to lower strains when higher strain rates were used. For example, LFM was observed between 6 % and 10 % for samples strained at 250 °C and $6.6 \times 10^{-4}\,\text{s}^{-1}$, but only between 4 % and 6 % when the sheet was strained at 250 °C and $6.6 \times 10^{-2}\,\text{s}^{-1}$. The current results were the first time that the strain rate effect was observed, since all past studies have been concerned with room temperature forming, where the strain rate sensitivity is not significant.

2. For all forming temperatures and levels of strain studied, the H24 temper post-braze microstructure was characterized by recrystallized grains elongated along the sheet rolling direction and a relatively uniform thickness clad residue layer. Due to the cold work imparted during production of the Al brazing sheet to achieve the H24 temper, the core alloy had sufficient stored energy to recrystallize before the clad alloy melting temperature was reached during the brazing cycle. While some dynamic recovery of the H24 sheet was suspected to occur during forming at 250°C, the core alloy microhardness measurements after forming revealed that the hardness was in the same order of magnitude as that of room temperature formed sheets, so recrystallization still occurred.

3. The trends in the clad alloy liquid duration time (LDT) and sheet sagging distance, both as a function of applied strain, were in excellent agreement with the results of past studies for room temperature formed sheet, which indicated their suitability as brazing performance indicators. Furthermore, the post-braze sheet microstructures were strongly correlated with the relationship between these metrics and applied strain. Poor brazing performance was predicted by either a low LDT or a large sagging distance, both of which were consistent with a recovered core alloy and the occurrence of LFM during brazing. On the other hand, good brazing performance was predicted when the LDT was large or the sagging distance was small, and a recrystallized core without penetration by the liquid clad was observed for these forming conditions. Using these metrics, sub-optimal brazing performance was predicted for O temper sheet formed above 150 °C, while no change in brazing performance was expected for H24 temper sheet formed up to 250 °C.

4. The driving force for LFM is the reduction of stored deformation energy. While this driving force was proposed in previous studies, the results in this thesis provide both direct and indirect evidence to support this theory. Transmission electron microscopy images from the interface between the LFM affected area and the remaining core revealed the presence of sub-boundaries in the remaining core, for forming conditions which had a large sagging distance. These conditions included O temper sheet strained to 4 % at room temperature, and strained to 10 % at 250 °C. On the other hand, no sub-

125

structure was found in the core for forming conditions with good predicted brazing performance, such as O temper sheet formed to 6 % strain at room temperature, due to recrystallization. The change in the dependence of the LDT and the sheet sagging distance on applied strain when the forming temperature increased and, consequently, the material flow stress decreased, provided indirect evidence for the stored deformation energy driving force. However, it was also shown that the simple relationship between dislocation density and material flow stress, in conjunction with the proposed LFM driving force, was not adequate to accurately estimate the relative susceptibility to LFM for certain forming conditions.

5. The development of innovative automotive heat exchanger technologies, through the use of warm forming to increase material forming limits and reduce sheet springback, is feasible. Scaled-down battery cooling plates were formed from both O and H24 sheet tempers between room temperature and 250 °C, and were successfully brazed. After calibrating the assembly and brazing process, all plates were shown to be leak-free up to 0.28 MPa (40 psi). No clear difference in the brazing performance was found at the component level for either sheet temper or forming temperature, although brazed fillet consistency for the H24 sheet improved when the forming temperature was increased to 250 °C. The post-braze microstructures for both sheet tempers were comparable to those of the uniaxial specimens at similar levels of strain and strain rate. The brazed battery cooling plates also revealed that the brazing performance predictions for the O temper sheet, using the LDT and sagging distance measurements, were not correct. These metrics were measured on uniaxial test specimens, where the liquid clad was relatively static, unlike in the formed plate where the liquid clad flowed to joint locations by wetting and capillary flow. Thus, sufficient liquid clad was available to form the brazed joints in the formed plates, despite the occurrence of LFM, even within the joint.

6. The preliminary internal corrosion tests provided useful insights at both the macro- and microstructure-scales. No clear relationship was observed between the susceptibility to failure and the forming condition, and the time to perforation was not recorded for all but one failed sample, due to the inability to visually detect leaks during the test. However,

126

the perforation locations from samples of all forming conditions were shown to be concentrated either at the channel inlet and fittings, or around formed features in the coolant channels. Failures near formed features were not in the heavily deformed materials and are believed to be due to the fluid flow pattern through the channel (e.g. causing local pressure drops leading to cavitation), rather than due to microstructure differences. Failures at the fittings were the result of insufficient filler metal application during assembly, leading to the formation of a crevice between the fitting and inlet. At the microstructure level, the test resulted in a fairly uniform hemispherical pitting morphology, characteristic of neutral salt solutions. At the perforation locations, corrosion progressed through the sheet thickness by combined intergranular and pitting mechanisms. Interestingly, re-solidified clad regions characterized by LFM-like grains did not show an increased susceptibility to corrosion as was reported in prior studies. Further work is required to elucidate the relationship between processing, microstructure, environment, and susceptibility to corrosion.

8.2. Recommended Future Work

While numerous important findings were made in conducting this research, they also uncovered a number of additional questions which should be further investigated. In this section, a set of actionable next steps is recommended, in order to further the understanding of the relationship between forming, brazing, and corrosion performance at the fundamental level, and to advance the commercial viability of the warm forming process in heat exchanger production.

1. The competition between LFM and recrystallization during brazing was shown to depend on the processing parameters used during sheet forming. However, it was shown that there were discrepancies in relating the driving pressure derived by Wittebrood [14] to the Al brazing sheet flow stress. Furthermore, the LFM driving pressure was derived in terms of the dislocation density in the core alloy, which is not easily measured. Thus, it is recommended that a more practical model be developed to relate the material susceptibility to LFM, or the propensity of the sheet to recrystallize during brazing, to processing parameters (i.e. forming temperature, strain, and strain rate). For example, the sheet susceptibility to LFM could be quantified by the LDT or sagging distance. The

metric selected could then be plotted as a function of the core alloy hardness after forming, which, in turn, depends on the forming temperature, strain, and strain rate. It should also be noted that while the model may not necessarily describe the actual brazing performance of the sheet in a real assembly, it would allow for a straightforward prediction of the post-braze microstructure and a qualitative assessment of brazeability over a large processing window.

2. A prior study showed that springback of the H24 sheet was not fully reduced after forming at 250 °C, and since springback will be magnified at the full-scale geometry, this could lead to issues during brazing. However, forming at 325 °C was shown to reduce springback to below the level of room temperature formed annealed sheet. The preliminary results of the H24 plates formed at 325 °C (Chapter 7) did not indicate any concerns with the ability to braze plates after forming. Thus, it is recommended that the brazing and corrosion performance of battery cooling plates formed from H24 temper sheet at 325 °C be further investigated, particularly if full-scale plates are to be produced.

3. The H24 temper core alloy recrystallized grain size and aspect ratio as a function of forming temperature should be quantified, because of the reported influence grain size and shape have on minimizing intergranular corrosion. There appeared to be anecdotal evidence in the micrographs in the current work that the grain size of warm formed H24 sheet was slightly coarser than that of sheets formed at room temperature. Moreover, the core alloy microhardness of warm formed H24 sheet was slightly reduced from the room temperature values, so a slightly coarser grain size would be expected. It is known that H24 sheets are processed to produce elongated recrystallized grains, in order to minimize the grain boundary area perpendicular to the clad alloy surface to reduce the sheet susceptibility to intergranular corrosive attack. If the recrystallized grain size or aspect ratio changes with increasing forming temperature, it would be even more apparent for forming at 325 °C. If a coarser recrystallized grain size after forming at elevated temperatures leads to enhanced corrosion resistance of the sheet, this could be an unexpected benefit of warm forming. Thus, as the capabilities of warm forming are

expanded, the effect of forming temperature on the recrystallized grains must be quantified, and the implications for the sheet corrosion resistance should be verified.

4. Warm forming of full-scale battery cooling plates should be performed, because of the increased level of springback. This is particularly important to verify the utility of warm forming to enable the use of higher initial strength sheets through springback reduction. As noted in Chapter 6, the full benefit of warm forming H24 sheet was not realized with the scaled-down battery cooling plates, since the springback experienced after room temperature forming was overcome by fixture design.

5. More extensive corrosion tests must be conducted in order to better understand the relationship between material, processing, and corrosion performance. First, the test used in the current work should be modified to improve detection of leaks. In future tests, the cooling plates should be connected in parallel in order to monitor the differential pressure and fluid flow through each plate, rather than across multiple plates connected in series as in the current test. Furthermore, an improved method to detect leaks during the test is required. For example, the fluid flow through the plates could be stopped during the daily visual inspection and the plates could be attached to pressurized air lines for leak testing, as outlined in section 6.2.3. Alternatively, a die could be added to the test solution to improve *in situ* detection of leaks during visual inspection. Beyond the deficiencies in the test procedure, the inability to conclusively state the relative corrosion performance of the various forming conditions was compounded by the stochastic nature of corrosion and the relatively limited number of available samples. Therefore, the number of replicates should be increased in future studies. Finally, as noted in section 7.2, further studies are required to elucidate the failures around the formed features in the coolant channel, as well as the relationships between microstructure and corrosion. Computational fluid dynamics could be used to understand the local changes in fluid flow through the channels, and to determine if the conditions necessary for cavitation or impingement are possible. The relationship between microstructure, environment, and corrosion could be investigated using a simple 2^2 factorial design of experiment. The forming conditions would produce different post-braze microstructures (e.g. O-RT-4 %

and O-RT-10 %) and the environments would differ in severity (e.g. ASTM D2570 corrosive water and ASTM G85 SWAAT solution). Electrochemical measurements (e.g. corrosion current density, corrosion potential, and pitting potential) on the post-brazed test coupons in each environment could then be used to assess the susceptibility to corrosion.

Letter of Copyright Permission

The necessary copyright permissions have been obtained to re-use published materials. This section provides the licences and permissions for Chapters 3, 4, and 5 from the publishers. Furthermore, as Chapters 3 and 4 were conducted in collaboration with CanmetMATERIALS, the original publications are Crown copyright, so additional permissions are given here. At the time of this writing, Chapter 6 has not been submitted for publication, so no permissions are given. In addition, copyright permissions were obtained for figures and tables originally published by other authors. These include Table 2-1 and Table 2-2, and Fig. 2-1 to Fig. 2-19.

Springer Nature Licence for Chapter 3

SPRINGER NATURE LICENSE
TERMS AND CONDITIONS
May 09, 2018

<501
yes
Effect of warm forming on brazing and corrosion performance of aluminum brazing sheet
Michael J Benoit
University of Waterloo
Aug 2018
Mr. Michael Benoit
9 Leila St

St. Thomas, ON N5R 2A5
Canada
Attn: Mr. Michael Benoit
Invoice
Mr. Michael Benoit
9 Leila St

St. Thomas, ON N5R 2A5
Canada
Attn: Mr. Michael Benoit
0.00 CAD

132

5. Where **'reuse in a dissertation/thesis'** has been selected the following terms apply: Print rights for up to 100 copies, electronic rights for use only on a personal website or institutional repository as defined by the Sherpa guideline (www.sherpa.ac.uk/romeo/).

6. Permission granted for books and journals is granted for the lifetime of the first edition and does not apply to second and subsequent editions (except where the first edition permission was granted free of charge or for signatories to the STM Permissions Guidelines http://www.stm-assoc.org/copyright-legal-affairs/permissions/permissions-guidelines/), and does not apply for editions in other languages unless additional translation rights have been granted separately in the licence.

7. Rights for additional components such as custom editions and derivatives require additional permission and may be subject to an additional fee. Please apply to Journalpermissions@springernature.com/bookpermissions@springernature.com for these rights.

8. The Licensor's permission must be acknowledged next to the licensed material in print. In electronic form, this acknowledgement must be visible at the same time as the figures/tables/illustrations or abstract, and must be hyperlinked to the journal/book's homepage. Our required acknowledgement format is in the Appendix below.

9. Use of the material for incidental promotional use, minor editing privileges (this does not include cropping, adapting, omitting material or any other changes that affect the meaning, intention or moral rights of the author) and copies for the disabled are permitted under this licence.

10. Minor adaptations of single figures (changes of format, colour and style) do not require the Licensor's approval. However, the adaptation should be credited as shown in Appendix below.

Elsevier Licence for Chapter 4

Crown Permission for Chapter 4

> You replied to this message on 2018-07-12 11:36 AM.
> This message was sent with High importance.

Dear Michael,

Assuming that:
- you have authorization from both publishers, Springer and Elsevier, for using their publications rights,

---

FOR CHAPTER 3
- **Liquid Film Migration in Warm Formed Aluminum Brazing Sheet**
  Metallurgical and Materials Transactions A;
  Volume 48, Issue 10, October 2017, Pages 4645-4654
  Published by Springer

FOR CHAPTER 4
- **Sagging Resistance of Warm Formed Aluminum Brazing Sheet**
  Journal of Materials Processing Technology
  Volume 254, April 2018, Pages 353-360
  Published by Elsevier

And considering that :
- You are not altering the work done by Haiou or Babak;
- You are adding the footnotes in your thesis acknowledging the original works
- Haiou Jin also agreed with your request of using the information in the papers mentioned above,

Then NRCan grants you permission to use the information included in these publications in your thesis results.
We wish you success in your thesis.
Best regards,
Maria

Permission for Chapter 5

As per Janice, I concur just make sure you cite properly that the content was first published in the ICAA16 Proceedings

Article originally published in 16th International Conference of Aluminum Alloys Proceedings (ICAA16) 2018., ISBN 978-1-926872-41-4 Reprinted with permission.

Brigitte Farah

Brigitte Farah
Manager, Operations
Gestionnaire, opérations
The Metallurgy and Materials Society of CIM
La Société de la métallurgie et des matériaux de l'ICM
1250- 3500 de Maisonneuve Blvd. W., Westmount QC H3Z 3C1
www.metsoc.org /Ph: 514-939-2710 ext. 1329 Cell: 514-244-2773

From: Burke, Janice
Sent: May-15-18 8:16 AM
To: Michael Benoit <mjlbenoi@uwaterloo.ca>; Farah, Brigitte <bfarah@cim.org>
Subject: Re: Copyright for ICAA papers

No worries Michael. You can do what you wish with it.

With warm regards,

Ms Janice M. Burke
Editorial Coordinator, CIM Journal
Editor, Global Mining Standards and Guidelines Group
Technical Program Coordinator. ICAA16 and RFG2018

Permission for Table 2-1 and Fig. 2-18

Confirmation Number: 11740208
Order Date: 08/17/2018
Customer Information

Customer: Michael Benoit
Account Number: 3001284660
Organization: Michael Benoit
Email: mjlbenoi@uwaterloo.ca
Phone: +1 (519) 851-8087
Payment Method: Invoice

Order Details

Advances in brazing : Science, technology and applications

- **Order detail ID:**71487991
- **ISBN:**9780857094230
- **Publication Type:**Book
- **Publisher:**Woodhead Publishing
- **Author/Editor:**Sekulić, Dušan P.
- **Permission Status:** ✅ **Granted**

- **Permission type:**Republish or display content
- **Type of use:**Thesis/Dissertation
-

Order License Id: 4411390014023

Requestor type	Academic institution
Format	Print, Electronic
Portion	chart/graph/table/figure
Number of charts/graphs/tables/figures	2
The requesting person/organization	Michael Benoit
Title or numeric reference of the portion(s)	Table 10.2, Fig. 10.26
Title of the article or chapter the portion is from	Chapter 10
Editor of portion(s)	D. Sekulic
Author of portion(s)	H. Zhao, R. Woods
Volume of serial or monograph	N/A
Issue, if republishing an article from a serial	N/A
Page range of portion	286-313
Publication date of portion	2013
Rights for	Main product
Duration of use	Life of current edition
Creation of copies for the disabled	no
With minor editing privileges	no
For distribution to	Worldwide
In the following language(s)	Original language of publication
With incidental promotional use	no
Lifetime unit quantity of new product	Up to 499
Title	Effect of Forming Temperature and Sheet Temper on the Brazing Characteristics of Aluminum Alloy Sheet
Instructor name	n/a
Institution name	University of Waterloo
Expected presentation date	Aug 2018

Note: This item was invoiced separately through our **RightsLink service.** More info$ 0.00

Permission for Table 2-2 and Fig. 2-5

REQUEST FOR PERMISSION TO REPRINT INFORMATION COPYRIGHTED BY THE AMERICAN WELDING SOCIETY (AWS)

Date: Aug. 14, 2018

We request permission to (✓ reproduce), (quote), or (✓ adapt*) the following information copyrighted by the American Welding Society:

Title: Brazing Handbook 4th Edition

Author(s): AWS Committee on Brazing and Soldering

Date: 1991

Tables/figures: Fig 1.3(A), pg.4 - reproduce, Table 3.4, pg. 55 (adapt)

Text selections (specify by page number and paragraph): _____

* With respect to adapted material, we request permission to change the source material as follows (attach PDF file or photocopy, if available): I have reduced the number of alloys listed in Table 3.4, due to the context of the section in which the material is presented. I have attached the adapted version of the table.

This material is to be used in the (book), (magazine) , (✓ other [please specify PhD thesis]) titled Effect of Forming Temperature and Sheet Temper on the Brazing Characteristics of Aluminum Alloy Sheet , which is scheduled for release in the year 20 18 by (publisher) the University of Waterloo .

Please return to:

Permission to use the above-requested material is hereby granted on the conditions specified below:

1. A complete list of items to be referenced, reproduced, or adapted is submitted above.

2. Full credit is given to the source using the following credit line(s):

AWS XXXX:YYYY, Figure/Table/Form ZZZZ, reproduced with permission from the American Welding Society(AWS), Miami, FL

where: XXXX = standard number e.g. A5.18/A5.18M   YYYY = year of publication e.g. 2005   ZZZZ = number e.g. Table 4.7

3. Two copies of the published document are sent to Director, Standards Development Dept, American Welding Society, 8669 NW 36 ST, #130, Miami, Florida 33166.

Date: 8/14/2018

Approved by: Peter Portela

Printed name: Peter Portela

*** Use of AWS copyrighted material beyond the scope of the permission granted may result in all permissions to use AWS material being revoked. Copyright abuse will be pursued pursuant to US copyright laws.***

Technical Services/Request for Permission to Reprint Information Copyrighted by AWS/04/01/2015

Permission for Fig. 2-1

Requestor Location	Mr. Michael Benoit
	9 Leila St
	St. Thomas, ON N5R 2A5
	Canada
	Attn: Mr. Michael Benoit
Publisher Tax ID	GB 494 6272 12
Total	0.00 USD
Terms and Conditions	

Permission for Fig. 2-2 and Fig. 2-3

License Number	4398431384256
License date	Jul 29, 2018
Licensed Content Publisher	Springer Nature
Licensed Content Publication	International Journal of Material Forming
Licensed Content Title	Formability improvement with independent die and punch temperature control
Licensed Content Author	Reza Bagheriasl, Kamyar Ghavam, Michael J. Worswick
Licensed Content Date	Jan 1, 2012
Licensed Content Volume	7
Licensed Content Issue	2
Type of Use	Thesis/Dissertation
Requestor type	academic/university or research institute
Format	print and electronic
Portion	figures/tables/illustrations
Number of figures/tables/illustrations	2
Will you be translating?	no
Circulation/distribution	<501

Author of this Springer Nature content	no
Title	Effect of Forming Temperature and Sheet Temper on the Brazing Characteristics of Aluminum Alloy Sheet
Instructor name	n/a
Institution name	University of Waterloo
Expected presentation date	Aug 2018
Portions	Figure 3, Fig. 7
Requestor Location	Mr. Michael Benoit 9 Leila St
	St. Thomas, ON N5R 2A5 Canada Attn: Mr. Michael Benoit
Billing Type	Invoice
Billing Address	Mr. Michael Benoit 9 Leila St
	St. Thomas, ON N5R 2A5 Canada Attn: Mr. Michael Benoit
Total	0.00 USD

Terms and Conditions

Permission for Fig. 2-4

Tue 2018-08-21 4:07 PM
Rohit Verma
Re: Copyright permission to re-use Fig. 40 in your thesis

To   Michael Benoit

ⓘ You replied to this message on 2018-08-21 4:36 PM.

Hi Mike,

Please go ahead. Thanks.

Regards,
Rohit

Sent from my iPhone

On Aug 21, 2018, at 3:43 PM, Michael Benoit <mjlbenoit@uwaterloo.ca> wrote:

Hi Rohit,
I hope you are doing well since the last time I saw you.
I am contacting you today to seek your permission to re-produce Fig. 40 from you thesis in the literature review of my thesis.
This figure displays the decrease in springback observed after forming at elevated temperatures.
Please let me know if there are any questions or concerns.
Kindest regards,
Michael Benoit

Permission for Fig. 2-6

Confirmation Number: 11740205
Order Date: 08/17/2018
Customer Information
Customer: Michael Benoit
Account Number: 3001284660
Organization: Michael Benoit
Email: mjlbenoi@uwaterloo.ca
Phone: +1 (519) 851-8087
Payment Method: Invoice

Order Details

Advances in brazing : Science, technology and applications

- **Order detail ID:**71485920
- **ISBN:**9780857094230
- **Publication Type:**Book
- **Publisher:**Woodhead Publishing
- **Author/Editor:**Sekulić, Dušan P.
- **Permission Status:** ✅ **Granted**

- **Permission type:**Republish or display content
- **Type of use:**Thesis/Dissertation
-

Order License Id:	4411381060143
Requestor type	Academic institution
Format	Print, Electronic
Portion	chart/graph/table/figure
Number of charts/graphs/tables/figures	1
The requesting person/organization	Michael Benoit
Title or numeric reference of the portion(s)	Fig. 1.12
Title of the article or chapter the portion is from	Chapter 1
Editor of portion(s)	D. Sekulic
Author of portion(s)	N. Eustathopoulos, F. Hodaj, O. Kozlova
Volume of serial or monograph	N/A
Issue, if republishing an article from a serial	N/A
Page range of portion	17
Publication date of portion	2013
Rights for	Main product
Duration of use	Life of current edition
Creation of copies for the disabled	no
With minor editing privileges	no
For distribution to	Worldwide
In the following language(s)	Original language of publication
With incidental promotional use	no

Lifetime unit quantity of new product	Up to 499
Title	Effect of Forming Temperature and Sheet Temper on the Brazing Characteristics of Aluminum Alloy Sheet
Instructor name	n/a
Institution name	University of Waterloo
Expected presentation date	Aug 2018

Note: This item was invoiced separately through our **RightsLink service.** More info**$ 0.00**

Permission for Fig. 2-7

Are you the author of this Elsevier article?	No
Will you be translating?	No
Original figure numbers	Fig. 4, Fig. 7
Title of your thesis/dissertation	Effect of Forming Temperature and Sheet Temper on the Brazing Characteristics of Aluminum Alloy Sheet
Publisher of new work	University of Waterloo
Expected completion date	Aug 2018
Estimated size (number of pages)	200
Requestor Location	Mr. Michael Benoit 9 Leila St St. Thomas, ON N5R 2A5 Canada Attn: Mr. Michael Benoit
Publisher Tax ID	GB 494 6272 12
Total	0.00 USD
Terms and Conditions	

Permission for Fig. 2-8

SPRINGER NATURE LICENSE
TERMS AND CONDITIONS

Jul 29, 2018

This Agreement between Mr. Michael Benoit ("You") and Springer Nature ("Springer Nature") consists of your license details and the terms and conditions provided by Springer Nature and Copyright Clearance Center.

License Number	4398520832753
License date	Jul 29, 2018
Licensed Content Publisher	Springer Nature
Licensed Content Publication	Bulletin of alloy phase diagrams
Licensed Content Title	The Al-Si (Aluminum-Silicon) system
Licensed Content Author	J. L. Murray, A. J. McAlister
Licensed Content Date	Jan 1, 1984
Licensed Content Volume	5
Licensed Content Issue	1

Type of Use	Thesis/Dissertation
Requestor type	academic/university or research institute
Format	print and electronic
Portion	figures/tables/illustrations
Number of figures/tables/illustrations	1
Will you be translating?	no
Circulation/distribution	<501
Author of this Springer Nature content	no
Title	Effect of Forming Temperature and Sheet Temper on the Brazing Characteristics of Aluminum Alloy Sheet
Instructor name	n/a
Institution name	University of Waterloo
Expected presentation date	Aug 2018
Portions	Fig. 2
Requestor Location	Mr. Michael Benoit 9 Leila St St. Thomas, ON N5R 2A5 Canada Attn: Mr. Michael Benoit
Billing Type	Invoice
Billing Address	Mr. Michael Benoit 9 Leila St St. Thomas, ON N5R 2A5 Canada Attn: Mr. Michael Benoit
Total	0.00 USD
Terms and Conditions	

Permission for Fig. 2-9 and Fig. 2-10

REQUEST FOR PERMISSION TO REPRINT INFORMATION COPYRIGHTED
BY THE AMERICAN WELDING SOCIETY (AWS)

Date: Aug. 14, 2018

We request permission to (✔ reproduce), (quote), or (adapt*) the following information copyrighted by the American Welding Society:

Title: Diffusion of Silicon in Aluminum Brazing Sheet (Welding Journal Research Supplement pp.202-209)

Author(s): J. R. Terrill

Date: May 1966

Tables/figures: Fig. 2 and Fig. 4

Text selections (specify by page number and paragraph): _____

* With respect to adapted material, we request permission to change the source material as follows (attach PDF file or photocopy, if available): _____

This material is to be used in the (book), (magazine) , (✔ other [please specify PhD thesis]) titled _Effect of Forming Temperature and Sheet Temper on the Brazing Characteristics of Aluminum Alloy Sheet_ , which is scheduled for release in the year 20 18 by (publisher) the University of Waterloo .

Please return to:

Permission to use the above-requested material is hereby granted on the conditions specified below:

1. A complete list of items to be referenced, reproduced, or adapted is submitted above.

2. Full credit is given to the source using the following credit line(s):

   Welding Journal (month, year) © American Welding Society

3. Two copies of the published document are sent to Director, Standards Development Dept, American Welding Society, 8669 NW 36 ST, #130, Miami, Florida 33166.

Date: 8/15/18   Approved by: Mary Ruth Johnsen

          Printed name: Mary Ruth Johnsen

*** Use of AWS copyrighted material beyond the scope of the permission granted may result in all permissions to use AWS material being revoked. Copyright abuse will be pursued pursuant to US copyright laws.***

Technical Services/Request for Permission to Reprint Information Copyrighted by AWS/04/01/2015

Permission for Fig. 2-11

This Agreement between Mr. Michael Benoit ("You") and Elsevier ("Elsevier") consists of your license details and the terms and conditions provided by Elsevier and Copyright Clearance Center.

License Number	4404450324552
License date	Aug 08, 2018
Licensed Content Publisher	Elsevier
Licensed Content Publication	Scripta Materialia
Licensed Content Title	A re-evaluation of the mechanism of SIBM
Licensed Content Author	Peter Bate,Bevis Hutchinson
Licensed Content Date	Jan 15, 1997
Licensed Content Volume	36
Licensed Content Issue	2
Licensed Content Pages	4
Start Page	195
End Page	198
Type of Use	reuse in a thesis/dissertation
Portion	figures/tables/illustrations
Number of figures/tables/illustrations	1
Format	both print and electronic
Are you the author of this Elsevier article?	No
Will you be translating?	No
Original figure numbers	Fig. 1
Title of your thesis/dissertation	Effect of Forming Temperature and Sheet Temper on the Brazing Characteristics of Aluminum Alloy Sheet
Publisher of new work	University of Waterloo
Expected completion date	Aug 2018
Estimated size (number of pages)	200
Requestor Location	Mr. Michael Benoit 9 Leila St

Publisher Tax ID	GB 494 6272 12
Total	0.00 USD
Terms and Conditions	

Permission for Fig. 2-12

Confirmation Number: 11734451
Order Date: 07/29/2018
Customer Information

Customer: Michael Benoit
Account Number: 3001284660
Organization: Michael Benoit
Email: mjlbenoi@uwaterloo.ca
Phone: +1 (519) 851-8087
Payment Method: Invoice

Order Details

Materials science forum

- **Order detail ID:**71343431
- **ISSN:**1662-9752
- **Publication Type:**Monographic Series
- **Volume:**
- **Issue:**
- **Start page:**
- **Publisher:**Trans Tech Publications
- **Permission Status:** ✅ **Granted**

- **Permission type:**Republish or display content
- **Type of use:**Thesis/Dissertation
-

Order License Id:	4398530570131
Requestor type	Academic institution
Format	Print, Electronic
Portion	image/photo
Number of images/photos requested	1
The requesting person/organization	Michael Benoit
Title or numeric reference of the portion(s)	Figure 3
Title of the article or chapter the portion is from	Liquid Film Migration in Aluminium Brazing Sheet?
Editor of portion(s)	W.J. Poole, M.A. Wells and D.J. Lloyd

Author of portion(s)	A. Wittebrood, S. Desikan, R. Boom, Laurens Katgerman
Volume of serial or monograph	519-521
Page range of portion	1151-1156
Publication date of portion	July 2006
Rights for	Main product
Duration of use	Life of current edition
Creation of copies for the disabled	no
With minor editing privileges	no
For distribution to	Worldwide
In the following language(s)	Original language of publication
With incidental promotional use	no
Lifetime unit quantity of new product	Up to 499
Title	Effect of Forming Temperature and Sheet Temper on the Brazing Characteristics of Aluminum Alloy Sheet
Instructor name	n/a
Institution name	University of Waterloo
Expected presentation date	Aug 2018

Note: This item was invoiced separately through our **RightsLink service.** More info **$ 0.00**

Permission for Fig. 2-13

Licensed Content Date	Jan 1, 2001
Licensed Content Volume	20
Licensed Content Issue	3
Type of Use	Thesis/Dissertation
Requestor type	academic/university or research institute
Format	print and electronic
Portion	figures/tables/illustrations
Number of figures/tables/illustrations	1
Will you be translating?	no
Circulation/distribution	<501
Author of this Springer Nature content	no
Title	Effect of Forming Temperature and Sheet Temper on the Brazing Characteristics of Aluminum Alloy Sheet
Instructor name	n/a
Institution name	University of Waterloo
Expected presentation date	Aug 2018
Portions	Fig. 6
Requestor Location	Mr. Michael Benoit 9 Leila St St. Thomas, ON N5R 2A5 Canada Attn: Mr. Michael Benoit
Billing Type	Invoice
Billing Address	Mr. Michael Benoit 9 Leila St St. Thomas, ON N5R 2A5 Canada Attn: Mr. Michael Benoit
Total	0.00 USD
Terms and Conditions	

Permission for Fig. 2-14, Fig. 2-15, and Fig. 2-16

Permission for Fig. 2-17

150

Licensed Content Author	F. Norouzi Afshar,A.M. Glenn,J.H.W. de Wit,H. Terryn,J.M.C. Mol
Licensed Content Date	Aug 1, 2013
Licensed Content Volume	104
Licensed Content Issue	n/a
Licensed Content Pages	16
Start Page	48
End Page	63
Type of Use	reuse in a thesis/dissertation
Intended publisher of new work	other
Portion	figures/tables/illustrations
Number of figures/tables/illustrations	1
Format	both print and electronic
Are you the author of this Elsevier article?	No
Will you be translating?	No
Original figure numbers	Fig. 16
Title of your thesis/dissertation	Effect of Forming Temperature and Sheet Temper on the Brazing Characteristics of Aluminum Alloy Sheet
Publisher of new work	University of Waterloo
Expected completion date	Aug 2018
Estimated size (number of pages)	200
Requestor Location	Mr. Michael Benoit 9 Leila St St. Thomas, ON N5R 2A5 Canada Attn: Mr. Michael Benoit
Publisher Tax ID	GB 494 6272 12
Total	0.00 USD
Terms and Conditions	

Permission for Fig. 2-19

License Number	4398440502222
License date	Jul 29, 2018
Licensed Content Publisher	Springer Nature
Licensed Content Publication	Metallurgical and Materials Transactions A
Licensed Content Title	Microstructural control in an aluminum core alloy for brazing sheet applications
Licensed Content Author	G. J. Marshall, R. K. Bolingbroke, A. Gray
Licensed Content Date	Jan 1, 1993
Licensed Content Volume	24
Licensed Content Issue	9
Type of Use	Thesis/Dissertation
Requestor type	academic/university or research institute
Format	print and electronic
Portion	figures/tables/illustrations
Number of figures/tables/illustrations	1
Will you be translating?	no
Circulation/distribution	<501
Author of this Springer Nature content	no
Title	Effect of Forming Temperature and Sheet Temper on the Brazing Characteristics of Aluminum Alloy Sheet
Instructor name	n/a
Institution name	University of Waterloo
Expected presentation date	Aug 2018
Portions	Fig. 11
Requestor Location	Mr. Michael Benoit 9 Leila St

	St. Thomas, ON N5R 2A5 Canada Attn: Mr. Michael Benoit
Billing Type	Invoice
Billing Address	Mr. Michael Benoit 9 Leila St St. Thomas, ON N5R 2A5 Canada Attn: Mr. Michael Benoit
Total	0.00 USD
Terms and Conditions	

References

[1] H. Zhao and R. Woods, "Controlled atmosphere brazing of aluminum," in *Advances in Brazing: Science, Technology and Applications*, D. P. Sekulic, Ed., Oxford, Woodhead Publishing, 2013, pp. 280-318.

[2] W. S. Miller, L. Zhuang, J. Bottema, A. J. Wittebrood, P. De Smet, A. Haszler and A. Vieregge, "Recent development in aluminium alloys for the automotive industry," *Materials Science and Engineering: A,* vol. 280, no. 1, pp. 37-49, 2000.

[3] G. J. Marshall, R. K. Bolingbroke and A. Gray, "Microstructural control in an aluminum core alloy for brazing sheet applications," *Metallurgical Transactions A,* vol. 24, no. 9, pp. 1935-1942, 1993.

[4] L. Pekarsky and D. Fabricatore, "Electric vehicle thermal management and filtration system". United States Patent US20140216693 A1, 7 August 2014.

[5] P. J. Bolt, N. A. P. M. Lamboo and P. J. C. M. Rozier, "Feasibility of warm drawing of aluminium products," *Journal of Materials Processing Technology,* vol. 115, no. 1, pp. 118-121, 2001.

[6] S. Kalpakjian and S. Schmid, Manufacturing processes for engineering materials, Upper Saddle River, NJ: Prentice Hall, 2003.

[7] R. Bagheriasl, K. Ghavam and M. J. Worswick, "Formability improvement with independent die and punch temperature control," *International Journal of Material Forming,* vol. 7, no. 2, pp. 139-154, 2014.

[8] R. Bagheriasl and M. J. Worswick, "Formability of AA3003 brazing sheet at elevated temperatures: limiting dome height experiments and determination of forming limit diagrams," *International Journal of Material Forming,* vol. 8, no. 2, pp. 229-244, 2015.

[9] R. Verma, S. Kurukuri, M. J. Worswick and S. Winkler, "Effect of warm forming on springback of aluminum alloy sheet," in *International Deep Drawing Research Group (IDDRG)*, Paris, 2014.

[10] R. Verma, R. George, S. Kurukuri, M. Worswick and S. Winkler, "Warm forming process study for reducing springback in aluminum alloy brazing sheets," in *International Deep Drawing Research Group (IDDRG)*, Shanghai, 2015.

[11] K. B. Han, R. George, S. Kurukuri, M. J. Worswick and S. Winkler, "Springback of aluminum alloy brazing sheet in warm forming," in *ESAFORM*, Dublin, 2017.

[12] R. Woods, "Liquid film migration during aluminum brazing," in *Vehicle Thermal Management Systems (VTMS) 3*, Indianapolis, 1997.

[13] Y. Isobe, K. Takeuchi, M. Tanaka, M. Mori, S. Yamauchi and K. Namba, "Development of a corrosion resistant brazing sheet for drawn cup type evaporators part 2: application to evaporator," SAE International, Warrendale, PA, 1993.

[14] A. Wittebrood, "Microstructural changes in brazing sheet due to solid-liquid interaction," Delft University of Technology, Delft, 2009.

[15] D. J. Schmatz, "Grain boundary penetration during brazing of aluminum," *Welding Journal Research Supplement,* no. 10, pp. 267-271, 1983.

[16] M. Nylen, U. Gustavsson, B. Hutchinson and A. Ortnas, "Mechanistic studies of brazing in clad aluminium alloys," *Materials Science Forum,* Vols. 217-222, pp. 1703-1708, 1996.

[17] J. Lacaze, S. Tierce, M. C. Lafont, Y. Thebault, N. Pebere, G. Mankowski, C. Blanc, H. Robidou, D. Vaumousse and D. Daloz, "Study of the microstructure resulting from brazed aluminium materials used in heat exchangers," *Materials Science and Engineering A,* Vols. 413-414, pp. 317-321, 2005.

[18] M. Dehmas, P. Weisbecker, G. Geandier, P. Archambault and E. Aeby-Gautier, "Experimental study of phase transformations in 3003 aluminium alloys during heating by in situ high energy X-ray synchotron radiation," *Journal of Alloys and Compounds,* vol. 400, no. 1-2, pp. 116-124, 2005.

[19] S. Meijers, "Corrosion of aluminium brazing sheet," Delft University of Technology, Delft, Netherlands, 2002.

[20] F. Norouzi Afshar, J. H. W. de Wit, H. Terryn and J. M. C. Mol, "The effect of brazing process on microstructure evolution and corrosion performance of a modified

AA4XXX/AA3XXX brazing sheet," *Corrosion Science,* vol. 58, no. 5, pp. 242-250, 2012.

[21] H. Jin, M. S. Kozdras, B. Shalchi-Amirkhiz and S. L. Winkler, "Liquid-solid interaction in Al-Si/Al-Mn-Cu-Mg brazing sheets and its effects on mechanical properties," *Metallurgical and Materials Transactions A,* 2018.

[22] American Welding Society Committee on Brazing and Soldering, Brazing Handbook, 5th ed., Miami: American Welding Society, 2007.

[23] H. R. Brooker and E. V. Beatson, Industrial Brazing, London: Newnes-Butterworths, 1975.

[24] F. J. Humphreys and M. Hatherly, Recrystallization and Related Annealing Phenomena, 2nd ed., Oxford: Elsevier, 2004.

[25] R. J. McElroy and Z. C. Szkopiak, "Dislocation-substructure-strengthening and mechanical-thermal treatment of metals," *International Metallurgical Reviews,* vol. 17, no. 1, pp. 175-202, 1972.

[26] Y. Bergstrom, "A dislocation theory for the plastic deformation of metals and its applicability - Paper 1: A dislocaiton model for the plastic deformaiton of single-phase alpha iron," May 2010. [Online]. Available: http://www.plastic-deformation.com/. [Accessed 21 June 2018].

[27] Y. Bergstrom, "A dislocation theory for the plastic deformation of metals and its applicability - Paper 3: A theory for the temperature and strain-rate dependences of dislocation re-mobilisation," May 2010. [Online]. Available: http://www.plastic-deformation.com/. [Accessed 21 June 2018].

[28] S. Kurukuri, M. J. Worswick and S. Winkler, "Constitutive modelling of aluminium alloy sheet at warm forming temperatures," *Journal of Physics: Conference Series,* vol. 734, pp. 1-4, 2016.

[29] ASM International, "Deformation processing," in *Elements of Metallurgy and Engineering Alloys*, F. C. Campbell, Ed., Materials Park, ASM International, 2008, pp. 279-302.

[30] P. A. Tebbe and G. T. Kridli, "Warm forming of aluminium alloys: an overview and future directions," *International Journal of Materials and Product Technology,* vol. 21, no. 1-3, pp. 24-40, 2004.

[31] F. Shehata, M. J. Painter and R. Pearce, "Warm forming of aluminium/magnesium alloy sheet," *Journal of Mechanical Working Technology,* vol. 2, no. 3, pp. 279-290, 1978.

[32] S. Toros, F. Ozturk and I. Kacar, "Review of warm forming of aluminum–magnesium alloys," *Journal of Materials Processing Technology,* vol. 207, no. 1-3, pp. 1-12, 2008.

[33] D. Li and A. K. Ghosh, "Biaxial warm forming behavior of aluminum sheet alloys," *Journal of Materials Processing Technology,* vol. 145, no. 3, pp. 281-293, 2004.

[34] N. Abedrabbo, F. Pourboghrat and J. Carsley, "Forming of aluminum alloys at elevated temperatures-part 1: material characterization," *International Journal of Plasticity,* vol. 22, no. 2, pp. 314-341, 2006.

[35] M. Kumar and N. G. Ross, "Influence of temper on the performance of a high-strength Al–Zn–Mg alloy sheet in the warm forming processing chain," *Journal of Materials Processing Technology,* vol. 231, pp. 189-198, 2016.

[36] R. Verma, "Effect of elevated temperature on mechanical behaviour and springback of aluminum alloy brazing sheets," University of Waterloo, Waterloo, ON, 2016.

[37] S. C. Churchill, Soldering and Brazing Technology Part Two Brazing, Brighton: The Machinery Publishing Co. LTD., 1963.

[38] T. Young, "An essay on the cohesion of fluids," *Philosophical Transactions of the Royal Society of London,* vol. 95, pp. 65-87, 1805.

[39] A. Dupre, Theorie mecanique de la chaleur, Paris: Gauthier-Villars, 1869.

[40] N. Eustathopoulos, F. Hodaj and O. Kozlova, "The wetting process in brazing," in *Advances in Brazing: Science, Technology and Applications*, D. P. Sekulic, Ed., Oxford, Woodhead Publishing, 2013, pp. 3-30.

[41] M. M. Schwartz, "Introduction to Brazing and Soldering," in *ASM Handbook Volume 6*, Materials Park, OH, ASM International, 1993.

[42] B. E. Cheadle and K. F. Dockus, "Inert atmosphere fluxless brazing of aluminum heat exchangers," SAE Technical Paper 880446, 1988.

[43] S. F. Corbin, S. Winkler, D. R. Turriff and M. Kozdras, "Analysis of fluxless, reactive brazing of Al alloys using differential scanning calorimetry," *Metallurgical and Materials Transactions A,* vol. 45, no. 9, pp. 3907-3915, 2014.

[44] Y. Sugiyama, "Brazing of aluminium alloys," *Welding International,* vol. 3, no. 8, pp. 700-710, 1989.

[45] H. Zhao and D. P. Sekulic, "Diffusion-controlled melting and re-solidification of metal micro layers on a reactive substrate," *Heat and Mass Transfer,* vol. 42, no. 6, pp. 464-469, 2006.

[46] F. Gao, D. P. Sekulic, Y. Qian and X. Ma, "Residual clad formation and aluminum brazed joint topology prediction," *Materials Letters,* vol. 57, no. 29, pp. 4592-4596, 2003.

[47] F. Gao, D. P. Sekulic, Y. Y. Qian and J. G. Morris, "Formation of microlayers of clad residue on aluminium brazing sheet during melting and resolidification in brazing process," *Materials Science and Technology,* vol. 20, no. 5, pp. 577-584, 2004.

[48] D. P. Sekulic, P. K. Galenko, M. D. Krivilyov, L. Walker and F. Gao, "Dendritic growth in Al-Si alloys during brazing. Part 1: experimental evidence and kinetics," *International Journal of Heat and Mass Transfer,* vol. 48, no. 12, pp. 2372-2384, 2005.

[49] J. L. Murray and A. J. McAlister, "The Al-Si (aluminum-silicon) system," *Bulletin of Alloy Phase Diagrams,* vol. 5, no. 1, pp. 74-84, 1984.

[50] J. R. Terrill, "Diffusion of silicon in aluminum brazing sheet," *Welding Journal Research Supplement,* vol. 45, no. 5, pp. 202-209, 1966.

[51] D. M. Turriff, S. F. Corbin and M. Kozdras, "Diffusional solidification phenomena in clad aluminum automotive braze sheet," *Acta Materialia,* vol. 58, no. 4, pp. 1332-1341, 2010.

[52] M. J. Benoit, M. A. Whitney, M. A. Wells and S. Winkler, "Reduction of liquid clad formation due to solid state diffusion in clad brazing sheet," *Metallurgical and Materials Transactions B,* vol. 47, no. 6, pp. 3501-3510, 2016.

[53] E. Nes, "Recovery revisited," *Acta Metallurgica et Materialia,* vol. 43, no. 6, pp. 2189-2207, 1995.

[54] S. P. Bellier and R. D. Doherty, "The structure of deformed aluminium and its recrystallization-investigations with transmission kossel diffraction," *Acta Metallurgica,* vol. 25, no. 5, pp. 521-538, 1977.

[55] P. Bate and B. Hutchinson, "A re-evaluation of the mechanism of SIBM," *Scripta Materialia,* vol. 36, no. 2, pp. 195-198, 1997.

[56] C. Liu, X. Xue, X. Chen, L. Li, C. Xia, Z. Zhong and D. Zhou, "Effect of microstructural evolution on sagging behavior of cold-rolled aluminum foil during the brazing thermal cycle," *Journal of Materials Engineering and Performance,* vol. 26, no. 11, pp. 5563-5570, 2017.

[57] A. Wittebrood, S. Desikan, R. Boom and L. Katgerman, "Liquid film migration in aluminium brazing sheet?," *Materials Science Forum,* Vols. 519-521, pp. 1151-1156, July 2006.

[58] J. E. Burke and D. Turnbull, "Recrystallization and grain growth," *Progress in Metal Physics,* vol. 3, pp. 220-244, 1952.

[59] E. S. Puchi-Cabrera, C. J. Villalobos-Gutierrez, A. Carrillo and F. Di Simone, "Non-isothermal annealing of a cold rolled commercial twin roll cast 3003 aluminum alloy," *Journal of Materials Engineering and Performance,* vol. 12, no. 3, pp. 261-271, 2003.

[60] J. S. Yoon, S. H. Lee and M. S. Kim, "Sagging resistance of cold rolled aluminum 4343/3N03/4343 clad sheet," *Journal of Materials Science Letters,* vol. 20, pp. 229-232, 2001.

[61] S. H. Lee, M. S. Kim, D. S. Jung, J. W. Han and B. D. You, "Fabrication and sagging behavior of three layer Al-Si/Al-Mn-Zn/Al-Si clad sheets for automotive heat exchanger," *Materials Science Forum,* vol. 439, pp. 221-226, 2003.

[62] Y. Tu, X. Liu, M. Zhang and J. Zhang, "Improving brazeability of AA3003+Zn brazing aluminum sheets by final annealing," *Advanced Materials Research,* Vols. 197-198, pp. 1555-1560, 2011.

[63] S. J. Noh, M. S. Kim, D. Jung, J. W. Han and B. D. You, "Effects of Si content and cold rolling condition on brazeability of Al-Mn-Zn alloy core brazing sheet," *Materials Science Forum,* Vols. 486-487, pp. 415-419, 2005.

[64] D. Y. Yoon, "Theories and observations of chemically induced interface migration," *International Materials Review,* vol. 40, no. 4, pp. 149-179, 1995.

[65] M. Nylen, U. Gustavsson, B. Hutchinson and A. Karlsson, "The mechanism of braze metal penetration by migration of liquid films in aluminium," *Materials Science Forum ,* Vols. 331-337, pp. 1737-1742, 2000.

[66] W. A. G. McPhee, G. B. Schaffer and J. Drennan, "The effect of iron on liquid film migration and sintering of an Al-Cu-Mg alloy," *Acta Materialia,* vol. 51, no. 13, pp. 3701-3712, 2003.

[67] D. N. Yoon and W. J. Huppmann, "Chemically driven growth of tungsten grains during sintering in liquid nickel," *Acta Metallurgica,* vol. 27, no. 6, pp. 973-977, 1979.

[68] S. W. Barker and G. R. Purdy, "On liquid film migration in aluminium-copper alloys," *Acta Materialia,* vol. 46, no. 2, pp. 511-524, 1998.

[69] H. S. Yang and R. Woods, "Mechanisms of liquid film migration (LFM) in aluminum brazing sheet," in *Vehicle Thermal Management Systems (VTMS) 3*, Indianapolis, 1997.

[70] A. J. Wittebrood, R. Beneictus and K. Vieregge, "Study of liquid film migration in O-temper AA3005 brazing sheet," in *6th International Conference on Aluminum Alloys (ICAA6)*, Toyohashi, 1998.

[71] A. Wittebrood, C. J. Kooij and K. Vieregge, "Grain Boundary Melting or Liquid Film Migration in Brazing Sheet," *Materials Science Forum,* Vols. 331-337, pp. 1743-1750, May 2000.

[72] J. S. Yoon, H. S. Lee and M. S. Kim, "Fabrication and brazeability of a three-layer 4343/3003/4343 aluminum clad sheet by rolling," *Journal of Materials Processing Technology,* vol. 111, no. 1-3, pp. 85-89, 2001.

[73] F. Norouzi Afshar, A. M. Glenn, J. H. W. de Wit, H. Terryn and J. M. C. Mol, "A combined electron probe micro analysis and scanning Kelvin probe force microscopy study of a modified AA4xxx/AA3xxx aluminium brazing sheet," *Electrochimica Acta,* vol. 104, pp. 48-63, 2013.

[74] D. A. Jones, Principles and Prevention of Corrosion, 2nd ed., Prentice Hall, 1995.

[75] ASTM International, "ASTM E1479-16, Standard Practice for Describing and Specifying Inductively Coupled Plasma Atomic Emission Spectrometers," ASTM International, West Conshohocken, PA, 2016.

[76] ASTM International, "ASTM E1097-12(2017), Standard Guide for Determination of Various Elements by Direct Current Plasma Atomic Emission Spectrometry," ASTM International, West Conshohocken, PA, 2017.

[77] M. E. Brown, Introduction to Thermal Analysis Techniques and Applications, 1st ed., New York: Chapman and Hall, 1988.

[78] M. L. Kuntz, S. F. Corbin and Y. Zhou, "Quantifying metallurgical interactions in solid/liquid diffusion couples using differential scanning calorimetry," *Acta Materialia,* vol. 53, no. 10, pp. 3071-3082, 2005.

[79] A. K. Ghosh, "The influence of strain hardening and strain-rate sensitivity on sheet metal forming," *Journal of Engineering Materials and Technology,* vol. 99, no. 3, pp. 264-274, 1977.

[80] W. F. Hosford and J. L. Duncan, "Sheet metal forming: a review," *JOM,* vol. 51, no. 11, pp. 39-44, 1999.

[81] S. Kahl, H. E. Ekstrom and J. Mendoza, "Tensile, fatigue, and creep properties of aluminum heat exchanger tube alloys for temperatures from 293 K to 573 K (20 °C to 300 °C)," *Metallurgical and Materials Transactions A,* vol. 45, no. 2, pp. 663-681, 2014.

[82] M. J. Benoit, M. A. Whitney, M. A. Wells and S. Winkler, "Effect of temperature and sheet temper on isothermal solidification kinetics in clad aluminum brazing sheet," *Metallurgical and Materials Transactions A,* vol. 47, no. 9, pp. 4425-4436, 2016.

[83] H. Kokawa, C. H. Lee and T. H. North, "Effect of grain boundaries on isothermal solidification during transient liquid phase brazing," *Metallurgical Transactions A,* vol. 22, no. 7, pp. 1627-1631, 1991.

[84] W. D. MacDonald and T. W. Eagar, "Isothermal solidification kinetics of diffusion brazing," *Metallurgical and Materials Transactions A,* vol. 29, no. 1, pp. 315-325, 1998.

[85] M. L. Kuntz, Y. Zhou and S. F. Corbin, "A study of transient liquid-phase bonding of Ag-Cu using differential scanning calorimetry," *Metallurgical and Materials Transactions A,* vol. 37, no. 8, pp. 2493-2504, 2006.

[86] M. L. Kuntz, B. Panton, S. Wasiur-Rahman, Y. Zhou and S. F. Corbin, "An experimental study of transient liquid phase bonding of the ternary Ag-Au-Cu system using differential scanning calorimetry," *Metallurgical and Materials Transactions A,* vol. 44, no. 8, pp. 3708-3720, 2013.

[87] M. Taheri, H. Weiland and A. Rollett, "A method of measuring stored energy macroscopically using statistically stored dislocations in commercial purity aluminum," *Metallurgical and Materials Transactions A,* vol. 37, no. 1, pp. 19-25, 2006.

[88] K. B. Han, "A component-level study on effect of warm forming on formability and springback of aluminum alloy brazing sheet," University of Waterloo, Waterloo, 2017.

[89] K. B. Han, R. George, M. J. Worswick and S. Winkler, "Effect of Warm Forming on Formability and Springback of Aluminum Alloy Brazing Sheet (accepted)," in *Numisheet 2018*, Tokyo, Japan, 2018 .

[90] Livermore Software Technology Corporation, "LS-DYNA keyword user's manual volume I," LSTC, Livermore, 2015.

[91] D. P. Sekulic, F. Gao, H. Zhao, B. Zellmer and Y. Y. Qian, "Prediction of the fillet mass and topology of aluminum brazed joints," *Welding Journal,* vol. 83, no. 3, pp. 102S-110S, 2004.

[92] M. C. Theyssier and J. H. Driver, "Recrystallization nucleation mechanism along boundaries in hot deformed Al bicrystals," *Materials Science and Engineering A,* vol. 272, no. 1, pp. 73-82, 1999.

[93] S. Kurukuri, A. H. van den Boogaard, A. Miroux and B. Holmedal, "Warm forming simulation of Al-Mg sheet," *Journal of Materials Processing Technology,* vol. 209, pp. 5636-5645, 2009.

[94] R. Sandstrom, B. Lehtinen, E. Hedman, I. Groza and S. Karlsson, "Subgrain growth in Al and Al-1% Mn during annealing," *Journal of Materials Science,* vol. 13, pp. 1229-1242, 1978.

[95] M. Nylen, U. Gustavsson and B. Hutchinson, "Mechanisms of erosion during brazing of aluminium alloys," *Materials Science Forum ,* Vols. 396-402, pp. 1585-1590, 2002.

[96] A. C. Scott, R. A. Woods and J. F. Harris, "Accelerated corrosion test methods for evaluating external corrosion resistance of vacuum brazed aluminum heat exchangers," Society of Automotive Engineers (SAE), Warrendale, PA, 1991.

[97] ASTM International, "ASTM G85-11, Standard practice for modified salt spray (fog) testing," ASTM International, West Conshohocken, PA, 2011.

[98] E. Szala, M. Wainer and K. Vieregge, "A closer look at the internal corrosion test for automotive heat exchangers: the OY water test," *Surface and Interface Analysis,* vol. 42, pp. 1458-1464, 2010.

[99] M. Melander and R. Woods, "Corrosion study of brazed aluminum radiators retrieved from cars after field service," *CORROSION,* vol. 66, no. 1, pp. 015005-1-015005-14, 2010.

[100] ASTM International, "ASTM D2570-16 Standard test method for simulated service corrosion testing of engine coolants," ASTM International, West Conshohocken, PA, 2016.

[101] F. N. Afshar, A. M. Glenn, J. H. W. de Wit, H. Terryn and J. M. C. Mol, "A combined electron probe micro analysis and scanning Kelvin probe force microscopy study of a modified AA4xxx/AA3xxx aluminium brazing sheet," *Electrochimica Acta,* vol. 104, pp. 48-63, 2013.